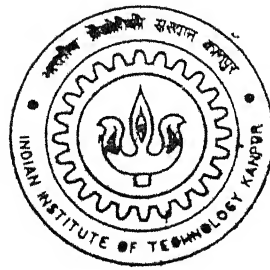


HEAT TRANSFER ENHANCEMENT IN RIBBED COOLANT CHANNELS OF GAS TURBINE BLADES

By

Kamlesh Singh



DEPARTMENT OF MECHANICAL ENGINEERING

Indian Institute of Technology Kanpur

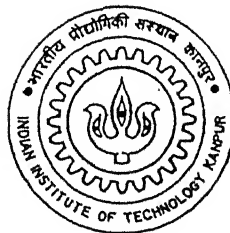
APRIL, 2002

HEAT TRANSFER ENHANCEMENT IN RIBBED COOLANT CHANNELS OF GAS TURBINE BLADES

A Thesis Submitted
In Partial Fulfilment of the Requirements
for the Degree of
Master of Technology

by

Kamlesh Singh

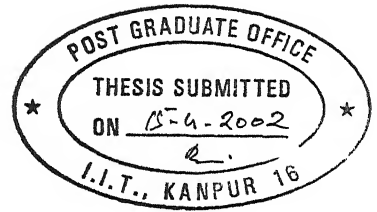


to the
DEPARTMENT OF MECHANICAL ENGINEERING
INDIAN INSTITUTE OF TECHNOLOGY KANPUR
INDIA
April, 2002

F 4 FEB 2003 / ME
पुरुषोत्तम काशीनाथ केनकर पुस्तकालय
भारतीय प्रौद्योगिकी संस्थान कानपुर
141872
अवधि क्र० A-----



A141872



CERTIFICATE

It is certified that the work contained in the thesis entitled "*Heat Transfer Enhancement in Ribbed Coolant Channels of Gas Turbine Blades*," by *Mr. Kamlesh Singh*, has been carried out under our supervision and that this work has not been submitted elsewhere for a degree.

Dr. P. K. Panigrahi
Asst. Professor
Dept. of Mechanical Engineering
I.I.T. Kanpur 208016

April, 2002

Abstract

The present work is an experimental study of heat transfer enhancement pertaining to the ribbed coolant channels of gas turbine blades. Gas turbine is a Major power source used in the generation of electricity and power plant of choice for modern aircrafts. In order to increase the performance of gas turbine cycles, it is desirable to raise the temperature of the gas entering the turbine. However, this raise is limited by the thermal and mechanical characteristics of the materials used in the gas turbine blades. Internal cooling of the blades are thus becoming more and more applied to achieve improvements. The findings from this work also have application in micro-heat exchangers and high density electronics packaging.

The effect of a single rib and two ribs mounted on the bottom surface of the rectangular channel are investigated in this work. The novelty of this work is the simultaneous and detailed measurements of instantaneous and average fluid flow and heat transfer characteristics. Hot wire anemometry (HWA) and resistance thermometry (RTD) have been utilized for the velocity and temperature measurements in the flow-field. Liquid crystal thermography (LCT) has been employed to map the surface temperature profiles and evaluation of the heat transfer coefficient. The effectiveness of one-rib and two-ribs is studied from flow modulation and heat transfer enhancement point of view. Results are reported for three Reynolds number (based on the hydraulic diameter of the channel), namely, 1.28×10^4 , 2.09×10^4 . and 2.94×10^4 . The rib pitch-to-height ratio set during the experiment is equal to 10.

The difference in effectiveness between the upstream and downstream recirculation region of the rib is clearly observed from the transient LCT images and surface Nusselt number distribution. The transient LCT results show the existence of a definite three dimensionality in the downstream region of the rib.

The transient LCT technique was used for the surface Nusselt number evaluation. The results from LCT was validated with the energy balance check. The conventional Nusselt number determination from the temperature profile was carried out and effect of the order of the polynomial curve fit on the results were explained. The turbulent boundary layer well past the ribs for both one-rib and two-rib cases is different from that of the smooth surface which was evident from the higher Nusselt number observed in the far-field region and the mismatch between the velocity and temperature profile with the law of the wall. The stagnation region around the second rib is not as significant as that around the first rib. The velocity and temperature profiles are compared with the flat plate laminar (Blasius) and turbulent (Law of the wall) profile. The skin friction coefficient, Nusselt number, velocity profile, temperature profile, and surface temperature and Nusselt number distribution are presented.

The results show that the local Nusselt number for the ribbed duct flow is higher in comparison to that of the smooth surface. The transition of the boundary layer to the equilibrium turbulent flat plate boundary layer in the presence of the rib is presented and discussed with the help of the shape factor and the comparison with the law of the wall. The transition of the thermal boundary layer was observed to take place earlier than the velocity boundary layer as the Prandtl number of the working fluid (air) is less than 1. The transition to the equilibrium flat plate boundary is observed to be delayed for the two-rib case in comparison to that of the one-rib case. The performance of the heat transfer enhancement was carried out using *entropy generation* principle. The performance evaluation shows that the augmentation is thermodynamically advantageous only at higher Reynolds numbers. There is a degree of correlation between the velocity fluctuation and temperature fluctuation, the former being significant in the core of the shear layer while later is significant close to the wall. Overall, the thermal boundary layer, the velocity boundary layer, flow visualization and the Nusselt number results are observed to correlate with each other very well. The use of ribs for heat transfer enhancement is clearly brought out from the measured data.

Acknowledgment

I feel immense pleasure and satisfaction by working with Prof. P. K. Panigrahi and Prof. K. Muralidhar for their brilliant guidance throughout the period of my M.Tech thesis helped to surpass all the obstacles smoothly. Their company not only enriched my knowledge but also widen my ways of thinking. I am indebted to them for many fruitful discussions and perspicacious guidance.

I am thankful to Mr. Andallib Tariq for his constant encouragement, invaluable suggestions and generous help on different occasions during my thesis work.

Special thanks to Mr. Rajesh, Mr. Sambunath for their co-operation in fabricating some experimental accessories.

I would like to thank all the members of our Lab, especially Mr. Sunil, Mr. Jyotirmay, Mr. Atul, Dutta, Vivek, Amit, Abir and Arnab for their constant company in the laboratory.

My family members were a constant source of encouragement for me throughout this work. I am sincerely thankful for the patience they kept in last more than one and half year.

I express my special thanks to my closest friend Mr. Ravipratap Singh for his encouragement during some difficult days of my stay at IIT kanpur. I am also thankful to my friends Rakesh, Dalton, Mittal, Pushpendra and Aman for making my stay plesent in IIT kanpur.

I am very thankful to the All Mighty for giving me enough perseverance, patience and strength to rise after every debacle.

Kamlesh Singh

Contents

Certificate	i
Abstract	i
Acknowledgements	iii
Contents	iv
List of Figures	xii
Nomenclature	xvii
1 Introduction	1
1.1 Literature Review	4
1.2 Objectives of the Present Work	8
1.3 Thesis Outline	9
2 Apparatus and Instrumentation	10
2.1 Wind Tunnel	10
2.2 Heating Section	11
2.3 Hot Wire Anemometry	13
2.4 Resistance Thermometry	14
2.5 Liquid Crystal Thermography (LCT)	14
2.5.1 Forms of Liquid Crystals	15

2.5.2	TLC Surface Coating	16
2.5.3	The Response Time	16
2.5.4	The Range of Application and Limitation	17
2.5.5	Image Processing	18
2.5.6	True Color Image Processing System	19
2.6	Uncertainty and Measurement Errors	19
3	Data Reduction	20
3.1	Velocity Data Reduction	20
3.1.1	Hotwire Calibration	21
3.1.2	Hotwire Data Reduction	23
3.1.3	Velocity Boundary Layer	25
3.2	Temperature Data Reduction	26
3.2.1	Thermal Boundary Layer	27
3.3	Energy Balance Check	29
3.4	Liquid Crystal Thermography	33
3.4.1	Calibration Test	33
3.4.2	Transient Test	35
4	Results and Discussion	40
4.1	Baseline Comparison of Smooth Channel Results	40
4.1.1	Velocity Field	41
4.1.2	Skin Friction Coefficient	41
4.1.3	Thermal Field	42
4.1.4	Nusselt Number	42
4.2	Nusselt Number from Temperature Profile	48
4.3	Effect of Heating Level	53
4.4	Comparison of No-rib, One-rib and Two-rib cases	57
4.4.1	Velocity Field	57

4.4.2	Boundary Layer Parameters	58
4.4.3	Thermal Field	60
4.4.4	Surface Temperature Visualization	75
4.4.5	Nusselt Number	79
4.4.6	Surface Nusselt Number Distribution	80
4.4.7	Transition of Boundary Layer	90
4.5	Performance Evaluation	97
5	Conclusions and Scope for Future Work	100
5.1	Conclusions	100
	Bibliography	103

List of Figures

1.1	Sketch of an internally cooled turbine blade alongwith rectangular channel with ribbed walls	3
2.1	Schematic drawing of flow system, coordinate system and instrumentation.	11
2.2	Sketch of configuration and dimensions of the test section.	12
3.1	Cross wire probe and velocity components	24
3.2	Control volume for energy balance check	31
3.3	HSI calibration chart of the liquid crystal used in the present work.	34
3.4	Variance of HSI in the calibration chart of the liquid crystal used in the present work.	35
3.5	Variation of Nu with x/e for different values of time	37
3.6	Verification of semi-infinite solid assumption with temperature measurement at different locations of the plate	38
4.1	Variation of u^+ with y^+ on the bottom surface of the smooth channel at Re=12800	43
4.2	Variation of u^+ with y^+ on the bottom surface of the smooth channel at Re=20900	43
4.3	Variation of u^+ with y^+ on the bottom surface of the smooth channel at Re=29400	44
4.4	Variation of the velocity boundary-layer thickness on the bottom surface of the smooth channel	44
4.5	Skin friction coefficient on the bottom surface of the smooth channel	45
4.6	Variation of the thermal boundary-layer thickness on the bottom surface of the smooth channel	45

4.7	Variation of t^+ with y^+ on the bottom surface of the smooth channel at $Re=12800$	46
4.8	Variation of t^+ with y^+ on the bottom surface of the smooth channel at $Re=20900$	46
4.9	Variation of t^+ with y^+ on the bottom surface of the smooth channel at $Re=29400$	47
4.10	Local Nusselt number variation on the bottom surface of the smooth channel	47
4.11	Variation of average Nu with Re for (TOP) no-rib case at $Q=69$ W, (MIDDLE) one-rib case at $Q=69$ W, (BOTTOM) one-rib case at $Q=89.7$ W	50
4.12	Variation of average Nu with Re for (TOP) one-rib case at $Q=132.8$ W, (MIDDLE) one-rib case at $Q=204$ W, (BOTTOM) two-rib case at $Q=69$ W	51
4.13	Variation of average Nu with Re for (TOP) two-rib case at $Q=89.7$ W, (MIDDLE) two-rib case at $Q=132.8$ W, (BOTTOM) two-rib case at $Q=204$ W	52
4.14	Comparison of thermal boundary layer thickness at all heating levels for one-rib case and $Re=12800$	55
4.15	Comparison of thermal boundary layer thickness at all heating levels for one-rib case and $Re=20900$	55
4.16	Comparison of thermal boundary layer thickness at all heating levels for one-rib case and $Re=29400$	56
4.17	Comparison of stream-wise velocity variation for all three cases at $Re=12800$	61
4.18	Comparison of stream-wise velocity variation for all three cases at $Re=20900$	61
4.19	Comparison of stream-wise velocity variation for all three cases at $Re=29400$	62
4.20	Comparison of cross-stream velocity variation for all three cases at $Re=12800$	62
4.21	Comparison of cross-stream velocity variation for all three cases at $Re=20900$	63
4.22	Comparison of cross-stream velocity variation for all three cases at $Re=29400$	63
4.23	Comparison of u_{rms} variation with y for all three cases at $Re=12800$	64
4.24	Comparison of u_{rms} variation with y for all three cases at $Re=20900$	64

4.25	Comparison of u_{rms} variation with y for all three cases at $Re=29400$	65
4.26	Comparison of v_{rms} variation with y for all three cases at $Re=12800$	65
4.27	Comparison of v_{rms} variation with y for all three cases at $Re=20900$	66
4.28	Comparison of v_{rms} variation with y for all three cases at $Re=29400$	66
4.29	Variation of velocity boundary layer thickness with x/e for all three cases at (TOP) $Re=12800$, (MIDDLE) $Re=20900$, (BOTTOM) $Re=29400$	67
4.30	Comparison of mean temperature variation for all three cases at $Re=12800$	71
4.31	Comparison of mean temperature variation for all three cases at $Re=20900$	71
4.32	Comparison of mean temperature variation for all three cases at $Re=29400$	72
4.33	Comparison of RMS temperature variation for all three cases at $Re=12800$	72
4.34	Comparison of RMS temperature variation for all three cases at $Re=20900$	73
4.35	Comparison of RMS temperature variation for all three cases at $Re=29400$	73
4.36	Variation of thermal boundary layer thickness with x/e for all three cases at (TOP) $Re=12800$, (MIDDLE) $Re=20900$, (BOTTOM) $Re=29400$	74
4.37	Transient liquid crystal images showing temperature changes during the cooling of the bottom surface with two ribs from $40^{\circ}C$ at $Re=20900$.	77
4.38	Transient liquid crystal images showing temperature changes during the cooling of the bottom surface with two ribs from $40^{\circ}C$ at $Re=12800$ (Left) and $Re=29400$ (Right).	78
4.39	Span-wise averaged local Nusselt number comparison of the no-rib case using LCT with that from the law of the wall at $Re=12800$	83
4.40	Span-wise averaged local Nusselt number comparison of the no-rib case using LCT with that from the law of the wall at $Re=20900$	83
4.41	Span-wise averaged local Nusselt number comparison of the no-rib case using LCT with that from the law of the wall at $Re=29400$	84
4.42	Comparison of span-wise averaged local Nusselt number variation for all three cases using LCT at $Re=12800$	84

4.43	Comparison of span-wise averaged local Nusselt number variation for all three cases using LCT at $Re=20900$	85
4.44	Comparison of span-wise averaged local Nusselt number variation for all three cases at $Re=29400$	85
4.45	Detailed Nusselt number distribution for no-rib, one-rib and two-rib cases at $Re = 12800$	86
4.46	Detailed Nusselt number distribution for no-rib, one-rib and two-rib cases at $Re = 20900$	87
4.47	Detailed Nusselt number distribution for no-rib, one-rib and two-rib cases at $Re = 29400$	88
4.48	Detailed Nusselt number distribution for $Re = 12800$ (TOP), $Re = 20900$ (MIDDLE) and $Re = 29400$	89
4.49	Variation of u^+ with y^+ for (TOP) no-rib case, (MIDDLE) one-rib case, (BOTTOM) two-rib case at $Re=12800$	91
4.50	Variation of t^+ with y^+ for (TOP) no-rib case, (MIDDLE) one-rib case, (BOTTOM) two-rib case at $Re=12800$	92
4.51	Variation of u^+ with y^+ for (TOP) no-rib case, (MIDDLE) one-rib case, (BOTTOM) two-rib case at $Re=20900$	93
4.52	Variation of t^+ with y^+ for (TOP) no-rib case, (MIDDLE) one-rib case, (BOTTOM) two-rib case at $Re=20900$	94
4.53	Variation of u^+ with y^+ for (TOP) no-rib case, (MIDDLE) one-rib case, (BOTTOM) two-rib case at $Re=29400$	95
4.54	Variation of t^+ with y^+ for (TOP) no-rib case, (MIDDLE) one-rib case, (BOTTOM) two-rib case at $Re=29400$	96

Nomenclature

A	Surface area, m^2
C_f	Skin friction coefficient
C_p	Specific heat, J/kg-K
D_h	Hydraulic diameter of channel, m
e	Height of rib, mm
h	Heat transfer coefficient, W/m ² -K
k	Thermal conductivity of air at average temperature, W/m-K
k_b	Thermal conductivity of bakelite, W/m-K
L	Length of heated section, m
$N_{\overline{Nu},a}$	Augmentation Nusselt number
$N_{\overline{Nu}\bar{f},a}$	Nusselt friction factor number
$N_{S,a}$	Augmentation entropy generation number
Nu_{avg}	Average Nusselt number
Nu_x	Local Nusselt number at location x, from one end
Nu	(hD_h/k) , Nusselt number based on hydraulic diameter of the duct
Δp	Average frictional pressure gradient per unit heated length
Pr	Prandtl number
q_w	Wall heat flux, W/m ²
q'_c	Heat transfer rate per unit heated length
Q	Heat input, W
Re	(UD_h/ν) , Reynolds number based on hydraulic diameter
Re_x	Local Reynolds number at location x
\dot{S}'	Entropy generation rate per unit heated length
t	Time

t_b	Thickness of bakelite sheet, mm
T_{bm}	Bulk mean temperature of fluid, °C
T_w	Average wall temperature, °C
T_{wi}	Wall temperature at initial time, °C
$T_w(x)$	Local wall temperature, °C
T_{rms}	RMS of temperature, °C
$T(x, y)$	Local air temperature, °C
T_∞	Free stream temperature, °C
u	Velocity of air within boundary-layer, m/s
u_{rms}	RMS of streamwise velocity component m/s
U_∞	Free stream velocity, m/s
v	Transverse velocity component, m/s
v_{rms}	RMS of transverse velocity component, m/s

Greek Symbols

μ	Dynamic viscosity, kg/sec- m^2
ν	Kinematic viscosity, m^2 /sec
ρ	Density, kg/ m^3
δ	Hydrodynamic boundary layer thickness, mm
δ_T	Thermal boundary layer thickness, mm
τ_w	Wall shear stress, N/ m^2
ϕ	Irreversibility distribution ratio
θ	Non-dimensional temperature
ϵ	Emissivity of aluminium plate
σ	Stefan-Boltzmann constant, 5.67×10^{-8}

Subscripts

a	augmented passage
ΔP	Irreversibility caused by fluid friction
ΔT	Irreversibility due to heat transfer
L	Average value
o	original (unaugmented) passage
w	Average wall condition
x	At axial location x
∞	Condition at boundary layer

Chapter 1

Introduction

Research and development in heat transfer is of significant importance to many branches of technology. Development includes new, efficient heat exchangers, thermal packaging of electronic equipments, novel heat transfer equipment as well as introduction of systems of heat exchanger in industrial processes, cooling in gas turbine blade passages and combustion chamber of IC engines are important areas of heat transfer research. There seems to be a growing need to develop cost effective enhancement technique and to understand mechanisms of enhancement of heat transfer, looking at the present day technology.

Modern, high-speed aero-engines operate at elevated temperatures about 2000 K, to achieve better cycle efficiencies. However, the presently available alloys can not resist temperatures much higher than 1350 K. Among the various high pressure turbine components, the vanes and blades are the most vulnerable since they are the first elements exposed to high enthalpy flow generated in the combustor. Various cooling (internal forced convection, impingement, film and transpiration) and surface coating methods have been developed over the last decades to maintain the metal temperature of these components within acceptable limits in this harsh environment.

Electronic equipment has become increasingly important to our daily life. Improvement of these systems requires continued miniaturization of electronic components. However, one of the most significant restrictions to achieve this goal is the inability to dissipate enough heat from these very closely-spaced devices. Accordingly, poor designed thermal management system will result in high

operating temperature for electronic equipment, leading to many potential problems or even premature failure. For example, in order to keep a Pentium CPU running smoothly, it is recommended by Intel that the maximum device junction (CPU die) temperature must not exceed 90 °C. Therefore, additional thermal enhancement scheme to dissipate the heat is necessary. Similarly, in advanced gas-cooled reactors, nuclear accidents are principally driven by the residual power (decay heat) generated by the fuel after the chain reaction is stopped caused by radioactive decay of fission products. If this decay heat is not removed, it will heat up the nuclear fuel until its fission product retention capability is degraded and its radioactivity is released.

The study of heat transfer performance is referred to as heat transfer enhancement, augmentation, or intensification. The basic idea of heat transfer augmentation is to disturb the velocity and temperature profiles close to the wall and also to create a secondary flow that will exchange heat and momentum between the wall region and the core region. Enhancement techniques can be classified either as passive methods or as active methods. The active method requires external power such as surface vibration, electric or acoustic fields. The passive method use surface modification on specific types of surface geometries and in some cases fluid additives are used to accomplish the enhancement. The rib turbulators are one of the principal means to enhance heat transfer. The presence of ribs, represented by prismatic obstacles emerging from a flat wall in a turbulent boundary layer, produces a typical flow pattern which is encountered in many engineering problems mentioned before, such as heat exchangers, advanced gas-cooled reactor fuel elements, internal blade cooling channels (Figure 1.1), and the ventilation equipment for micro-electronic systems. These ribs increase the heat transfer by increasing the heat transfer area (fin effect) and by disturbing the approach flow thereby the developing boundary layer. The developed boundary layer provides maximum resistance to heat transfer and hence breaking the boundary layer increases the heat transfer enhancement. This increase in heat transfer also contributes to simultaneous increase in the pressure drop. Thus it of interest to find out a roughness geometry that will yield high heat transfer augmentation with minimum pressure penalty.

Measurement of temperature distribution in many applications described earlier, such as electronics thermal management, gas turbine blade coolant pas-

sages and boiling heat transfer, requires complete characterization of the thermal performance. As a part of thermal characterization process, thermal designers must be able to identify any thermal 'hot-spots' that might lead to degraded thermal performance. The development of liquid crystal (LC) based thermography over the past 30 years has provided thermal engineers with a relatively inexpensive technique for visualizing and measuring surface temperature or even distribution of local heat transfer coefficient on the surface of the devices. Engineers and scientists have successfully used LC thermography to investigate various thermal phenomena in wide variety of applications.

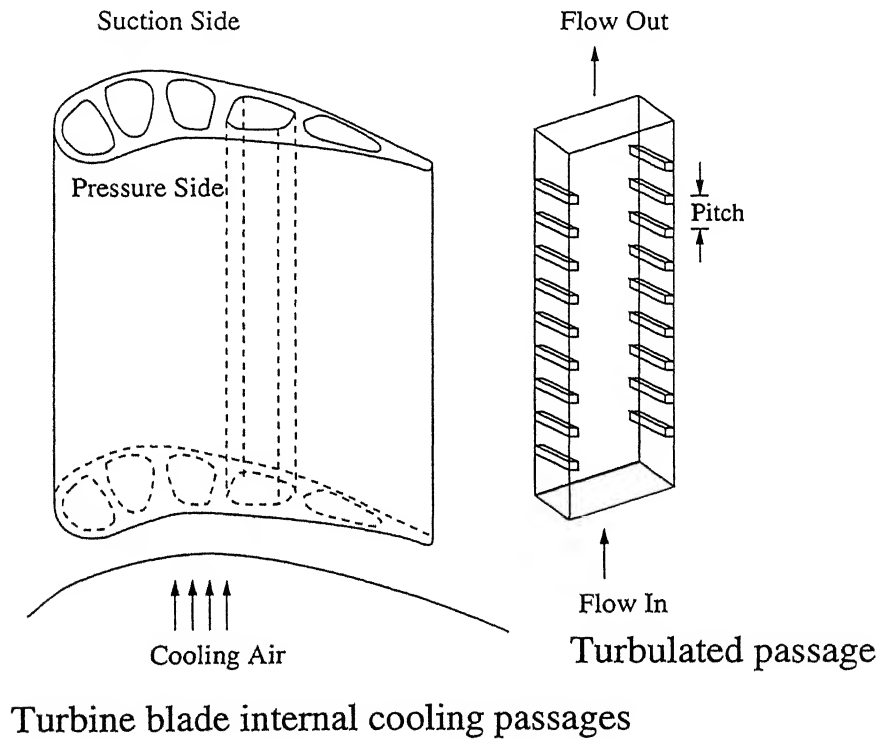


Figure 1.1: Sketch of an internally cooled turbine blade alongwith rectangular channel with ribbed walls

At heart of LCT are liquid crystal materials, called thermochromic liquid crystals (TLCs). Fundamentally, a liquid crystal is a phase that is between solid and pure liquid phase of matter. Thermochromic liquid crystal exhibit wavelength- dependent reflectivity that changes with temperature. They are particularly suitable for the measurement of surface temperature over a complete

area and have been used by many workers from different research groups to measure heat transfer coefficients. The crystals are supplied in a robust encapsulated form and are glued to the surface to form a layer between 10 and 20 μm thick. This temperature-sensitive coating is typically illuminated from a diffuse source and the reflected light monitored with a color CCD camera. Mapping temperature and heat transfer distribution using liquid crystals are possible through the hue-temperature calibration.

Figure 1.1 shows the internally cooled turbine blade. As shown in the figure, through passages are made in to the blades which can be approximately modeled as rectangular channels. These channels are turbulated to enhance the heat transfer. The present study is directed towards the study of these turbulators and there effectiveness so that the turbine could be operated at elevated temperatures.

1.1 Literature Review

To achieve the objective of increasing the heat transfer coefficient in internal flow with minimum amount of pressure losses, tremendous amount of work has been in progress. Roughening the wall of the passage is one of the various methods on which a large amount of literature is available . In context to the present work, where rib turbulators are used to study the heat transfer and flow characteristics in a duct flow, the literature survey can be divided into two sections. First, in which the work has been done to study the enhancement using the conventional measurement techniques and the main area of concern were a number of geometric parameters such as channel aspect ratio (AR), rib height-to-passage hydraulic diameter (e/D_h) or blockage ratio, rib angle of attack(α), the manner in which the ribs are positioned relative to one another (for example in-line, staggered, and criss cross) rib pitch-to-height ratio (s/e) and rib shape (round verses sharp corners, fillets, rib aspect ratio (AR_t), and skewness toward the flow direction) have pronounced effects on both local and overall heat transfer coefficients. Second, where study is totally based on the liquid crystal thermography. The earliest study to use liquid crystal for convective heat transfer measurements was performed in early seventies. After that several number of investigators have been involved to use this technique as a very effective tool for the study of heat transfer enhancement.

Burggraf (1970) reported the results of turbulent air-flow in a square duct with transverse *solid type ribs* on two opposite walls for Reynolds number ranging from 13,000 to 130,000. The wall temperature distributions were measured by thermocouples. With a hydrodynamically fully developed condition at the heated duct entrance, the average Nusselt number of the ribbed side wall and friction factor were approximately 2.38 and 8.6 times the corresponding values for fully developed smooth duct flows, respectively. The average Nusselt number of the ribbed side wall was 19 percent greater than for the duct with four smooth walls.

Han *et al.* (1984, 88) investigated systematically the effects of the rib pitch, rib height, rib spacing, and the rib angle of attack on the average heat transfer and the average pressure drop for the fully developed turbulent flow in a uniformly heated, straight, square channel with two opposite rib-roughened walls. They found that a *symmetrical rib* arrangement gave the same results as a *staggered rib* arrangement and that the rib shape influenced the friction factor but had only a modest effect on the heat transfer coefficient. Metzger *et al.* (1988) used a *thermal transient technique* to examine the contribution of the rib heat transfer to the overall heat transfer of a rib-roughened walls with variations in rib angle of attack and pitch. *Square ribs* representing a blockage ratio of 0.14 were mounted on only one wider side of a 0.154 aspect ratio rectangular channel. The main conclusions were that heat transfer on the rib surface significantly contributed to the overall rib-roughened wall heat transfer and this contribution mainly depends on the rib pitch to height spacing with very little effect from the rib angle.

Ireland and Jones (1985) were first to present a transient technique for heat transfer measurements using a liquid crystal coating where they tracked the movement of a single band of liquid crystals during a transient experiment.

Metzger *et al.* (1991) presented a transient liquid crystal technique where they used an image processing system to measure the time at which each location on the test surface reaches a certain liquid crystal band temperature during a transient test. The technique basically measures iso-heat transfer coefficient lines on the liquid crystal coated surface.

Liou and Hwang (1992) reported the heat transfer and friction in a ribbed rectangular duct. They used highly localized heat input to the fluid and combined with that the presence of ribs caused the situation where neither isothermal

nor isoflux condition was established. *Square* ribs with rib pitch to height ratio of 10, 15 and 20 were placed symmetrically on the bottom and upper surface of the duct of aspect ratio of 4:1. The Reynolds number range during the experiment was kept between 5000 to 50,000 with measurements being done in both developing and developed region of the flow. Holographic interferometry, thermocouples, pitot tube and pressure taps were used for the measurement of temperature field, wall temperature, centerline pressure distribution and static pressure drop respectively. They found that there were the regions of hot spots around the downstream corners of the ribs and 60 to 150 % enhancement were obtained with ribbed ducts when compared with smooth ducts at equal mass flow rate. enhancement was 8 to 50 % when compared on the basis of equal pumping power.

Acharya *et al.* (1993) performed numerical as well as experimental investigations to obtain periodic fully developed flow and heat transfer results for a ribbed duct, using the nonlinear and standard $K - \epsilon$ turbulence models.

Hirota *et al.* (1994) studied forced convective heat transfer for a turbulent flow through a square duct with a ribbed roughed bottom wall. Isothermal condition was maintained for all sides of wall by condensing the saturated steam. They have tried to examine the mechanism of heat transfer improvement in rough ducts, not only the wall heat transfer coefficient but the characteristics of the entire temperature field in the duct, with attention to the secondary flow effects as well. The main findings of their work are that periferally averaged local Nusselt number on smooth walls of the rough duct are 1.71 to 1.97 times larger than those of the smooth ducts, and the distribution of the local wall heat flux on the upper smooth wall opposite the rough wall is similar to that of wall shear stress, influenced the behavior of the secondary flow.

Taslim *et al.* (1996) used liquid crystal thermography to determine the local Nusselt numbers in a square duct with *angled*, *V-shaped* and *discrete ribs* on two opposite walls. Only one wall was heated with a constant heat flux, while the other walls were adiabatic. Their results indicated that the heat transfer was highest for V-shaped ribs pointing downstream, contrary to the results of Han *et al.* (1991).

Ekkad and Han (1997) presented detailed Nusselt number distributions in

the 180° turn region of a two pass smooth square channel and studied the effect of various rib turbulators on a two-pass square channel with one ribbed wall, using a transient heat transfer technique with a liquid crystal coating on the test surfaces. They studied channels with 90°*parallel*, 60°*parallel*, 60°*V*, and 60°*broken V-rib* configurations. From their results, it is possible to identify the flow separation, re-attachment and secondary flow phenomena in the rib turbulated channels from the detailed heat transfer distributions. Later, Ekkad et al. (1998) compared the previous results (Ekkad and Han, 1997) with detailed heat transfer distribution data in a two-pass square channels with rib turbulators and *bleed holes*. Regional- averaged heat transfer results indicate that a surface with bleed holes provides similar heat transfer enhancement as that for a surface without bleed holes although (20-25) percentage of the inlet mass flow exits through the bleed holes.

Taslim *et al.* (1999) studied the heat transfer and friction factor in passages roughened by ribs. *Square* ribs of full length were placed on one, two, three and all walls in staggered arrangement. The primary wall heated such that constant wall heat flux condition was maintained and LC sheets were placed on it. The Reynolds number range was between 4000 to 40,000. The flow was fully developed, both thermally and hydrodynamically. They performed the experiments for square and trapezoidal ducts. LCT was used for temperature measurement while contact micro-meter was used for measuring the pressure differential across the rib roughened wall. They found that roughening of the partition walls enhances the heat transfer coefficients on primary walls considerably. This heat transfer coefficient enhancement was accompanied by an increase in overall channel friction factor. however, the net effect was an increase in the channel thermal performance.

Tsia and Hwang (1999) performed the experimental study of heat transfer and fluid flow in a rectangular duct with alternate attached-detached rib arrays. A uniform wall heat flux condition was maintained on the bottom surface of the duct. square ribs of two pitch to height ratio of 10 and 30 and rib height to duct height of 0.2 was studied. Aspect ratio of the duct was 4:1. The range of Reynolds number was kept between 12000 and 70000, with measurement being done in both developing and developed region of the flow. Thermocouples, hot-wire and micro-differential pressure taps were used to measure temperature, velocity and pressure

drop in the flow field respectively. Important findings of their work are that The thermally and hydrodynamically developing length of a composite rib roughened wall is longer than those for two fully attached or fully detached duct, and Fully developed heat transfer coefficient is also higher for composite arrangement of the ribs, while fully attached or fully detached arrangements give the maximum and minimum pressure penalties respectively.

Mochizuki *et al.* (1999) have carried out detailed measurement of heat transfer and fluid flow in turbulent flow through smooth and rib-roughened two straight, rectangular channels with a 180° sharp bend. For monitoring detailed distribution of local heat transfer coefficients over the four wall surfaces of the entire channel, more than 450 thermocouples have been used. Ribs have been attached to two opposite walls with an angle of 90° or 60° to the flow. Flow visualization tests have been performed which reveal the generation of secondary flows.

1.2 Objectives of the Present Work

The present study is concerned with heat transfer enhancement study of a rectangular channel due to the presence of surface mounted square ribs. The heating section is made of an aluminum plate of dimension 680 mm×298 mm×3 mm in order to achieve a uniform wall temperature boundary condition. The study is carried out with four different heating levels and five different Reynolds number.

The present experimental investigation is directed towards achieving the following objectives:

1. To impliment the liquid crystal thermography technique as a visualization tool and tool for Nusselt number determination.
2. To compare the effect of one-rib and two-ribs on simultaneous fluid flow and heat transfer characteristics of a rectangular channel experimentally using liquid crystal thermography, hot wire anemometry and resistance thermometry with the help of both mean and fluctuating quantities.
3. To elucidate the transition of both thermal and velocity boundary layer to

the equilibrium flat plate boundary layer behind surface mounted ribs.

4. To impliment and analyze the entropy generation principle for heat transfer enhancement performance evaluation.
5. To compare and contrast the effect of parameters i.e. Reynolds number and heating levels etc.

1.3 Thesis Outline

This thesis has been arranged in the following format: Chapter 1 presents the introduction, the literature survey and objectives of the work. Chapter 2 explains the experimental setup and the instrumentations used for experiments. Chapter 3 discusses about the principle of data analysis including the empirical relations used for comparison subsequently in results and discussion. In chapter 4, results are presented and discussed in detail. Overall conclusions are summarized in chapter 5.

Chapter 2

Apparatus and Instrumentation

The present study involves the measurement of heat transfer and flow characteristics from heated bottom surface of a rectangular duct exposed to a flow field. Figure 2.1 shows the sketch of the experimental setup used in this work. The experimental facility comprises of a flow circuit(wind tunnel), the heating section, traverse mechanism and an image processing system. Hot wire anemometry (HWA) and resistance thermometry (RTD) have been utilized for the velocity and temperature measurement in the velocity and thermal boundary-layer respectively. Temperature of the plate have been measured using a K-type thermocouple connected to a National Instrument's data acquisition card (NI 4351). Also wall temperature distributions have been recorded with liquid crystal sheets, exposed to two 150W tungsten-halogen lamps which provides an excellent color rendering even in the long run, a reasonable high efficacy, high luminance and compact size as described by de Boer and Fischer [7].

2.1 Wind Tunnel

The wind tunnel is of the open loop type which operates with the fan in the suction mode. The ambient air flow is sucked from the temperature controlled room into the test section through a flow straightener and five screens in the settling chamber and a 3:1 contraction cone. This air flows through the bell shaped contraction cone, the heated section, the unheated length of the duct and is then exhausted by a centrifugal fan that is run by a 3 phase motor. The

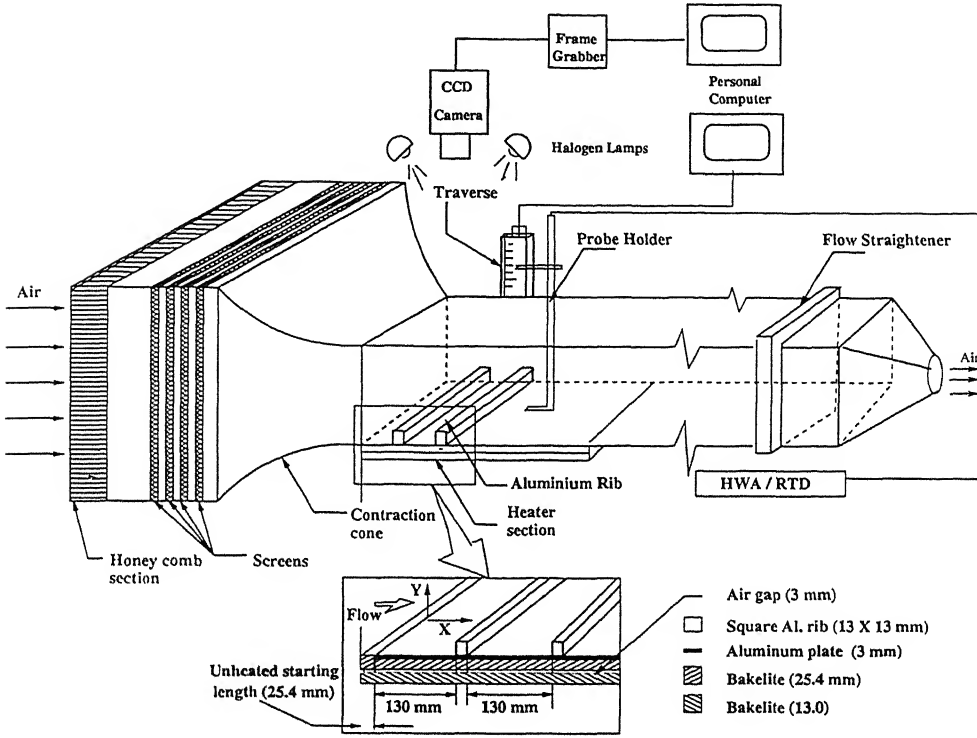


Figure 2.1: Schematic drawing of flow system, coordinate system and instrumentation.

speed of the blower is controlled by a speed controller (Victor G1000) supplied by Kirloskar Electric Co. Ltd., India. The settling chamber is 1950 mm long and has a rectangular cross section of 500 mm by 1000 mm. The test channel is 3300 mm long with an aspect ratio of 1.8:1, (160 mm \times 298 mm in the vertical plane). The test channel is made of perplex sheet of 12 mm thickness. Velocities in the range 1-4 m/s are presently realizable in the tunnel. The turbulence intensity was found to be less than 0.5%.

2.2 Heating Section

The heating section which is an assembly of an aluminum plate, Bakelite sheets, and a stainless steel foil as shown schematically in Figure 2.2.

The heating section is situated just at the entrance of test duct. The test plate is 730 mm long and is located flush with the bottom wall. It serves as the heat transfer surface, both as a smooth and one roughened by a rib, while the

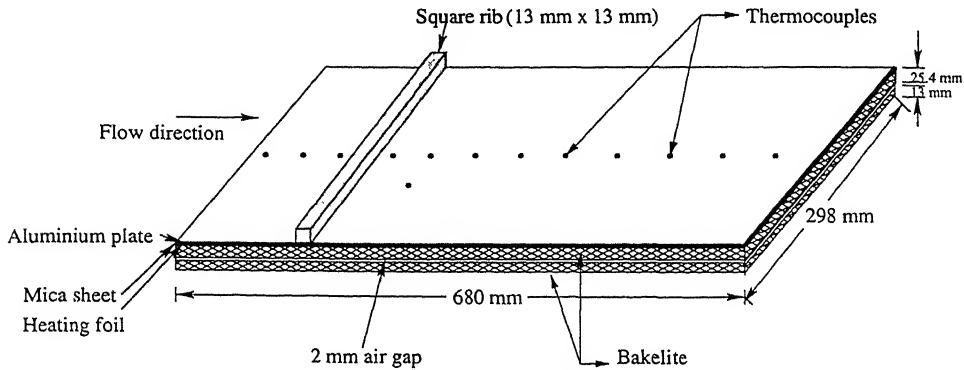


Figure 2.2: Sketch of configuration and dimensions of the test section.

top and two vertical walls are smooth and thermally insulated. Downstream of the test duct is an unheated section made of perplex with the same cross section. The heat transfer surface is constructed using a single aluminum plate (680 mm \times 298 mm \times 3 mm). There are six stainless steel foils of dimension 690 mm \times 47 mm \times 0.045 mm that are cemented on to the 25 mm thick Bakelite sheet. These foils are electrically connected in series and finally connected to a variac for power supply. To prevent the aluminum plate from electrical contact the upper surface of the stainless steel foil is coated with varnish. A 2 mm mica sheet is placed between the Bakelite and aluminum plate for better insulation. The surface of aluminum plate is highly polished to minimize emissivity, and hence the radiative losses. In addition, to minimize the conductive heat losses, lower surface of the Bakelite board is insulated using a 13 mm thick of Bakelite with a 2 mm thick air gap between them.

The heat transfer surface is also instrumented with thirteen calibrated thermocouples of the chromel-alumel type. The thermocouples are located inside the heated surface with omega-bond 101 epoxy. Twelve thermocouples are distributed along the center-line of the heated plate for wall temperature measurement. In order to check the span-wise temperature uniformity, surface temperature along the lateral of the heated plate is also instrumented with one thermocouple. To maintain a smooth flow surface, the thermocouple beads are attached to the underside of the Aluminum plate fed through the opening made in the two Bakelite sheets and mica. To measure the conduction losses, on the underside there are two thermocouple are mounted at the two sides of the upper Bakelite sheet exactly on the same line. There are two more thermocouples are mounted

at the two sides of the lower Bakelite sheet on the same line. This arrangement is repeated at a second location in the downstream.

2.3 Hot Wire Anemometry

The hot wire anemometer is an example of an intrusive technique whose application for measuring turbulent flow has far outstripped other instruments. The hot-wire is basically a thermal transducer and responds primarily to the velocity magnitude and is based on the principle of heat transfer. This sensor is small in size and coupled with a feedback circuit, it has a very high frequency response. The DANTEC model 56 C 17 CTA has been used in the present study. The main unit 56 C 17 CTA delivers the servo-voltage as the output of the instrument. This voltage is a measure of fluid velocity. The feed-back circuit of the CTA plays an important role in improving the frequency response of the hot-wire from about 100Hz to 10KHz.

The 56 C 01 CTA contains a function switch with three modes for operation, namely TEMP, STD.BY and FLOW. In TEMP position the resistance of the connected probe can be measured in terms of a current supplied to it. In STD.BY position no current flows through the bridge. In FLOW setting the CTA starts operating with the function of the servo amplifier. A setting named BRIDGE ADJ enables the adjustment of bridge balance for measurement of probe resistance and setting of the desired overheat resistance. This BRIDGE ADJ has a switch pair for coarser adjustment of overheat resistance and a screw for fine adjustment. Resistance settings ranging from 0-30 Ω in steps of 0.001 Ω are possible. This adjustment is crucial for adjusting the overheat resistance for the calibration procedure. CTA in TEMP mode produces a voltage proportional to resistance of wire. Calibration of this voltage with known temperature can be directly used to measure instantaneous temperature of the probe. The main unit 56 N 22 is a 5.5 digit display voltmeter. The primary purpose of this module is to measure the DC component of the output signal from 56 C 17 CTA. This module has 100 μ volt resolution, 1-1000 second integration time and switch selectable 14 inputs. DANTEC two wire probe (P63) has been used to measure the mean and rms velocity components of the flow in the present investigation with an integration time of 10-100 seconds.

The accuracy of hotwire measurements is affected by the accuracy of calibration procedure that of the procedure that is used to solve the nonlinear simultaneous equation. Calibration of a hot-wire probe involves two major steps, namely data generation and curve fitting. Calibration data is generated by measuring the output of the anemometer when the probe is subjected to flow with known velocity. In the present study, calibration has been performed in the test cell itself due to its high quality uniform inflow.

2.4 Resistance Thermometry

DANTEC Platinum coated tungsten wire ($\alpha_{20} = 0.36/^{\circ}\text{C}$) probe (P11) has been utilized as a temperature measuring device. The resistance of the wire of the probe at 20°C has been determined by a 5.5 digit display HP 3457A multimeter against the precalibrated thermister TBX-68T mounted on the terminal block of the National Instrument's data acquisition card (NI 4351). The HP 3457A has a reading and program storage and is available of making fast measurements. The HP 3457A's math operations manipulate or modify a measured reading before it is displayed, in addition the STAT operation evaluates mean, standard deviation, number of samples etc. The HP 3457A is programmed for converting the operating wire temperature. The temperature of the fluid flow is measured by using the relation:

$$R(T_{\text{sensor}}) = R_{20} + \alpha_{20}R_{20}(T_{\text{sensor}} - T_{20}) \quad (2.1)$$

The RTD probe is attached with the computer controlled traverse mechanism for accurate positioning.

2.5 Liquid Crystal Thermography (LCT)

The liquid crystal technology is one of the important inventions of the twentieth century that has found many applications as a visualization tool today. Liquid crystals change their color on applications of external stimulus, for example temperature and shear stress distributions and thus act as a measure of their change.

Liquid crystal is a unique substance, which exists between the solid and the isotropic-liquid phase of some organic compounds. It scatters incident light very selectively. The lowest temperature where liquid crystals scatters visible light is called the event temperature. At a temperature below the liquid crystal's event temperature, the liquid crystal will be in the solid state and will appear transparent. The clearing point temperature is the temperature at which the liquid crystal ceases to reflect visible light. When the temperature exceeds the clearing temperature point, the liquid crystal will enter the pure liquid state and appear transparent. The color output in liquid crystals is reversible and reproducible.

2.5.1 Forms of Liquid Crystals

Liquid crystals are commonly categorized based on their molecular morphology and optical properties e.g. smectic, nematic, and cholesteric. Cholesteric LCs, so named because the first of this type were derived from cholesterol, are capable of displaying a range of visible colors and are thus classified as thermochromic. However non-sterol based thermochromic LCs have also been developed, and are termed chiral-nematic, in reference to their molecular arrangement.

The nematic structure comes about when long range inter-molecular forces cause molecules to align relative to one another in planes. These planes are determined by the local solid boundaries and the direction of alignment of molecules within a plane is called director. Direction of this director changes on the application of mechanical or electrical deformation. The cholesteric materials form a similar structure. However, due to the shape of the molecules, the director of adjacent planes are rotated through certain angle and thus forming a helix of a certain pitch. The pitch of the helix changes depending upon the temperature of the liquid crystal. For the liquid crystal cholesteric materials considered for temperature sensing purpose, It is necessary that the pitch of the helix represented by the director is of the order of the wavelength of the visible light.

2.5.2 TLC Surface Coating

The most common means of applying thermochromic liquid crystals to a surface is by using micro-encapsulated form of the material. The tiny spherical capsules ($20\mu\text{m}$ in diameter) are glued to the test surface using an adhesive. Care is taken to ensure that the surface is fully dry before the mixture of crystal and binder mixture is applied. A thin ($20\mu\text{ mm}$ thick) coating is best developed by spraying many thick coats, with interim drying using an air heater. It is also worth noting that thin plastic sheets are available from suppliers and these often display a very clear color display. TLCs are available in different bandwidths, which defines the temperature range in which it actively reflects visible light. In the present work the commercially available thin plastic sheet of TLC (Hallcrest, Inc.;R35C5W) is pasted on the heating surface. This means the activation of the red color of this particular TLC begins at 35°C and the bandwidth is 5 degrees wide. The advantage of a precoated sheet are convenience and quality of color but these must be set against possible difficulties in wrapping the sheet over the complex, compound curvature surfaces which is not the case for the present work.

2.5.3 The Response Time

During the transient heat transfer experiment, the accuracy of the measured temperature depends on the rate at which the liquid crystal's optical properties respond to the change in the surface temperature. Ireland and Jones [20] measured the response of nematic type LC material and they were able to quantify the lag in the optical signals at rate of increase of surface temperature as high as $2000^{\circ}\text{C}/\text{sec}$. Experiments showed that delay between the time at which the surface reached a steady state color display temperature and the occurrence of the color display was no more than a few milliseconds (typically 3 to 10 milliseconds). In fact, the time taken for any point within the liquid crystal layer to achieve the heated surface temperature is a function of the distance from the surface, the layer thickness and the film diffusivity.

2.5.4 The Range of Application and Limitation

Although the TLCs offer an excellent way of measurement full surface temperatures in many applications, there are always some constraints on their use.

Temperature Range

Encapsulated liquid crystal materials are available in the temperature range -30 to 115 °C. The temperature range over which a material is optically active (the color play) can also be selected. The narrowest color range is 1.0 °C and the widest is about 20 °C. Wide-band crystals typically have bandwidths between 5°C and 20°C. They are useful when an object has large temperature variations. Practical applications of wide-band crystals include investigation of the surface temperature distribution on gas turbine blades or characterizing the temperature distribution on electronic components.

The Pressure Range

Encapsulated TLCs are insensitive to pressure. They are tested up to 133 bar without any appreciable change in its behavior.

The Speed of response

As discussed earlier, the optical response time of TLCs are in the range of few milliseconds e.g. for chiral-nematic it is around 3 msec.

Chemical Contamination

TLCs are complex organic compounds that are particularly susceptible to attack from organic solvents. In addition, UV (ultraviolet) light can destroy the color display, so care must be taken to minimize exposure to UV light.

The Maximum Heat Flux

As a rule-of-thumb, the value for maximum heat flux of 2×10^4 can be taken. The conductivity of the liquid crystal layer is typically 0.2 W/mK and hence the above heat flux gives a 2°C temperature drop across a 20 μm layer.

2.5.5 Image Processing

In a transient experiment, any site on the TLC surface will change color as the surface passes through optically active temperature range. This permits either color processing or intensity based (black and white) processing of the image of the surface optical response.

The standard color television practice of representing color by R, G and B tristimulus signals, red, green and blue, is used in color analysis. The tristimulus signals can be thought of as outputs from three camera detectors each with its optically sensitive range centered on a different wavelength in the visible spectrum. The intensity signals is made up of the sum of the R, G, and B signals. The R, G, and B signals are changed to H, S, and I (namely hue, saturation and intensity) form, which is less sensitive to the variations in strength of illumination. The derived signals hue and saturation are both independent of intensity and are produced using look-up tables in commercially available color framegrabbers. Hue depends on the ratio of RGB signals and its use has found favor in TLC work since its value normally increases monotonically with temperature. Hue physically represents the dominant wavelength of the light being displayed by the LCs. It is determined by establishing the angle between the orthogonal red, green, and blue components in RGB space.

Various techniques have been employed to calculate hue from the RGB components of the digitized images. The hue is calculated as(Ireland and Jones [21]):

$$\cos(H) = \frac{2R - G - B}{\{6[R - I]^2 + (G - I)^2 + (B - I)^2\}^{0.5}} \quad (2.2)$$

Where I is defined as:

$$I = \frac{R + G + B}{3} \quad (2.3)$$

The value of hue varies from 0 to 180° . The highest value of hue corresponds to perfect blue while lowest to red.

2.5.6 True Color Image Processing System

The image acquisition and processing system used in the present investigation consists of a high resolution 768 (horizontal) \times 574 (vertical) pixels CCD video camera (SONY XC-003P) with 16 mm focal length lens (VCL-16WM), a 24-bit color frame grabber board (Imaging Technology) and a high speed PC. These systems store the appropriate intensities of red, green, and blue needed to produce a corresponding matched color response at each point in an image. The frame grabber can be programmed for color analysis using base level C-programs. Several software programs are commercially available to analyse images. The software is capable of acquiring, freezing, sequential grabbing of images with specific functions such as determination of red, green, blue values and also the corresponding hue distribution. The current 24-bit true color image processing board from Imaging Technology, USA is programmed for aforementioned color analysis using base level C-programs.

2.6 Uncertainty and Measurement Errors

Possible sources of errors in the experimental data are: (a) fluctuating supply voltage of the D.C. power source, (b) the positional accuracy in locating the probe, (c) errors in calibration data, (d) inadequate compensation for room temperature, (e) inadequate signal length and sampling rate, (f) drift in electronics and (g) non-uniformity in illumination on the liquid crystals. Most of the experiments have been conducted several times and the repeatability of the results presented are confirmed. the local Nusselt number and average Nusselt number were found to be in good agreement with theoretical correlations and energy balance check.

Chapter 3

Data Reduction

The experiments performed during present work can be divided in to four parts. In the first part temperature and velocity data were collected for no-rib i.e. smooth duct case at one heating level and three different Reynolds number under the steady state, using RTD (resistance thermometric device) and hot-wire anemometer respectively. In the second part, similar data were collected for one-rib case at four different heating levels and five different Reynolds number. Third part is similar to the second but there were two ribs placed on the bottom surface of the duct instead of one. Fourth and last part of the experiments were performed to grab the sequential images of the liquid crystals under transient conditions for all three cases namely no-rib, one-rib and two-rib, at one heating level and three different Reynolds number, using colored CCD camera.

Now, the data reduction can be divided into three phases that are velocity data, temperature data and liquid crystal data. All three phases of data reduction are discussed in detail in the following sections.

3.1 Velocity Data Reduction

As mentioned earlier, velocity data were collected using hot-wire anemometer. The data obtained was not in terms of velocity but it was in terms of voltage which is required in excess to maintained the wire at its original temperature i.e. resistance. There is a unique relationship between this voltage and velocity which

must be obtained by proper calibration.

3.1.1 Hotwire Calibration

General calibration of hot-wire involves two major steps, namely Data-generation and Curve-fitting.

Data-Generation

Calibration data is generated by measuring the output of wires when it is subjected to a fluid with known velocity. Specially designed apparatus are used to generate high quality flow with uniform velocity, temperature and very low turbulence level

Hot-wire to be calibrated should be kept firmly in the calibration apparatus such that the direction of velocity of uniform flow should be normal to the wire. The velocity of the flow should be steady. The apparatus should be able to produce uniform flow with variable velocity. Output of the wires are noted at zero velocity and at various velocities of flow. Measurements can be repeated at a given velocity and average output of the wire can be taken as representative voltage. However, the data should be repeatable with very low scatter.

In the present study, calibration has been performed in the wind tunnel itself due to its high quality inflow. The maximum turbulence level is 0.5% .

Isothermal Calibration of Hotwire

DISA hot-wire equipment uses a linearizer card (56 N 21) which produces a voltage signal linearly proportional to flow velocity. The mathematical curve used by this card is given below.

$$y = 10^{A+Bx+Ey} + Cx + D \quad (3.1)$$

Here A, B, C, D and E are constants. Normally constants are selected to give a fluid velocity equal to 10m/sec for a wire output of 10 V. y is the linearizer

output equal to normalized velocity of fluid defined as,

$$y = 10 \times \frac{U}{U_{max}} \quad (3.2)$$

and x is normalized voltage defined as,

$$x = 10 \times \left[\frac{V - V_0}{V_{max} - V_0} \right] \quad (3.3)$$

and x is normalized voltage defined as,

$$x = 10 \times \left[\frac{V - V_0}{V_{max} - V_0} \right] \quad (3.4)$$

where V_0 is the output of wire measured at zero velocity of fluid and V_{max} measured at maximum velocity of fluid U_{max} .

The constants A, B, C, D and E are obtained by means of iterative least square error approach. For any calibration point (x_i, y_i) Equation 3.1 will produce an error ϕ_i given by

$$\phi_i = y_i - [10^{A+Bx_i+Ey_i} + Cx_i + D]. \quad (3.5)$$

The least square approach requires the sum of errors at all calibration points to be minimum *i.e.*,

$$\Phi = \sum_{i=1}^n \phi_i = \sum_{i=1}^n \{y_i - [10^{A+Bx_i+Ey_i} + Cx_i + D]\}^2 \quad (3.6)$$

$$\text{and} \quad \frac{\partial \Phi}{\partial A} = \frac{\partial \Phi}{\partial B} = \frac{\partial \Phi}{\partial C} = \frac{\partial \Phi}{\partial D} = \frac{\partial \Phi}{\partial E} = 0. \quad (3.7)$$

Let I be any of the parameters A, B, C, D or E , then

$$\frac{\partial \Phi}{\partial I} = 2 \sum_{i=1}^n \phi_i \frac{\partial \phi_i}{\partial I} = 0 \quad (3.8)$$

Hence A, B, C, D and E can be calculated using iterative least squares.

All the data have been normalized for a wire output of 0 – 10 volts and velocity normalized for 0 – 10 m/sec. Before normalization the data are fitted to a curve for linearization. Calibration of hot-wire in isothermal flow measurement is relatively easy. Measurement of non-isothermal flows requires a calibration curve which can include effect of fluid temperature.

3.1.2 Hotwire Data Reduction

A cross-wire sensor with two wires is used for two dimensional measurement. Each wire is separately calibrated and corresponding calibration curve and constants are evaluated. Substitution of output of a wire in its calibration gives effective cooling velocity sensed by the wire. The definition of effective cooling velocity is as follows. The components of velocity can be resolved into components normal to the wires and parallel to them. The effect of cooling by other two components of velocity can be accounted for by using sensitivity coefficients K_N and K_T . Experiments of Butler and Wanger (1982) and many others suggested a value of K_N ranging from 1.0-0.85 and K_T ranging form 0.1 to 0.25. A value of $K_N=0.9$ and $K_T=0.20$ are found to be optimum. The effective cooling velocity sensed by each wire is

$$V_e^2 = V_{NP}^2 + K_T^2 V_T^2 \quad \text{Two-dimensional flow} \quad (3.9)$$

where V_e is the effective cooling velocity, V_{NP} is the velocity component normal to the wire but parallel to the prongs, V_T is the velocity component tangential to the wire and $V_N N$ is the velocity component normal to both wire and prongs. Measurement of two and three dimensional flows involves calculation of components of velocity along laboratory coordinates. Many techniques are available in literature to get the components of velocity from known effective cooling velocities. Only two-dimensional flow measurement techniques are described in this chapter. With reference to Figure 3.1, for wire 1 the normal velocity component V_{NN} is $(u \cos \alpha - v \sin \alpha)$ and the tangential velocity component V_T is $(u \sin \alpha + v \cos \alpha)$. The heat transfer coefficient associated with each velocity component is different. Hence the effective velocities v_1 and v_2 sensed by wire 1 and wire 2 are written as,

$$v_1^2 = [(u \cos \alpha - v \sin \alpha)^2 + K_T^2 (u \sin \alpha + v \cos \alpha)^2] \quad (3.10)$$

$$v_2^2 = [(u \sin \alpha + v \cos \alpha)^2 + K_T^2 (u \cos \alpha - v \sin \alpha)^2] \quad (3.11)$$

Generally cross-wires manufactured with the angle between wires $2\alpha = 90^\circ$. With $\alpha = 45^\circ$ above equations can be simplified as,

$$v_1^2 = \frac{1}{2} [(u - v)^2 + K_T^2 (u + v)^2] \quad (3.12)$$

$$v_2^2 = \frac{1}{2} [(u + v)^2 + K_T^2 (u - v)^2] \quad (3.13)$$

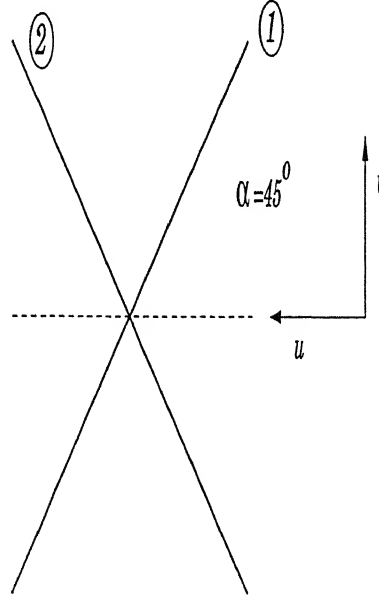


Figure 3.1: Cross wire probe and velocity components

The factor K_T takes into account the differences in the heat transfer coefficient between cross flow and parallel flow. Let $v_x = \frac{u+v}{\sqrt{2}}$ and $v_y = \frac{u-v}{\sqrt{2}}$. Substituting in Equations 3.12 and 3.13, we get

$$v_1^2 = v_y^2 + K_T^2 v_x^2 \quad (3.14)$$

$$v_2^2 = v_x^2 + K_T^2 v_y^2 \quad (3.15)$$

Hence, inversion of Equations 3.14 and 3.15 gives,

$$v_x^2 = a_1 v_1^2 + a_2 v_2^2 \quad (3.16)$$

$$v_y^2 = b_1 v_1^2 + b_2 v_2^2 \quad (3.17)$$

$$\text{where } a_1 = b_2 = \frac{1}{1-K_T^4} \text{ and } a_2 = b_1 = \frac{-K_T^2}{1-K_T^4}.$$

The instantaneous velocity components u and v can be calculated using v_x and v_y as,

$$u = \frac{v_x + v_y}{\sqrt{2}}$$

$$v = \frac{v_x - v_y}{\sqrt{2}}$$

The method mentioned above does not require instantaneous signal and equipment to collect instantaneous signal, but involves complex mathematical equations.

3.1.3 Velocity Boundary Layer

For the velocity distribution, u^+ has been plotted against non-dimensional distance in wall coordinate y^+ . The theoretical expression for velocity distribution in laminar flows can be obtained from the Blasius solution which is converted to wall coordinate. The theoretical expression for the velocity distribution in turbulent flows is obtained from the law of the wall which is expressed as

$$u^+ = 2.44 \ln y^+ + 5.0 \quad (3.18)$$

where

$$u^+ = \frac{u/U_\infty}{\sqrt{\frac{C_f}{2}}} \quad (3.19)$$

and

$$y^+ = \frac{y U_\infty \sqrt{\frac{C_f}{2}}}{\nu} \quad (3.20)$$

The basic unknown in the above equation is C_f and can be calculated by using the boundary condition: $y = \delta$, $u = U_\infty$. Hence

$$\frac{u}{U_\infty} = \sqrt{\frac{\tau_w}{\rho U_\infty^2}} (2.44 \ln \frac{y}{\delta} \sqrt{\frac{\tau_w \delta^2}{\rho \nu^2}} + 5.0) \quad (3.21)$$

With C_f (or τ_w) determined from Equation 3.21, it is possible to get the plot of u^+ against y^+ for turbulent flow.

The non dimensional boundary layer thickness (δ/x) has been plotted against the x/e in the present work. The theoretical expression for (δ/x) as a function of local Reynolds number for laminar flow is given as

$$\frac{\delta}{x} = 5.0 \text{Re}_x^{-\frac{1}{2}} \quad (3.22)$$

where Re_x can be written in terms of x/e as

$$\text{Re}_x = \frac{U e x}{\nu e} \quad (3.23)$$

For all further such correlations, the same Equation 3.23 has been used to replace Re_x to x/e . The theoretical expression for (δ/x) as a function of local Reynolds number for turbulent flow is given as

$$\frac{\delta}{x} = 0.37 \text{Re}_x^{-\frac{1}{5}} \quad (3.24)$$

The skin friction coefficient can be determined by measuring the velocity gradient in the near wall region of the channel. It can be expressed as

$$C_f = \frac{\mu(du/dy)|_{y=0}}{\frac{1}{2}\rho U_\infty^2} \quad (3.25)$$

where the wall velocity gradient is determined by fitting a best fit curve through the near-wall values of velocity. In Equation 3.18, μ and ρ are fluid properties determined at average temperature $(T_w + T_\infty)/2$. Further U_∞ is the free stream velocity.

The theoretical expression for the skin friction coefficient in laminar flow over flat plate is given by

$$C_f = 0.644\text{Re}_x^{\frac{1}{2}} \quad (3.26)$$

when $\text{Re}_x < 5 \times 10^5$, x being measured from the leading edge of the aluminum plate. The theoretical expression for the skin friction coefficient in turbulent flow over a flat plate is given by

$$C_f = 0.0592\text{Re}_x^{-\frac{1}{5}} \quad (3.27)$$

when $5 \times 10^5 < \text{Re}_x < 10^7$, assuming that the boundary-layer is fully turbulent from the leading edge.

The experimental u^+ against y^+ has been plotted by first obtaining C_f from the equation of law of the wall by supplying the values of U_∞ , δ and all the properties from the experiment, and then converting the u and y data from the hot-wire measurement to u^+ and y^+ coordinate.

3.2 Temperature Data Reduction

Temperature data were collected by RTD for which the resistance is determined by a precalibrated thermister. The HP 3457A multimeter which was used for the display of the resistance of probe wire, was programed for converting the operating resistance of the probe wire into the corresponding temperature. MATH and STAT operations are utilized for the aforementioned purpose of conversion.

3.2.1 Thermal Boundary Layer

The non-dimensional temperature θ is defined as

$$\theta = \frac{T_w(x) - T(x, y)}{T_w(x) - T_\infty} \quad (3.28)$$

Here $T_w(x)$ is the temperature of the plate at that point where the temperature profile is measured. The local fluid temperature is indicated by $T(x, y)$. T_∞ is the free stream temperature.

The theoretical non-dimensional temperature variation for laminar flow is obtained from Blasius solution by converting them in to wall coordinate. The theoretical non-dimensional temperature variation for turbulent flow is can be obtained from law of wall which is expressed as follows

$$t^+ = 2.075 \ln y^+ + 3.9 \quad (3.29)$$

where

$$t^+ = \frac{(T_w(x) - T(x, y)) \sqrt{\frac{\tau_w}{\rho}}}{q_w / \rho c_p} \quad (3.30)$$

Here τ_w , the wall shear stress is obtained as in section 3.1.3. In this equation only q_w is unknown. It can be obtained by applying the boundary condition, $y = \delta_T$, $T = T_\infty$. Thus

$$\frac{T_w(x) - T(x, y)}{T_w(x) - T_\infty} = \sqrt{\frac{q_w^2}{\tau_w \rho c_p^2 (T_w(x) - T_\infty)^2}} (2.075 \ln \frac{y}{\delta_T} \sqrt{\frac{\tau_w \delta_T^2}{\rho \nu^2}} + 3.9) \quad (3.31)$$

From above equation one can solve for q_w and subsequently plot u^+ as a function of y^+ .

In the present work, plot was also obtained between δ_T/x against x/e . The theoretical expression for δ_T/x for laminar flow is given as:

$$\frac{\delta_T}{x} = 5.496 \text{Re}_x^{-\frac{1}{2}} \quad (3.32)$$

The theoretical expression for δ_T/x in turbulent flow is given as:

$$\frac{\delta_T}{x} = 0.4067 \text{Re}_x^{-\frac{1}{5}} \quad (3.33)$$

The local convective heat transfer coefficient of the heated surface is presented in terms of the local Nusselt number based on the hydraulic diameter of the duct, Nu_{Dh} defined as

$$Nu_{Dh} = \frac{-Dh}{T_w(x) - T_{bm}(x)} \frac{dT}{dy} \Big|_{y=0} \quad (3.34)$$

Here the air temperature gradient $\frac{dT}{dy} \Big|_{y=0}$ is determined by fitting a best fit polynomial through all the data points for temperature. The local wall temperature $T_w(x)$ is read from the thermocouple output at that particular point. In Equation 3.34, $T_{bm}(x)$ is local bulk mean temperature defined as:

$$T_{bm}(x) = \frac{\int \rho T \cdot u \cdot dy}{\int \rho u \cdot dy} \quad (3.35)$$

The theoretical expression for the local Nusselt number for laminar flow is given by

$$Nu_x = 0.332 Re_x^{\frac{1}{2}} Pr^{\frac{1}{3}} \quad (3.36)$$

This is applicable for $Re_x < 5 \times 10^5$ and $0.6 < Pr < 50$. The theoretical expression for the local Nusselt number for turbulent flows is given by

$$Nu_x = 0.0296 Re_x^{0.8} Pr^{\frac{1}{3}} \quad (3.37)$$

when $5 \times 10^5 < Re_x < 10^7$

The properties of air were calculated at the film temperature

$$T_f = \frac{T_w(x) + T_\infty}{2}$$

Similar to the velocity data, temperature data is also plotted on wall coordinates i.e. t^+ is plotted against y^+ . The value of q_w required for this conversion is obtained from the equation for law of the wall given by equation 3.31. The value of C_f is supplied from the previous calculation from the law of the wall for velocity variation.

The average Nusselt number based on hydraulic diameter can be determined by applying the energy balance principle using the following equation

$$Nu_{Dh} = \frac{Q_{net} Dh}{K A (T_w - T_{bm})} \quad (3.38)$$

where Q_{net} represents the net heat transfer to coolant and is calculated by subtracting the total heat loss from the electrical power dissipated by the heater. The electrical power generated from the heater is determined from the measured current and voltage through the foil. The total heat loss includes the conductive heat loss from rear side of the heated plate and the vertical adiabatic plates to the environment, and the radiative heat from loss the plate to its surroundings. Here T_w is an average of the thirteen thermocouples reading and T_{bm} is the average bulk mean temperature.

3.3 Energy Balance Check

The integration of number of instrumentation in the experimental set-up and their faulty use may lead to significant error in the measurements. To verify our experimental procedure and assumptions for data analysis i.e. calculation of radiation and conduction losses, a detailed energy balance check is performed. The energy balance is carried out between the inflow, out-flow and surface heat transfer of the heated test section of the duct. The control volume can be taken as shown in Figure 3.2

Assuming uniform velocity profile at the inlet, energy entering and leaving from the various surfaces of the control volume can be written as:

$$\text{Energy in through face AD, } Q_{AD} = w \int_0^H (\rho C_p U T)_{\infty} dy$$

$$\text{Mass in through face AD} = w \int_0^H (\rho U)_{\infty} dy$$

$$\text{Mass out through face BC} = w \int_0^H \rho(T) u(y) dy$$

$$\text{Mass out through face CD} = w \left[\int_0^H (\rho U)_{\infty} dy - \int_0^H \rho(T) u(y) dy \right]$$

Energy out through face CD, $Q_{CD} = (\text{Mass out through face CD}) \times (C_p T)_\infty$

Energy out through face BC, $Q_{BC} = w \int_0^H \rho(T) C_{ptf} u(y) T(y) dy$

Electrical power input, $Q = V \times I$

Energy loss due to conduction, $Q_{\text{cond}} = \frac{k_b A_{\text{eff}} (T_1 - T_2)}{t}$

Energy loss due to radiation, $Q_{\text{rad}} = \sigma \epsilon A_t (T_w^4 - T_\infty^4)$

Net power input through face AB, $Q_{AB} = [Q - (Q_{\text{cond}} + Q_{\text{rad}})]$

Net power input in control volume, $Q_{\text{in}} = (Q_{AD} + Q_{\text{Electrical}})$

Net power out from control volume, $Q_{\text{out}} = (Q_{BC} + Q_{CD} + Q_{\text{cond}} + Q_{\text{rad}})$

Percentage excess energy balance = $\frac{Q_{\text{in}} - Q_{\text{out}}}{Q_{\text{in}}} \times 100$

In the energy balance check described above, the following points are taken into consideration:

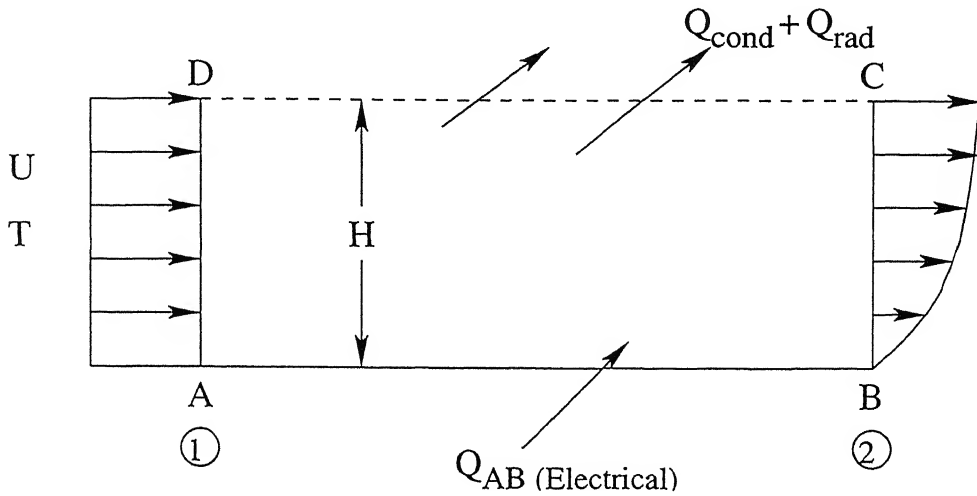


Figure 3.2: Control volume for energy balance check

1. Density of the fluid is a function of temperature.
2. Fin surface area is included in the calculation of radiation losses.
3. H is selected in such a way that U_{∞} is reached at both the ends.

The sources of error because of which the energy balance is not complete are

1. Neither u nor T is a constant in z -direction i.e. along the width of the duct.
2. Thermal losses to side walls are neglected.
3. Uncertainties are involved in ϵ (emissivity of polished surface) and k_b (thermal conductivity of Bakelite) values.

Sample Calculation

Measured data for one-rib case at $Re = 29400$ and 69.57 W power input are as follows

Temperature of plate, T_w	=	38.38°C
Ambient air temperature, T_∞	=	23.10°C
Voltage supplied to the foil, V	=	11.50 Volt
Current flows through the foil, I	=	6.05 amp
Length of the plate	=	0.68 m
Width of the plate	=	0.298 m
H for which U_∞ is reached	=	0.038 m
Hydraulic diameter	=	0.2082 m
Thickness of lower Bakelite(t_b)	=	0.013 m
Conductivity of Bakelite(k_b)	=	0.23 W/m.°C
Temperature of upper side of lower Bakelite(T_1)	=	33.11°C
Temperature of lower side of lower Bakelite(T_2)	=	31.50°C
Emissivity(ϵ) of aluminum plate(with LC sheet)	=	0.65
Stefan-Boltzmann constant(σ)	=	5.67×10^{-8}
Bottom side area(A)= 0.68 \times 0.298	=	0.20264 m ²
Side area	=	0.0751 m ²
Effective area(A_f)=A+0.5 \times Side area	=	0.2401 m ²
Conductivity(k) of air at film temperature(T_f)	=	26.51×10^{-3}
Power input	= $V \times I$	= 69.57 W
Radiation loss	= $\sigma \epsilon A (T_w^4 - T_\infty^4)$	= 12.43 W
Conduction loss	= $\frac{K_b A_f (T_1 - T_2)}{t}$	= 6.84 W
Net power input	= $Q - (Q_{Cond} + Q_{Rad})$	= 50.30 W
Average temperature difference	= $T_w - T_{bm}$	= 12.71°C
Average Nusselt number, Nu_{Dh}	= $\frac{Q_{Net} D_h}{k A (T_w - T_{bm})}$	= 150.83
Energy in through face AD, Q_{AD}	=	677.437 W
Mass in through face AD	=	0.0287 kg/sec.
Mass out through face BC	=	0.0256 kg/sec.
Mass out through face CD	=	0.0031 kg/sec.
Energy out through face CD, Q_{CD}	=	73.930 W
Energy out through face BC, Q_{BC}	=	609.469 W
Net electrical power input through face AB, Q_{AB}	=	45.118 W
Net power input to the control volume	=	722.556 W
Net power out from the control volume	=	700.220 W
Percentage excess energy balance	=	3.09 %

Note that AB is not the full length of the plate but it is the farthest downstream location where measurement is taken. The length of the plate for this location is 441 mm.

3.4 Liquid Crystal Thermography

Thermocromic liquid crystals were spread uniformly on the test surface before the rib and after the rib. The liquid crystal experiment performed in two phases.

1. Calibration test to relate color with temperature.
2. Transient test with three different Reynolds numbers to grab the sequential images showing the changes of color before and after the rib.

3.4.1 Calibration Test

Prior to the quantitative temperature measurement over the test surface, the method of color expression was defined and the relationship between the color and temperature of the liquid crystal assessed with a calibration test. Although the colors of the liquid crystals are observed by a RGB - data acquisition system, the R, G and B-data are not used to calibrate the sheet. Instead, the RGB color space is transformed to the hue-intensity-saturation color space, because the hue value is a monotonic function of the dominant wavelength reflected by the crystals and is therefore best suited for a unique color-to temperature relation. A perfectly lighted surface showed uniform background intensity of the color over the entire test surface. The background intensity determines the clarity of the picture seen by camera. If the background intensity is low, then the picture is too dark and the camera cannot capture the actual color change. If the background intensity is too high, then the actual color is lost in the white-light effect. Therefore optimum background intensity is maintained to provide uniform lighting of the surface and to obtain accurate color change information.

The test surface was heated to a temperature of nearly 43°C. The reading of one thermocouple was monitored continuously by PC connected through data card and it can give a direct temperature reading up to five digits after the decimal point. Then the power supply was cut off. The calibration test was done under the no flow condition. The plate started to cool under natural convection and images were captured at every 0.2°C temperature interval. Images were captured until color of the surface became red. Assuming that temperature is same within one

square inch, (45 x 45) pixels were selected in the image around the location where the thermocouple was placed. Then these images were processed in the PC to get HSI values from RGB values separately for those particular pixels. The HSI values were averaged to get a single hue, saturation and intensity value appropriate for the temperature. With appropriate curve fitting a plot was obtained between hue and temperature. Figure 3.3 shows the calibration curve which was used in transient experiment to determine temperature distribution from a set of images. It can be observed that intensity is almost constant for the entire colour display range.

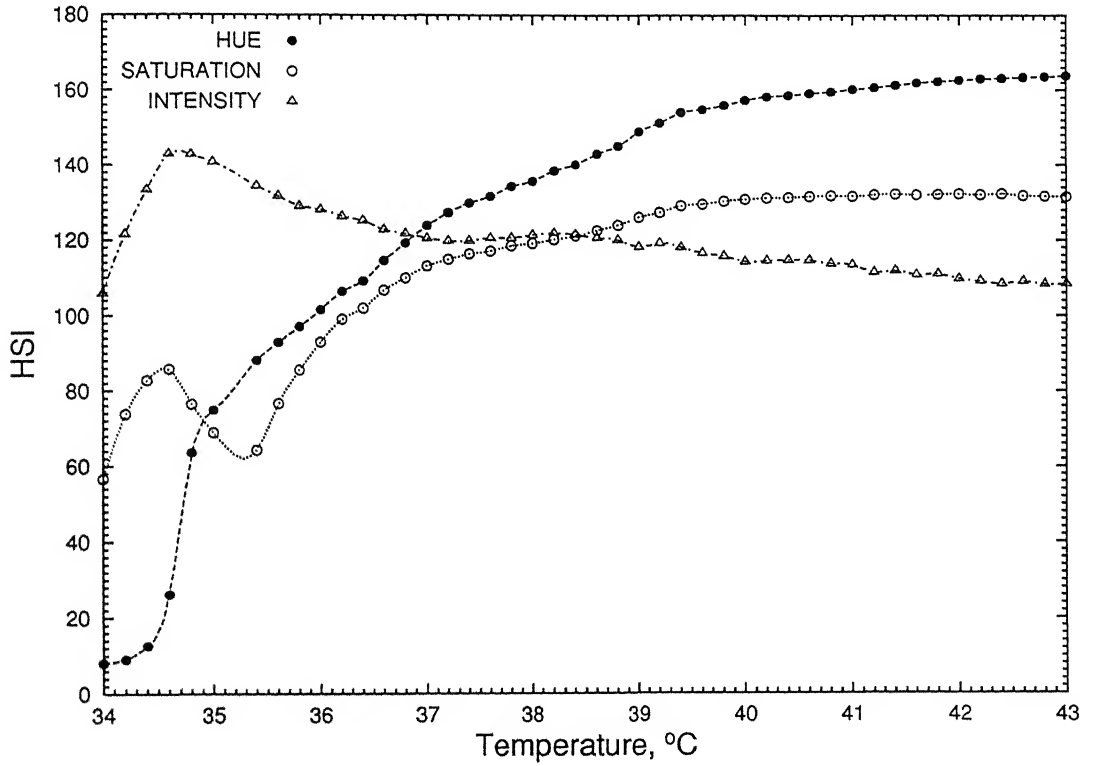


Figure 3.3: HSI calibration chart of the liquid crystal used in the present work.

Using hue from HSI color space reduces possible sources of uncertainty, such as the brightness of light source [9]. The hue is observed to have a monotonic change with temperature and also remains independent of the local illumination strength. The variance of hue with temperature is found to be small and constant, as shown in Figure 3.4, characterizing the uniform distribution of pixels and its high quality. Therefore, hue is used for relating the color of the liquid crystals and temperature.

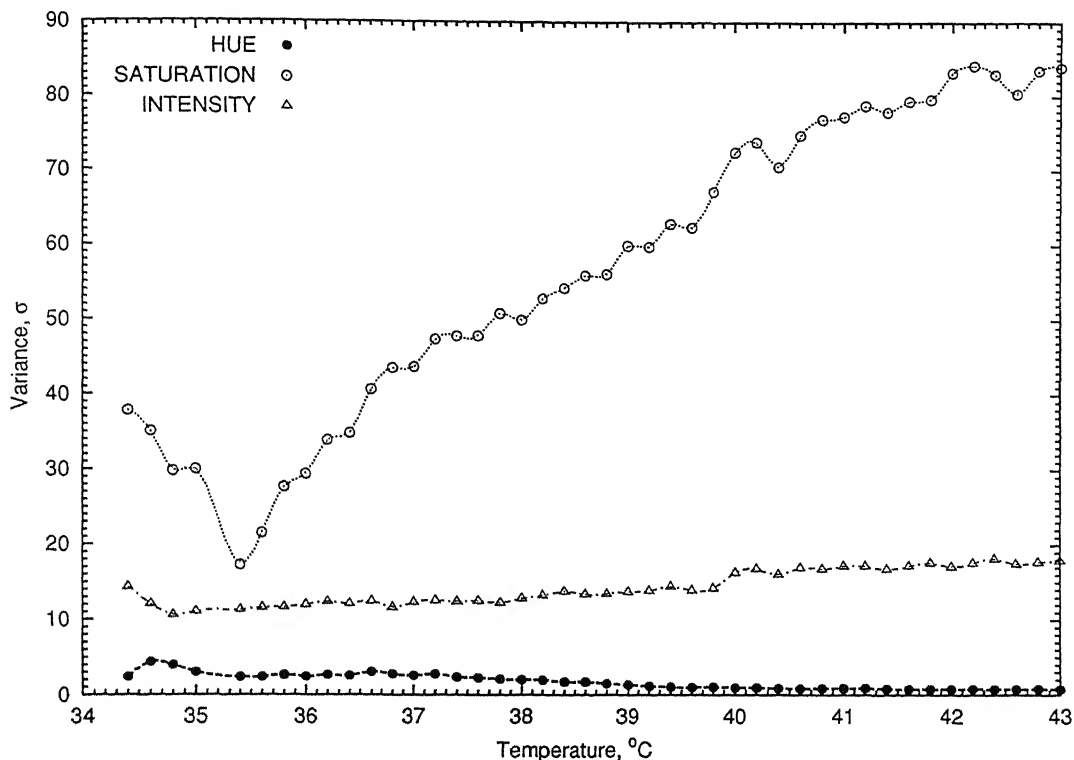


Figure 3.4: Variance of HSI in the calibration chart of the liquid crystal used in the present work.

There exists the effect of type of illumination, illumination source to model distance, illumination angle, camera conditions (such as circuit gain, filter adjustment, aperture and optical adjustments etc.), hence the image processing system color capturing adjustments have to be locked during the calibration and actual testing efforts [4]. The prefabricated LC sheets are calibrated in-situ under the no flow condition, keeping identical illumination and imaging characteristics throughout the experiment in order to keep the temperature measurement uncertainty within $\pm 0.10^{\circ}\text{C}$.

3.4.2 Transient Test

The transient heat transfer method has been applied by the authors to many different blade cooling problems. This method offers the significant advantage of yielding local heat transfer coefficients over complete test surfaces in a single experiment. The technique involves heating of the test plate up to a certain temperature. The flow is then started. The lighting arrangement and camera

position are kept identical to that of the calibration test. After the plate reaches a particular temperature, then the power supply is cut off. Due to forced convection the plate starts to cool. Images are then captured at 7 seconds intervals. This experiment was carried out for three Reynolds numbers namely 12800, 20900 and 29400 . Using the calibration curve, temperatures at different points were evaluated.

During the transient heat transfer experiments each pixel location will reach a prescribed temperature after different time interval depending upon the local heat transfer coefficient. This transient temperature distribution can be used for evaluation of the local heat transfer coefficient by assuming the test surface as a semi-infinite solid. For a semi-infinite solid, the one dimensional transient conduction equation is:

$$\frac{\partial T}{\partial t} = \alpha \frac{\partial^2 T}{\partial y^2} \quad (3.39)$$

Using a convective boundary condition at the surface,

$$-k \left(\frac{\partial T}{\partial y} \right)_{y=0} = h[T(y=0, t) - T_{\infty}] \quad (3.40)$$

Where T_{∞} is the free-stream temperature (or the local bulk mean temperature (T_{bm}) in the case of a duct) and $T(t)$ is the temperature of the surface at any time t . Assuming T_{∞} or T_{bm} to be constant, a semi-infinite wall with constant properties, and a uniform initial temperature of T_{wi} , the solution for the temperature at the surface i.e. $y = 0$ is

$$\frac{T_{wi} - T(t)}{T_{wi} - T_{\infty}} = 1 - \exp\left(\frac{h^2 \alpha t}{k^2}\right) \operatorname{erfc}\left(\frac{h\sqrt{\alpha t}}{k}\right) \quad (3.41)$$

or

$$\frac{T(t) - T_{\infty}}{T_{wi} - T_{\infty}} = \exp\gamma^2 \operatorname{erfc}(\gamma) \quad (3.42)$$

Where the parameter γ is defined as,

$$\gamma = \frac{h\sqrt{t}}{\sqrt{\rho c k}} \quad (3.43)$$

The only unknown in the equation 3.43 is h , which is determined by least square fit through the experimental data which follows the theoretical profile given by equation 3.42 in a prescribed total time span Δt . It was observed that the changes in temperature with time at any particular pixel starts diverging from the theoretical profile based on the semi-infinite solid assumption. So, the total time span (Δt) for which the curve fitting is done, plays an important role. If Δt is very high, then at some pixels, where heat transfer rate is very high, would reach to a temperature which is beyond the color display range of the liquid crystal. At the same time, some other pixels where heat transfer is low, would reach to a condition where experimental temperature gradient starts diverging from theoretical curve. At these pixels the predicted heat transfer coefficient would be comparatively higher than the actual. Hence, the pixels with higher heat transfer rate give the estimate of the total time span (Δt), for which the curve fitting should be done at each pixel. The process will be made clear by looking at the Figure 3.5.

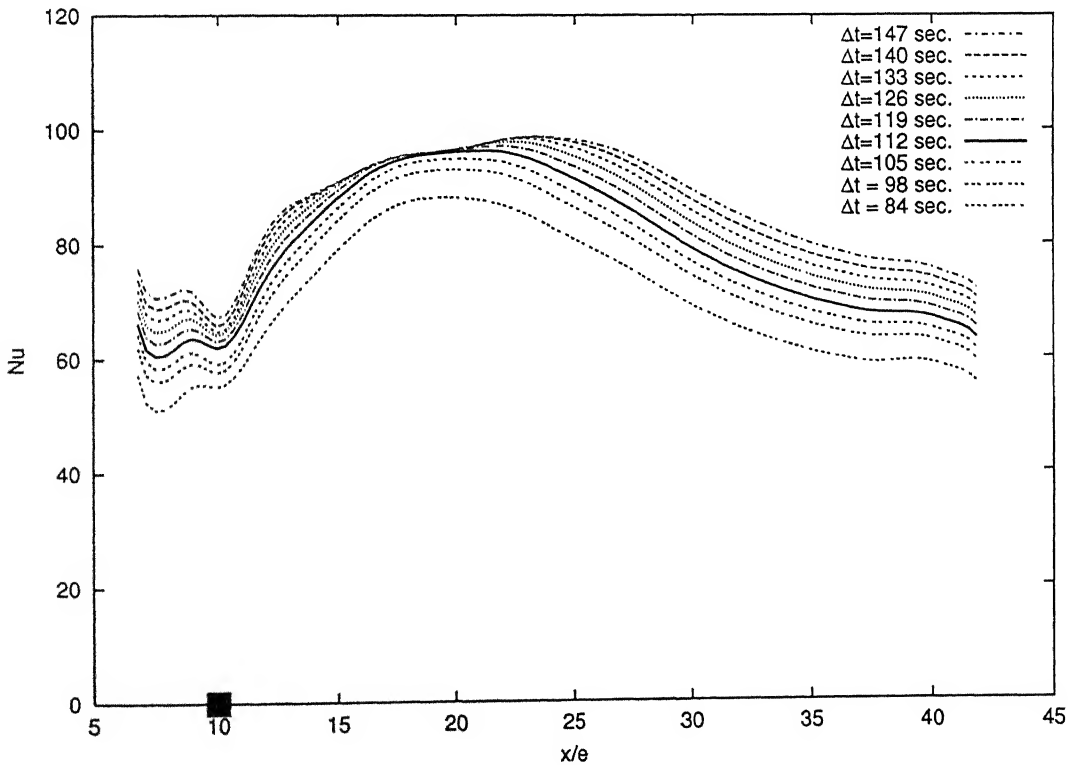


Figure 3.5: Variation of Nu with x/e for different values of time

The figure shows the variation of spanwise averaged Nusselt number for different time spans at a particular case of one-rib case and $Re = 20900$. The thick solid curve corresponds to the total time span for which the coolest zone on the surface has reached to the minimum temperature. Any time span greater than that will not give the actual variation of Nusselt number with x/e and any time span lower than this would give actual shape of variation but the absolute values will be lower. Similar process is repeated for all the cases under study to determine the total time span limit.

Validity of Semi-infinite Solid Assumption

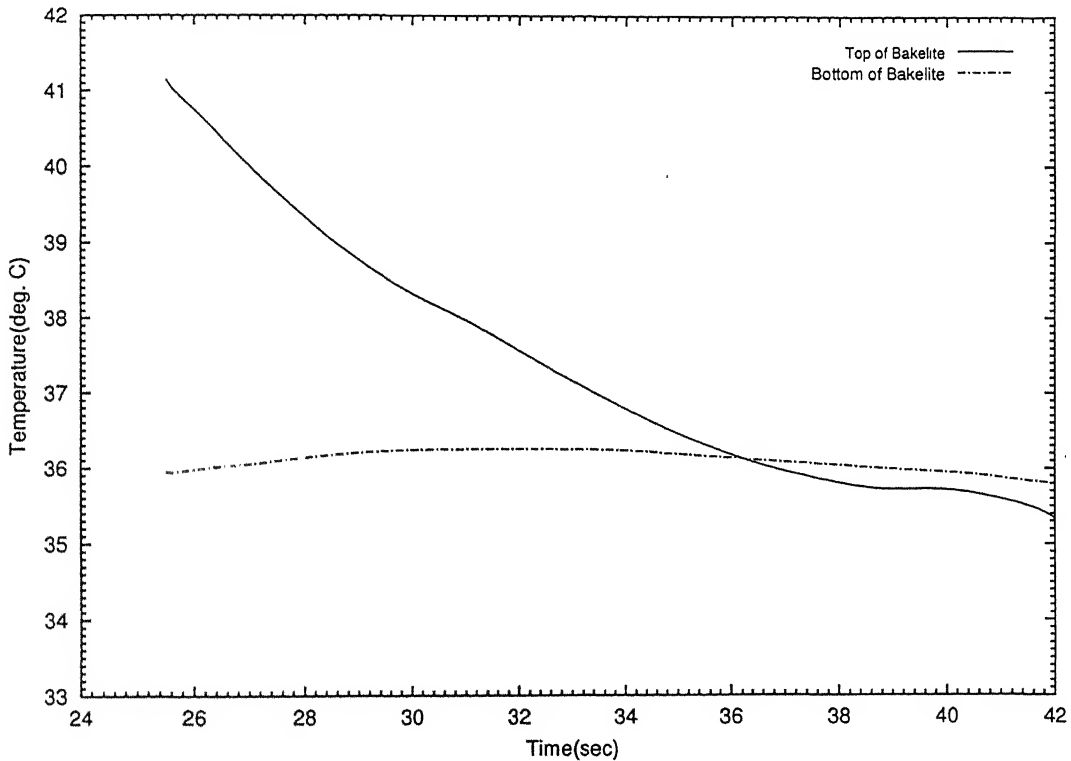


Figure 3.6: Verification of semi-infinite solid assumption with temperature measurement at different locations of the plate

The validity of the semi-infinite solid assumption is verified from the transient temperature measurement of the thermocouples located at the top and bottom of the Bakelite plate and its thickness. The assumption of a semi-infinite solid is valid only if the specimen is made from a material with low thermal diffusivity and chosen to be sufficiently thick. Chan *et al.* [5] suggested a criterion

for the minimum thickness of the material (y), as:

$$y > 4\sqrt{\alpha\Delta t} \quad (3.44)$$

In the present work, Bakelite is assumed to be the semi-infinite solid for which the thermal diffusivity is very low. The required thickness for the plate for even 150 seconds would be 16.54 mm. Since the thickness of the Upper Bakelite plate is more than 25 mm, above condition is fully satisfied. Temperature variation of the thermocouples placed at the top and bottom surface of the Bakelite plate are shown in Figure 3.6. It can be observed that the temperature of the lower surface of the Bakelite is remaining unchanged while the temperature of the top surface is decreasing when cooled. This observation confirms the validity of semi-infinite solid assumption.

The other assumption in the present study is that conductivity of the aluminum plate is very high and thickness is very small, so that the temperature gradients in the aluminum plate is equal to the temperature gradient of the upper surface of the Bakelite.

Chapter 4

Results and Discussion

In this chapter, the mean velocity profiles, boundary layer parameters, mean temperature profiles, velocity fluctuations, temperature fluctuations, skin friction coefficient, surface temperature visualization, averaged Nusselt number, surface Nusselt number distribution and transition of boundary layer results due to the presence of surface mounted disturbances are discussed. The effect of curve fitting on the Nusselt number determination from temperature profile data is discussed in detail by performing the energy balance check. The effect of heating level on the overall results are also presented and discussed. Smooth channel results without the presence of surface mounted rib is compared with existing correlations and is used as a baseline for comparing the effect of disturbance on the surface. Finally the performance evaluation of the disrupted surface is presented with the help of entropy generation principle.

4.1 Baseline Comparison of Smooth Channel Results

The smooth channel heated at the bottom surface is used for the baseline comparison. The power supplied to the aluminum plate is in the range of 68.40-70.15 W, where the limits indicate the extreme heat input level that could have been reached owing to line voltage fluctuations. The tests have been carried out at Reynolds number equal to 12800, 20900 and 29400. The velocity field, thermal field, Nusselt number and friction coefficient result are compared with existing

correlation discussed earlier in the data reduction section.

4.1.1 Velocity Field

The nature (laminar or turbulent) of the velocity boundary layer in the developing region of the rectangular channel is investigated by comparing the experimental profile with the Blasius solution (plotted on u^+ and y^+ coordinates) and law of the wall. In Figures 4.1, 4.2 and 4.3, the experimental velocity profile in u^+ and y^+ coordinate is plotted at different x/e locations with Blasius and law of the wall profile at different Reynolds number. It is observed that experimental profile at all x/e locations follow the law of the wall. The nature of the experimental profile is independent of the Reynolds number except for the fact that with increase in Reynolds number, law of the wall profile is followed up to a larger values of y^+ . Thus, the velocity profile at all x/e locations in a rectangular channel can be concluded to be turbulent in nature for the considered Reynolds number.

Figure 4.4 shows the variation of non-dimensionalized velocity boundary layer thickness at various stream-wise locations. It may be observed that the general trend of the boundary layer development is similar to that of the correlation. The difference in the magnitude between the present experiment and the correlation may be attributed to presence of a definite boundary layer at the inlet i.e. the absence of precise definition of the origin i.e. $x=0$ location.

4.1.2 Skin Friction Coefficient

Skin friction coefficient has been plotted against x/e in Figure 4.5. C_f is obtained by two methods, (a) curve fitting through the velocity profile and, (b) from the law of the wall. The experimental C_f values are also compared with empirical correlation results. It is very clear that C_f obtained by later method is following the turbulent profile which is again strengthening the turbulent nature of the flow. The results from curve fitting shows the skin friction coefficient to be on the higher side, especially for the lowest Reynolds number case.

4.1.3 Thermal Field

In Figure 4.6, the development of thermal boundary layer thickness on the bottom surface of the smooth channel at different Reynolds number is compared with the results from the correlation. The nature of variation is observed to be comensurate with each other. The difference in the magnitude may be attributed to the absence of precise definition of $x=0$ location. Overall, the thermal boundary layer thickness variation is observed to be close to the turbulent boundary variation pointing to the turbulent nature of the thermal boundary layer. Comparing Figure 4.6 with Figure 4.4, the effect of Reynolds number on the velocity boundary layer (δ) and thermal boundary layer (δ_T) is observed to be correlated. This may be due to the possibility of superimposed counter-rotating transverse vortices leading to different growth of the thermal boundary layer at different Reynolds number. In Figures 4.7, 4.8 and 4.9 the t^+ are plotted against y^+ . Similar to the velocity boundary layer, the thermal boundary layer is observed to be turbulent in nature as the experimental temperature profiles at all stream-wise locations follow closely the turbulent profile of the law of the wall.

4.1.4 Nusselt Number

Local Nusselt number based on hydraulic diameter is plotted against x/e in Figure 4.10. Nusselt numbers calculated from fitting a polynomial through RTD data are compared with correlations for Nusselt number in case of a flow over the bottom surface of the smooth channel. It is clear that for all the locations, Nusselt number is closely following the turbulent profile for higher Reynolds numbers. For the lowest Reynolds number, it is not following any of the profiles, but for most of the locations it is very nearly following the turbulent profile. This result is in accordance with the earlier conclusion of the flow being turbulent.

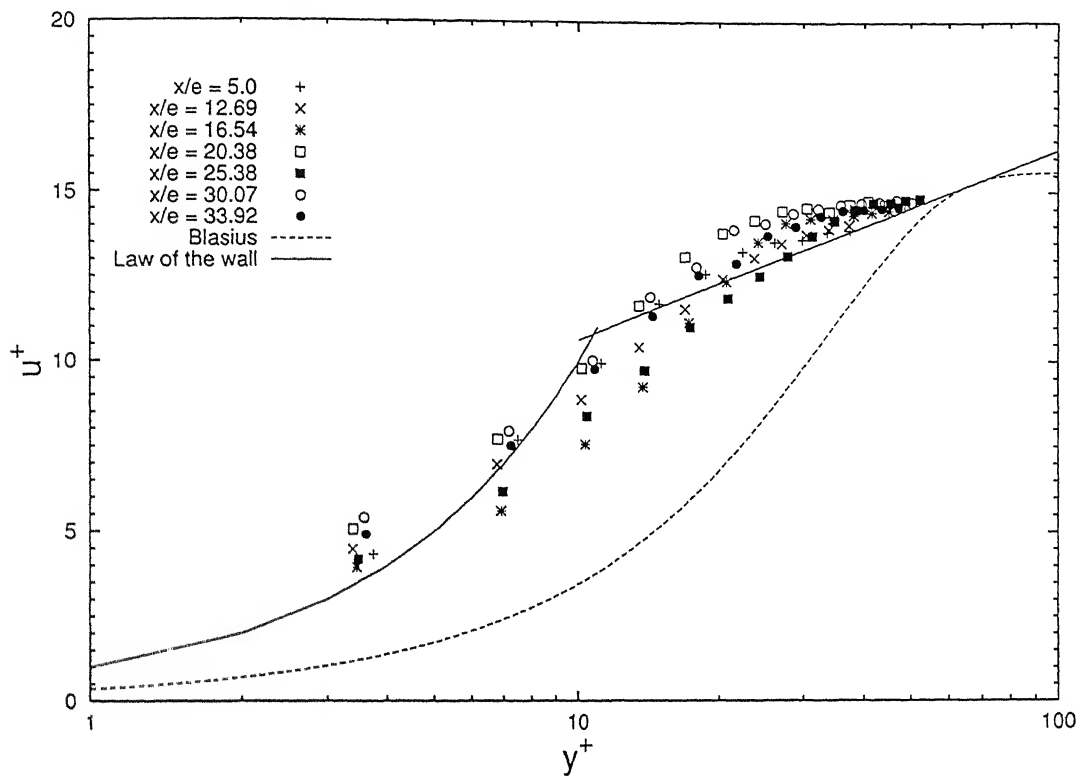


Figure 4.1: Variation of u^+ with y^+ on the bottom surface of the smooth channel at $Re=12800$

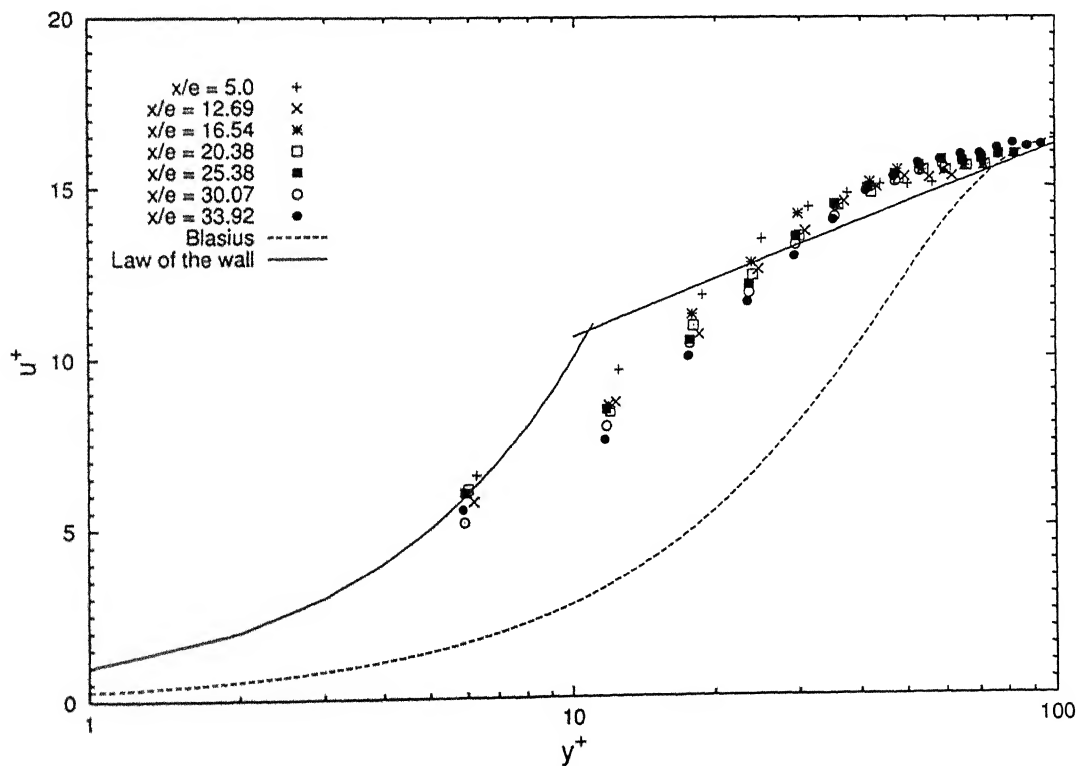


Figure 4.2: Variation of u^+ with y^+ on the bottom surface of the smooth channel at $Re=20900$

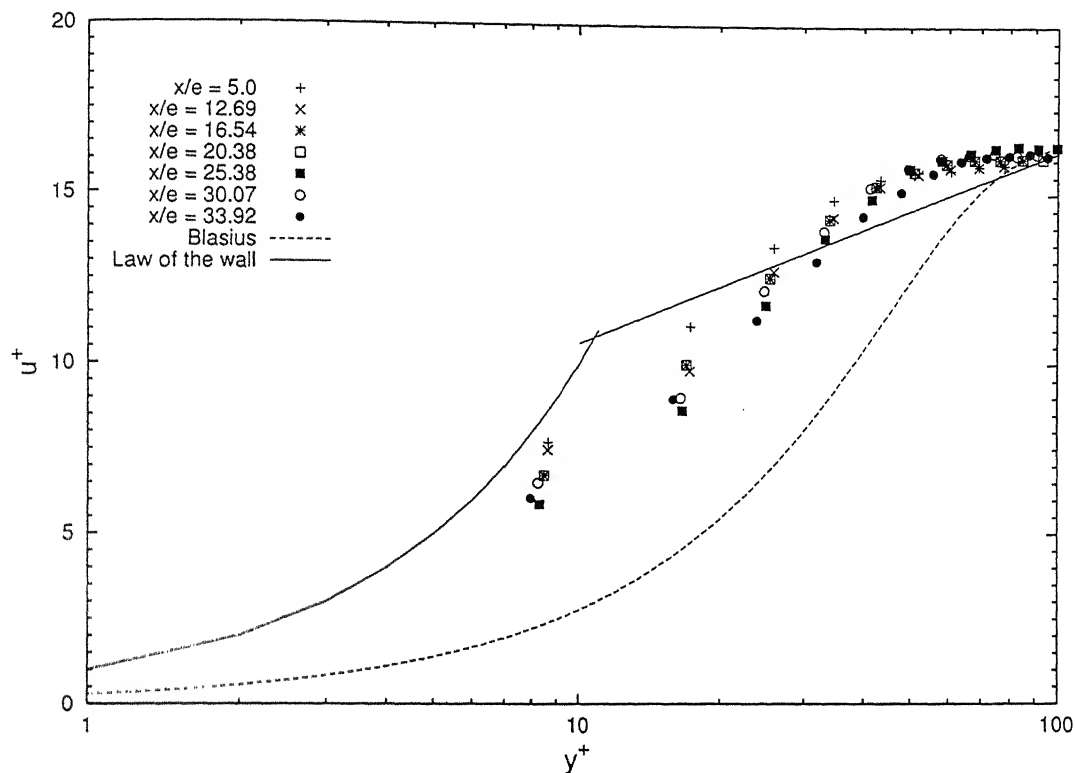


Figure 4.3: Variation of u^+ with y^+ on the bottom surface of the smooth channel at $Re=29400$

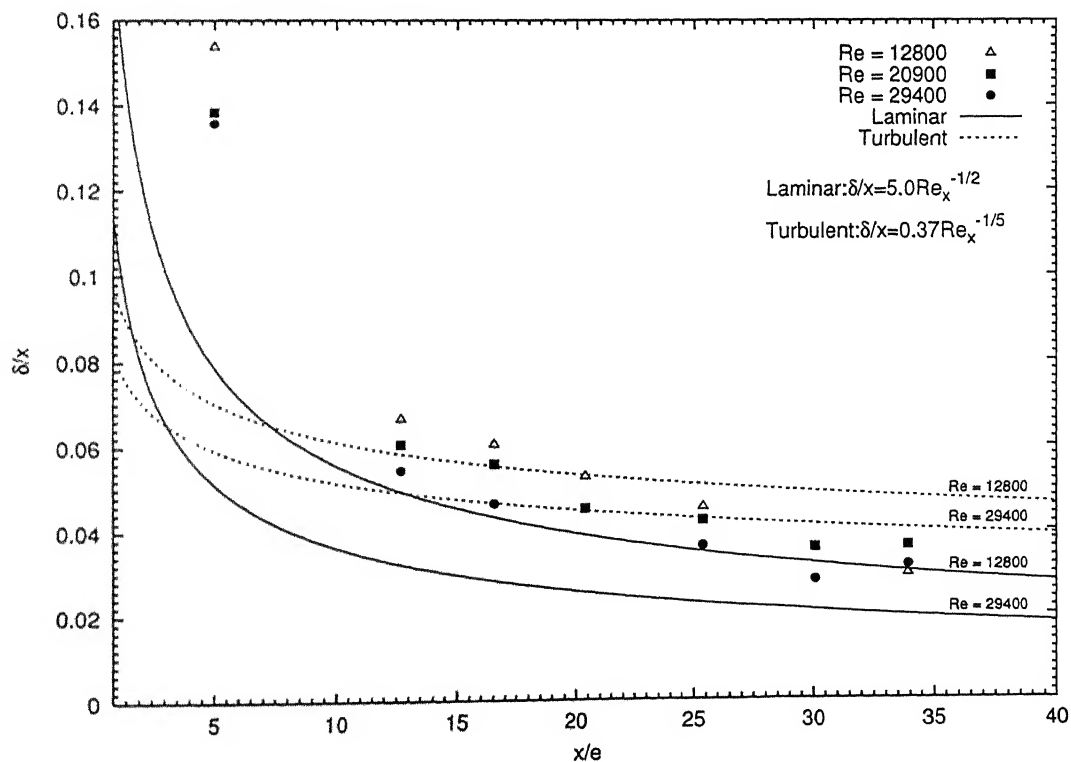


Figure 4.4: Variation of the velocity boundary-layer thickness on the bottom surface of the smooth channel

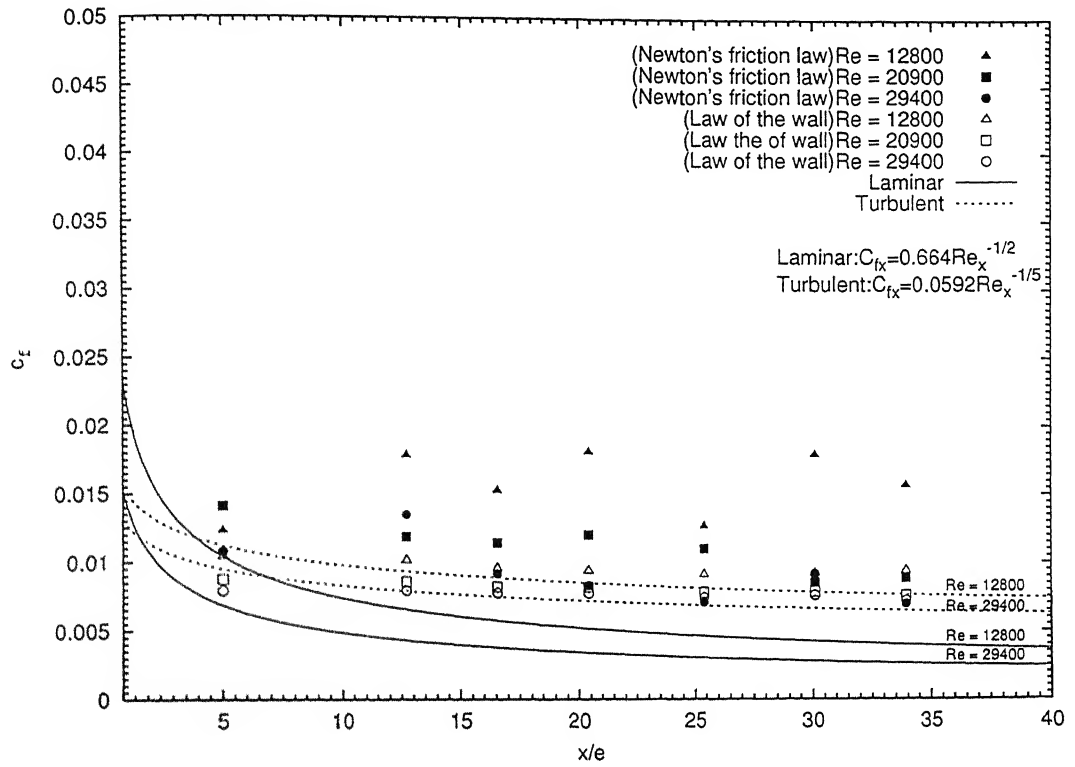


Figure 4.5: Skin friction coefficient on the bottom surface of the smooth channel

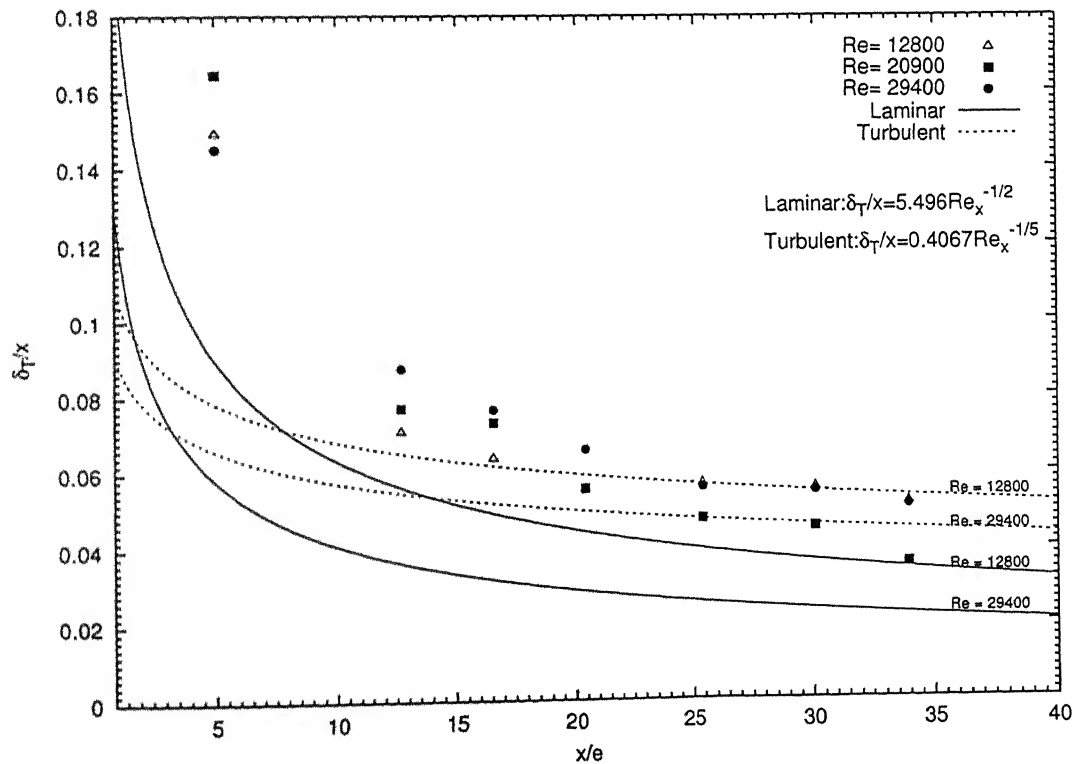


Figure 4.6: Variation of the thermal boundary-layer thickness on the bottom surface of the smooth channel

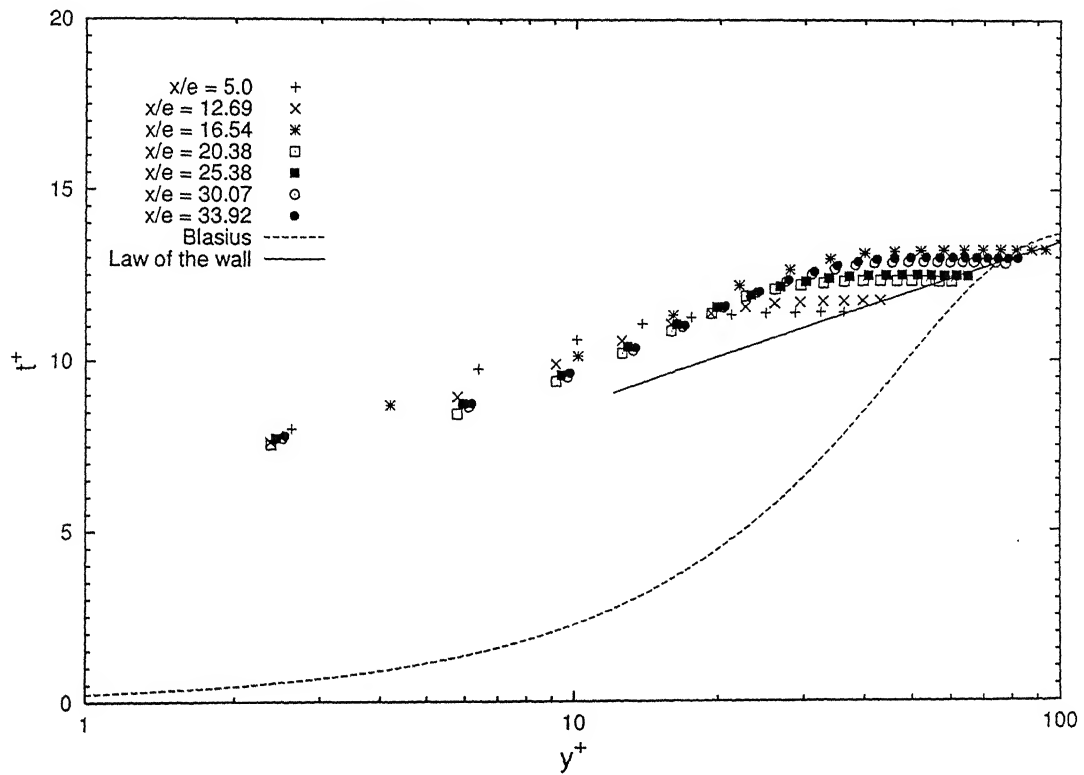


Figure 4.7: Variation of t^+ with y^+ on the bottom surface of the smooth channel at $Re=12800$

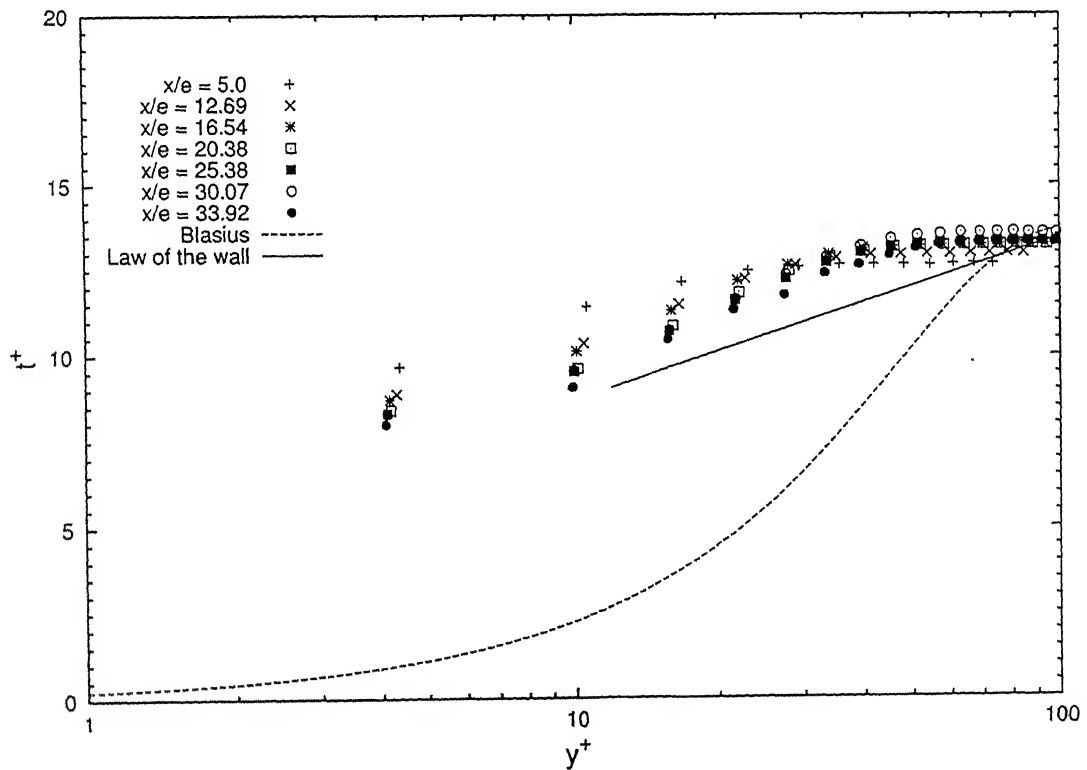


Figure 4.8: Variation of t^+ with y^+ on the bottom surface of the smooth channel at $Re=20900$

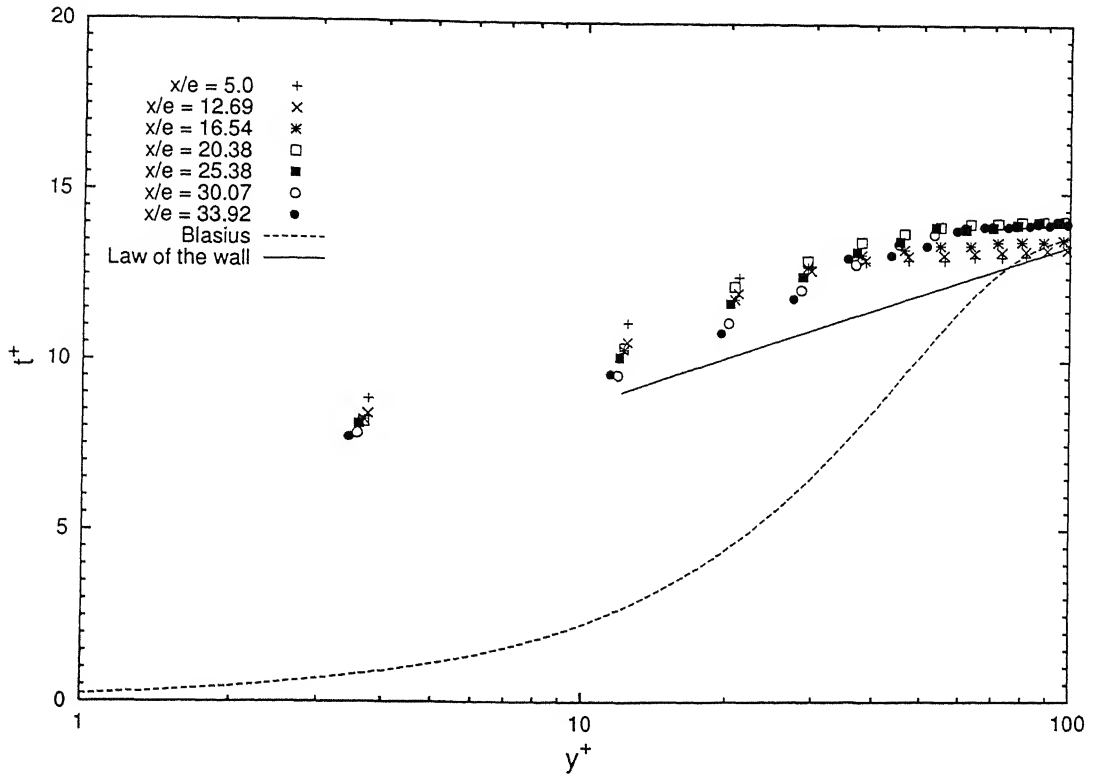


Figure 4.9: Variation of t^+ with y^+ on the bottom surface of the smooth channel at $Re=29400$

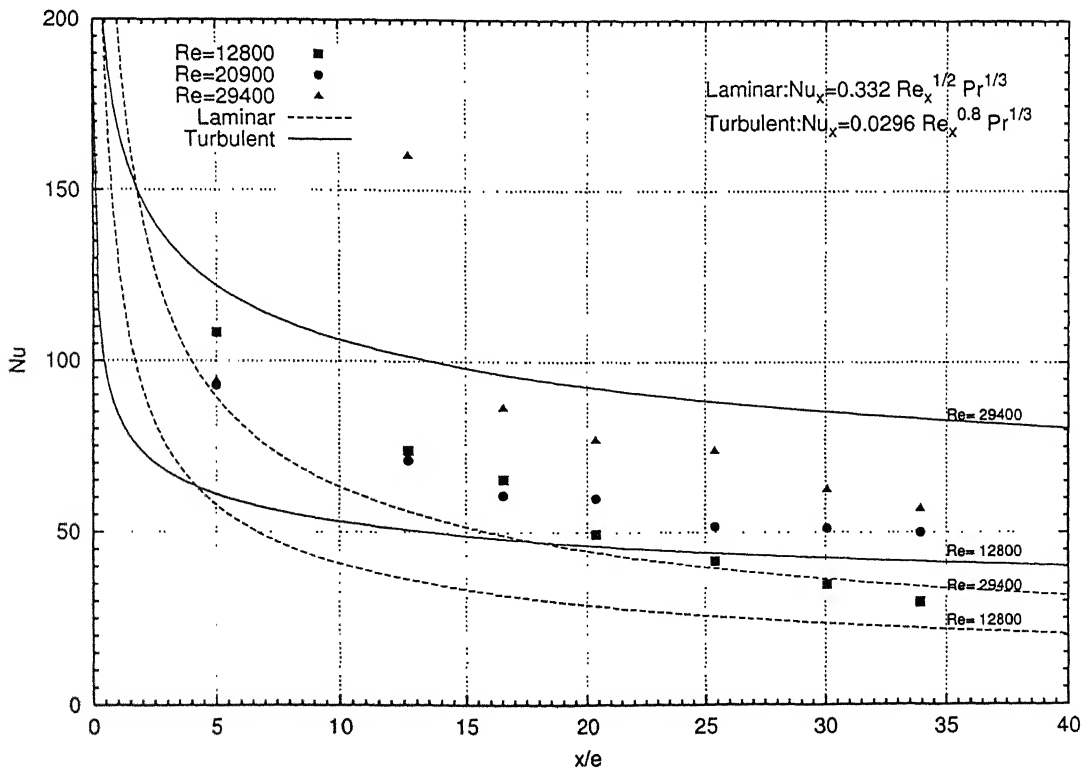


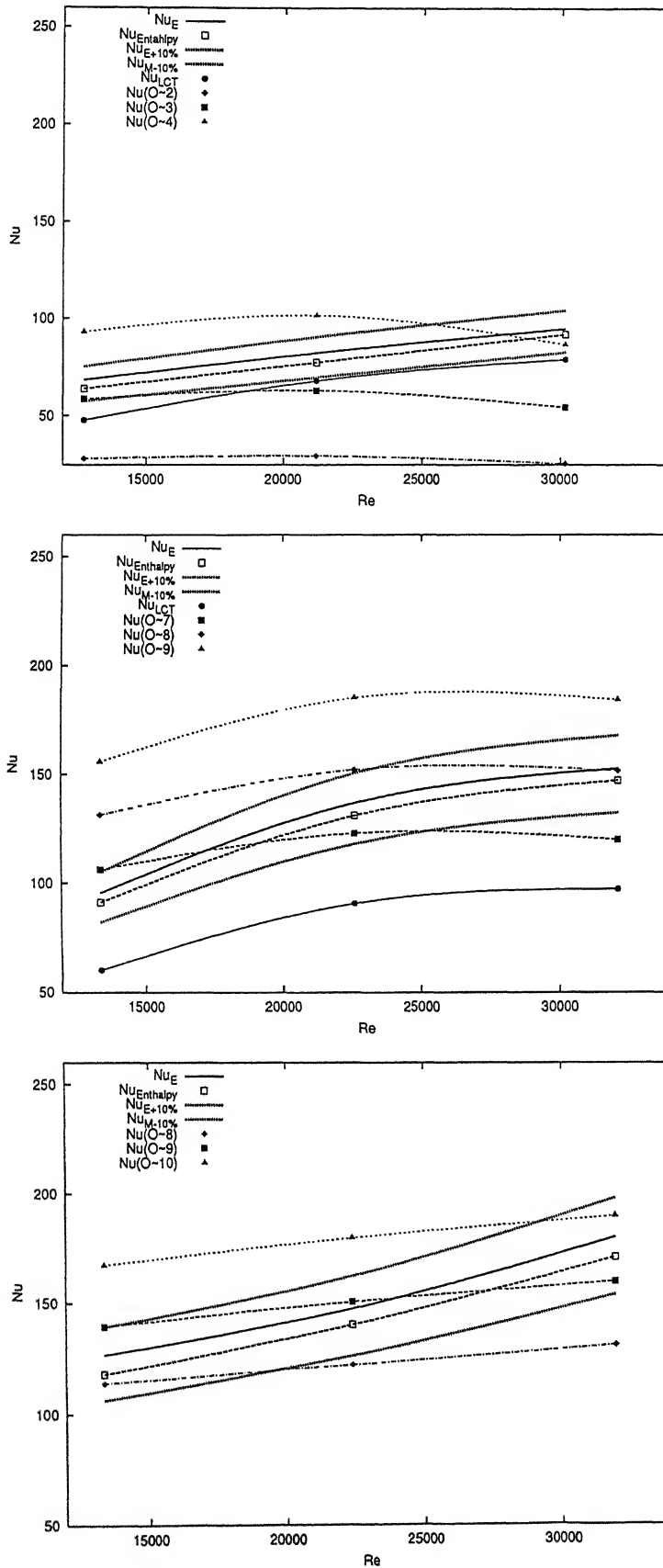
Figure 4.10: Local Nusselt number variation on the bottom surface of the smooth channel

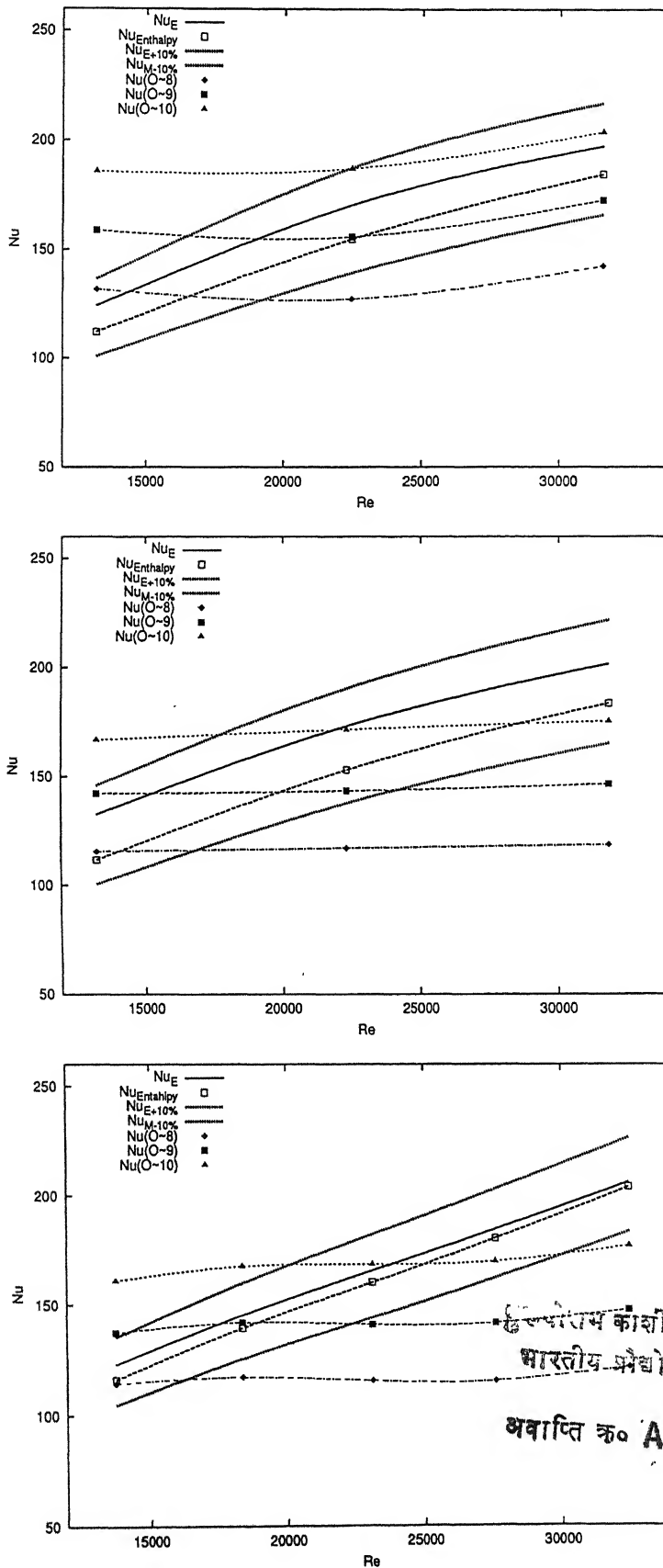
4.2 Nusselt Number from Temperature Profile

The boundary condition of the heated bottom surface of the channel is of constant temperature type with maximum variation of 2 °C to 3 °C. To determine the Nusselt number at any location on the surface, local heat flux or in other words temperature gradient is needed. In the earlier studies with similar boundary conditions and measurements [24], [14], temperature gradient at any particular location is calculated by fitting a second order polynomial through the data points including the wall temperature in the near wall region. But during the present study, it has been observed that no single order of polynomial fit is successful in predicting the Nusselt number behaviour as expected for some known solutions like the law of the wall or Blasius solution for the flow over the flat plate. It is because of this reason, a detailed study has been carried out to comment on the curve fitting procedure for Nusselt number determination from the temperature profile.

Nusselt number calculated using energy balance is taken as a reference because it is the most basic approach with minimal uncertainty, to calculate the average Nusselt number for the whole bottom surface. Flow enthalpy approach is also used to find out the percent error because of the unaccounted losses. A bandwidth has been made by plotting $\pm 10\%$ lines from the energy balance. The different plots of average Nusselt numbers using different orders of polynomials, starting from second order to tenth order has been drawn in the Figures 4.11, 4.12 and 4.13. The first point which is very obvious from the plots is that for no-rib case the points lying within the prescribed bandwidth are of lower order polynomials, namely second, third and fourth while as we move to the one-rib and two-rib cases, the higher order polynomials are lying in the bandwidth. This is because of the fact that for flat plate, the variation of temperature from the surface to the free stream is very smooth and also the boundary layer thickness is small. On the other hand, for one-rib and two-rib cases where boundary layer thickness is quite large as compared to no-rib case and also the temperature profile is not smooth. In such cases, all the points within the boundary layer have the effect on temperature gradient at the wall and so the curve must pass through all the data points. This is why the higher order polynomials would predict the best result. The second point which is clear from the plots is that no single order poly-

nomial is lying within the bandwidth while looking at different Reynolds number. In fact, one single order is contradicting the basic behavior as obtained from the energy balance. Hence no generalization could be made for it. In the present work, the points which are lying within the bandwidth are chosen irrespective of the order of the polynomial i.e. no single order of polynomial is followed for any case. Thirdly, it can be seen that when moving towards the higher heating levels or in other words higher wall temperature cases, the percentage error in the Nusselt number calculated from energy balance and that from flow enthalpy is increasing. It is because of unaccounted losses are becoming higher as heat loss from side walls are not negligible. Detailed discussion on the effect of heating level is presented in the subsequent sections.

Figure 4.11: Variation of average Nu with Re for (TOP) no-rib case at $Q=69$ W,

Figure 4.12: Variation of average Nu with Re for (TOP) one-rib case at $Q=132.8$

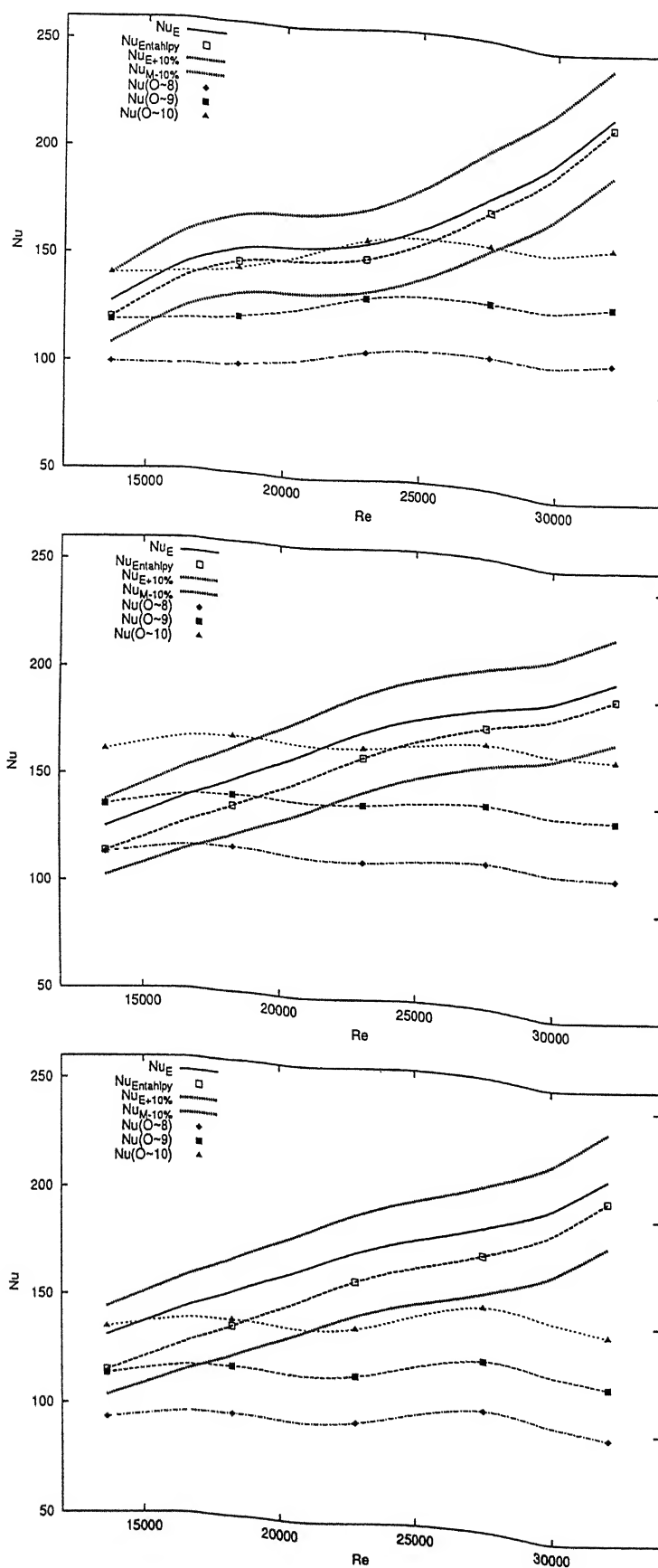


Figure 4.13: Variation of average Nu with Re for (TOP) two-rib case at $Q=132.8$ W, (MIDDLE) two-rib case at $Q=132.8$ W (BOTTOM) two-rib case at $Q=89.7$ W

4.3 Effect of Heating Level

In the present study, the temperature data were collected at four different heating levels i.e. four different constant wall temperature conditions at a particular Reynolds number. The effect of heating level on Nusselt number and boundary layer thickness is discussed in the present section. The average Nusselt number calculated from energy balance at different heating levels is presented in the table 4.1.

Table 4.1: Average Nusselt number at different heating levels

Configuration	Q (W)	Re= 12800	Re= 15950	Re= 20900	Re= 23900	Re= 29400
One-rib	69.0	109.0		155.4		179.6
	89.7	126.6		147.6		179.9
	132.8	124.1		170.1		197.2
	204.0	132.6		172.9		201.3
Two-rib	69.0	122.9	145.4	165.6	184.8	205.9
	89.7	127.4	154.4	160.0	186.2	230.0
	132.8	125.2	148.7	174.5	189.4	208.2
	204.0	131.0	152.7	174.6	190.2	218.5

It may be concluded that the average Nusselt number calculated by energy balance method is not significantly dependent on heating level. In only few cases, particularly at Re=20900 and 29400 there is a significant increase in the value of the Nusselt number for $Q=132.8$ W in comparison to $Q=89.7$ W. The reason for this might be the fact that there is a large difference between these two heating levels and as it is discussed in the previous section, at higher heating levels, unaccounted losses are more and so the predicted values of Nusselt number will be on the higher side than the actual values. The other factor of importance at higher heating level is the change in the properties of the working fluid i.e air at a higher temperature.

Similar observations could be made from the plots showing the variation of non dimensionalized thermal boundary layer thickness with x/e for one-rib case in Figures 4.14, 4.15 and 4.16. It is apparent from the plots that there is

no definite relationship between thermal boundary layer thickness and heating level. For a given Reynolds number δ_T is lying within a certain range and this range could be because of the uncertainty associated with the measurement of boundary layer thickness.

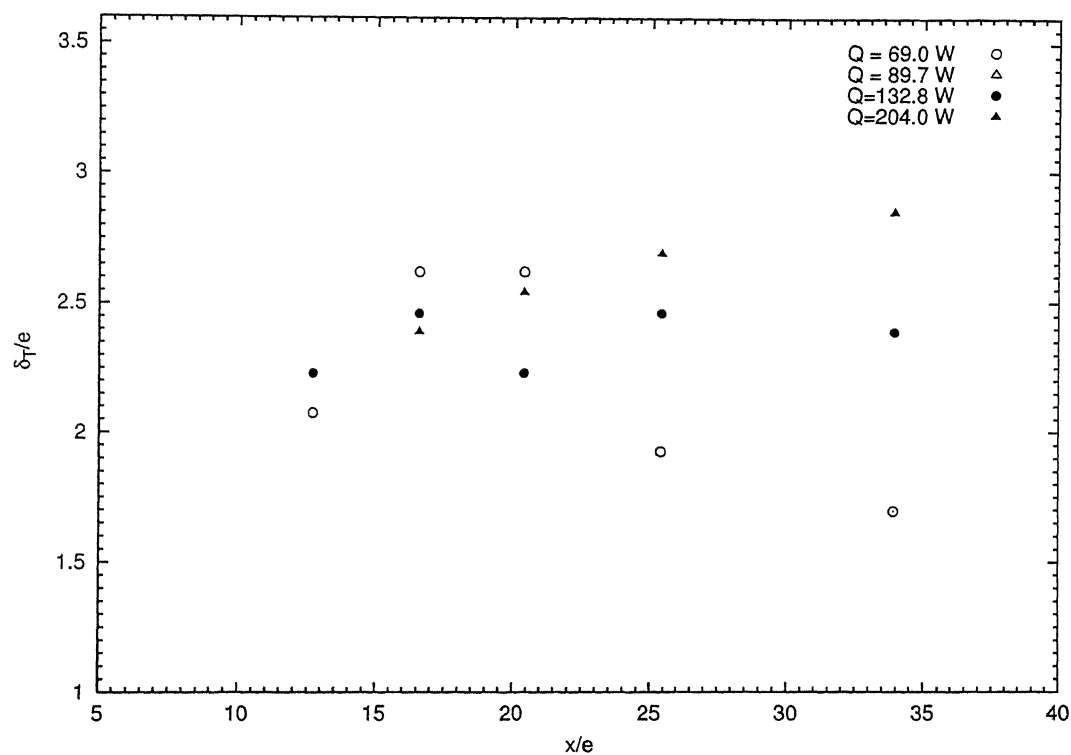


Figure 4.14: Comparison of thermal boundary layer thickness at all heating levels for one-rib case and $Re=12800$

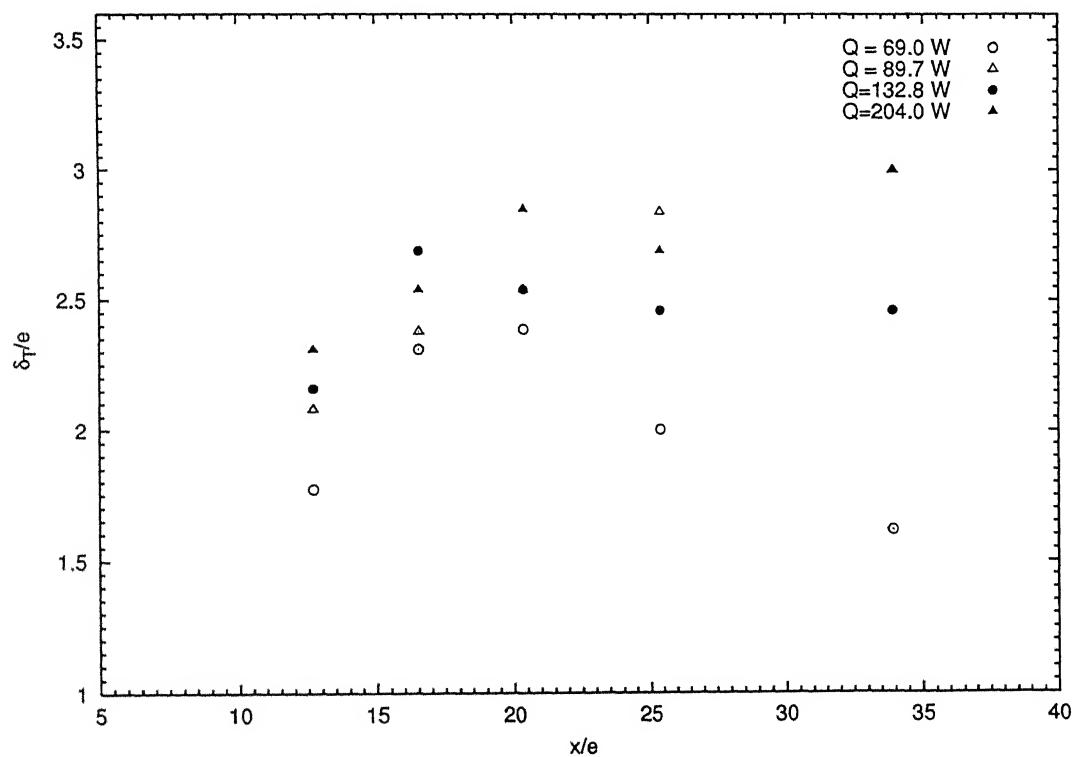


Figure 4.15: Comparison of thermal boundary layer thickness at all heating levels for one-rib case and $Re=20900$

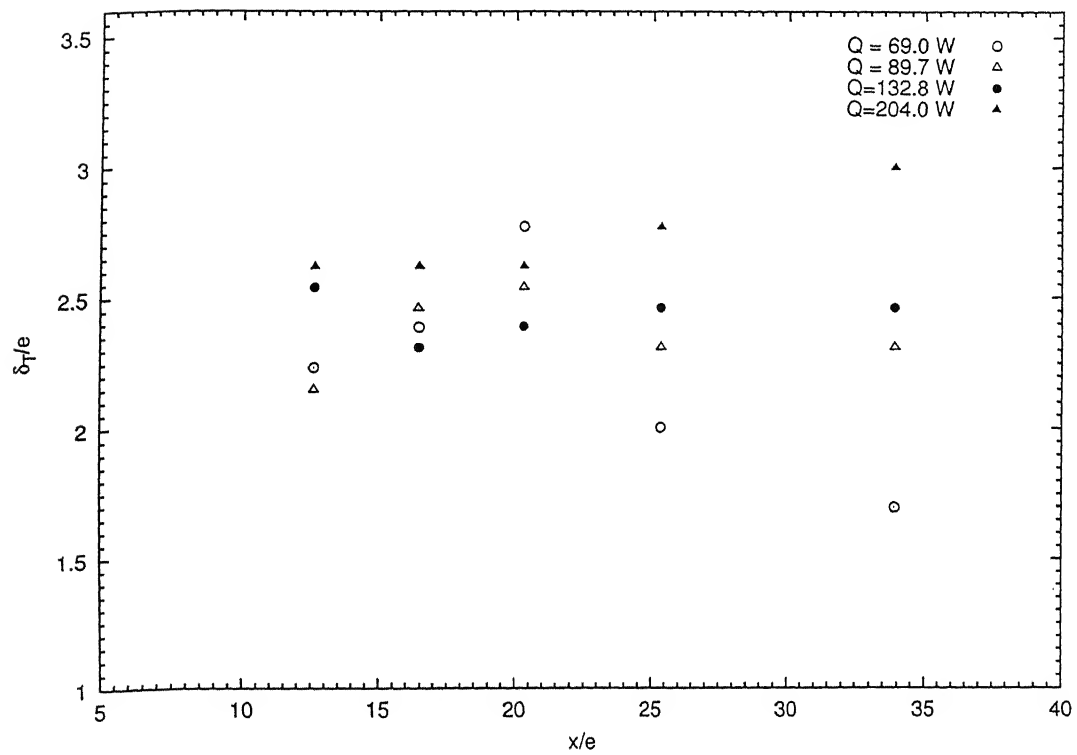


Figure 4.16: Comparison of thermal boundary layer thickness at all heating levels for one-rib case and $Re=29400$

4.4 Comparison of No-rib, One-rib and Two-rib cases

The comparison of the one-rib and two-rib case with respect to the smooth channel is presented in the following sections with the help of mean and fluctuating velocity field, mean and fluctuating thermal field, boundary layer parameters, transient surface temperature visualization from LCT, span-wise average Nusselt number and transition data of boundary layer.

4.4.1 Velocity Field

Figure 4.17, 4.17 and 4.19 shows the variation of u/U_{avg} with y/e at various stream-wise locations at different Reynolds number. Where U_{avg} denotes the average stream-wise velocity the channel. For the no-rib case, velocity increase away from the wall is smooth and gradual. The velocity boundary layer thickness is increasing in the downstream direction, though, the increase is very nominal at farther downstream locations. In case of one-rib and two-rib, the increase in the velocity at the first downstream location of the rib i.e. $x/e=12.69$, is very slow initially and there is a sudden change at about $y/e = 1.0$. This may be due to the presence of stagnant region till y equal to the rib height. In case of one-rib, the velocity profile at subsequent downstream locations seems to be approaching the fully developed condition. In the case of two-rib, the effect of second rib seen at location $x/e=30.07$, which is almost the corresponding location from the second rib as compared to the location $x/e=12.69$, from the first rib, no sharp change in stream-wise velocity can be observed. The boundary layer thickness is increasing very rapidly due to the presence of ribs. There is a very significant increase when comparing the no-rib with the one-rib case but it is not as significant when comparing the one-rib with the two-rib case. This shows that momentum transport is enhanced in ribbed cases quite significantly. Overall, the boundary layer grows more rapidly for the two-rib case in comparison to the one-rib case indicating greater momentum transport.

Variation of cross-stream velocity v/U_{avg} at same stream-wise locations are shown in Figures 4.20, 4.21 and 4.22. The v -velocity magnitude for the no-rib case is observed to be smaller with that with the rib case. For the one-rib case the

maximum magnitude of the v -velocity increases in the streamwise direction which subsequently decreases in magnitude. This is primarily due to the redevelopment of the boundary layer after reattachment.

In Figures 4.23, 4.24 and 4.25, variation of u_{rms} for all three cases at different Reynolds number are shown. The u_{rms} for the no-rib case shows a lower magnitude at close to the wall with gradual increase to the free stream value, indicating the effect of the boundary condition $u' = 0$, at close to the wall and no significant turbulence production inside the boundary layer. In the one-rib case, the rms velocity is highest inside the core of the boundary layer with subsequent decrease to the free-stream value. The maximum value of rms velocity is decreasing when moving in the stream-wise direction for one-rib case. In comparison, for the two-rib case, the u_{rms} increases for the second time after the second rib i.e. at $x/e = 30.07$, but it is marginal as compared to that after the first rib. Overall, the average turbulence level is highest for the two-rib case and lowest for the no-rib case. The variations of v_{rms} is also shown in the Figures 4.26, 4.27 and 4.28.

Figure 4.29 shows the comparison of non-dimensionalized velocity boundary layer thickness for no-rib, one-rib and two-rib cases. It can be clearly seen that presence of ribs, increase the boundary layer thickness considerably, and it is more for two-rib than one-rib case. This shows how the turbulence is increased with the introduction of ribs.

4.4.2 Boundary Layer Parameters

In this section, various boundary layer parameters e.g. displacement thickness, momentum thickness, shape factor (ratio of displacement and momentum thickness), which gives the idea about the shape of the velocity profile i.e. flatness and vorticity thickness and their effect are discussed. These parameters are presented in the Tables 4.2, 4.3, 4.4 for no-rib, one-rib and two-rib cases respectively.

For the no-rib case, both displacement and momentum thickness are increasing as we move from downstream, making the shape factor to remain almost constant when looking at any particular Reynolds number. Since the value of shape factor for laminar flow is $H = 2.6$ (Blasius) and for turbulent flow, it is about $H = 1.29$ (assuming $(1/7)^{th}$ power law), it can be said that for no-rib

case is not fully turbulent though it is very close when we look at the Figures 4.49(TOP), 4.51(TOP), 4.53(TOP). Vorticity thickness is reducing with the increase in the Reynolds number indicating the increase in the shear stress at the wall because the maximum gradient in the stream-wise velocity is observed to be at the wall for all three Reynolds number and stream-wise locations under study.

When comparing the one-rib and two-rib cases with no-rib case, it can be observed that there is a large increase in the displacement and momentum thickness with the values being highest for the two-rib case. A very high value of shape factor at the first downstream location after the first rib for both one-rib and two-rib case, indicates that flow is separated. But, when moving further downstream, the value of shape factor is approaching that for the turbulent flow. This fact is also confirmed when looking at the Figures 4.49; 4.51 and 4.53. Highest velocity gradient at a location slightly higher than the rib height at the location just after the first rib also confirms the condition of separated flow. The separation is not seen after the second rib for two-rib case, except for the case of lowest Reynolds number. The values of vorticity thickness are quite high at first few downstream locations but it lower at farther downstream locations, showing the increase in the wall shear stress for the one-rib case. Though, for the two-rib case, values of vorticity thickness are not very low and in fact they are comparable with the no-rib case.

For the smooth channel case, there is no change in the shape factor in the downstream direction. For the one-rib and two-rib case, there is a gradual drop in shape factor in the downstream direction approaching a constant value in the far field region. For the one-rib case the shape factor in the far field region is lowest at the highest Reynolds number ($Re=29400$) in comparison to that at $Re=12800$ and 20900 . The far field region shape factor for the two-rib case is higher in comparison to that for the one-rib case. This may be due to the presence of the second rib and thus the developing length of the boundary layer is smaller for the two-rib case than that of the one-rib case and boundary layer has not reached equilibrium.

4.4.3 Thermal Field

The non-dimensional temperature profiles at different stream-wise locations are shown in Figures 4.30, 4.31 and 4.32. Similar to the velocity profile, the temperature profiles for no-rib case has a smooth variation in the near wall region. The thermal boundary layer thickness is higher than the corresponding boundary layer thickness as the Prandtl number is less than unity. There is a significant increase in the thermal boundary layer thickness for the one-rib and two-rib cases in comparison to the no-rib case; the two-rib case has the maximum increase. For all the cases, at very close to the bottom surface, a sharp drop in temperature is observed contrary to the gradual increase in the velocity, observed in the velocity boundary layer case, indicating the predominance of the diffusion mechanism. The effect of ribs on temperature is very similar to that of velocity profile, discussed in the earlier section.

The non-dimensional *rms* temperature profile has different nature of variation in comparison to the *rms* velocities, as shown in the Figures 4.33, 4.34 and 4.35. The *rms* of temperature fluctuation is observed to be higher in the near wall region for all cases i.e. no-rib, one-rib and two-rib case. Comparing the *rms* temperature profile with *rms* velocity profile at $x/e = 12.69, 16.54$ for one-rib and two-rib cases, a second peak in the *rms* temperature profile is observed at same y/e location. This indicates some degree of correlation between the velocity and temperature in this region. Overall, the temperature fluctuations is observed to be highest in the near wall region where the temperature gradient is the highest.

Similar to the velocity boundary layer thickness, comparison of thermal boundary layer thickness for all three cases are shown in Figure 4.36. The changes in temperature boundary layer thickness on the introduction of ribs is very similar to that of velocity boundary layer thickness at $Re=12800$ and 20900 . At $Re=29400$, the velocity boundary layer for the one-rib and two-rib cases are different, while the thermal boundary layer is not different from each other.

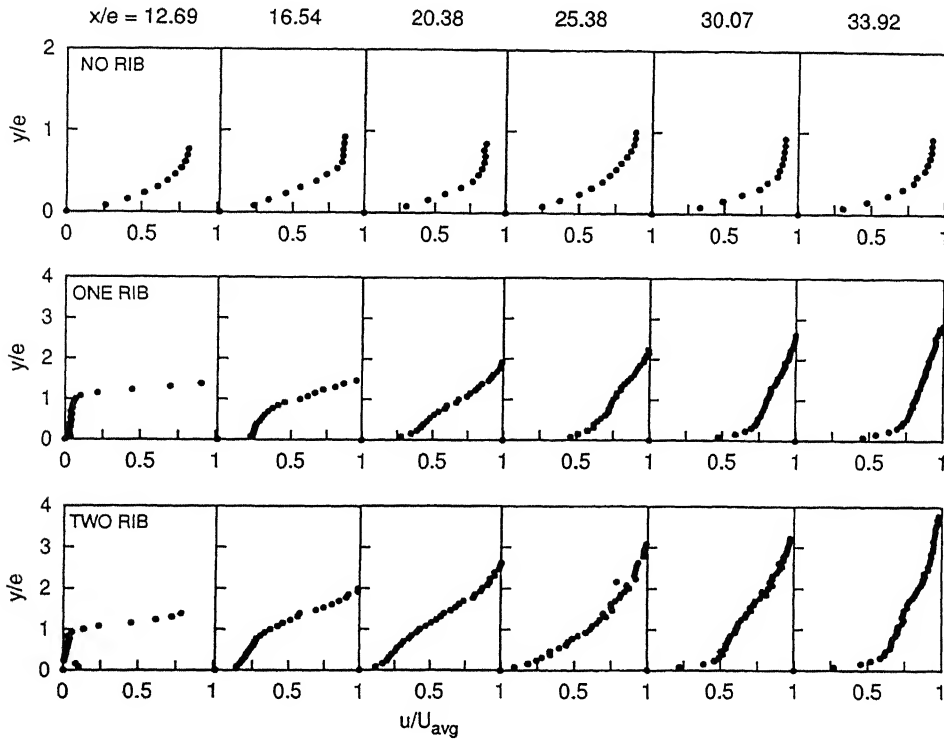


Figure 4.17: Comparison of stream-wise velocity variation for all three cases at $Re=12800$

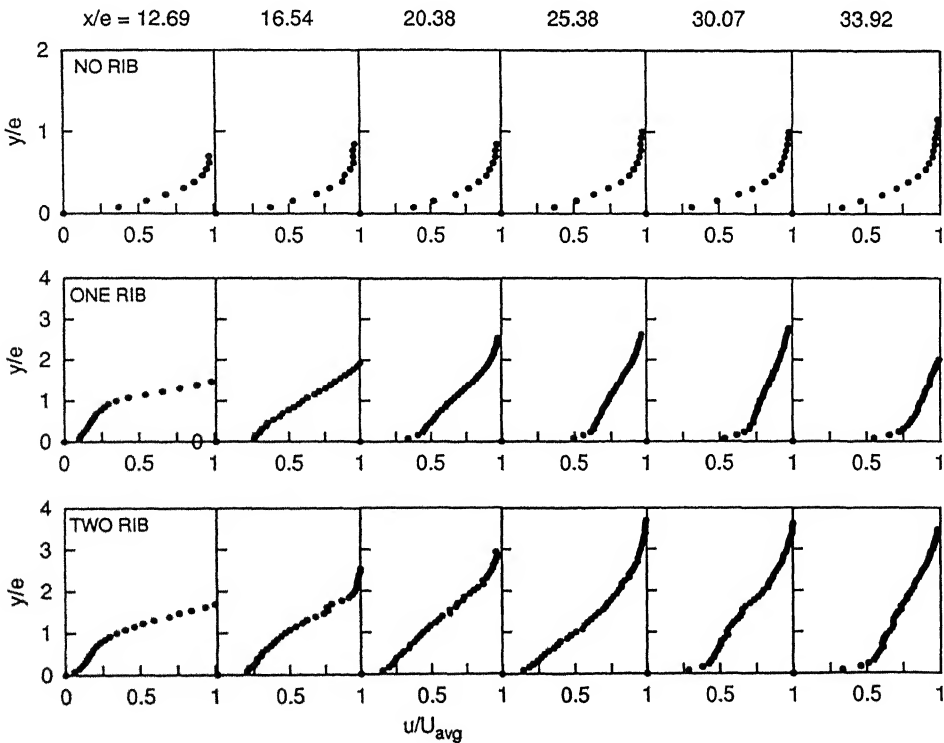


Figure 4.18: Comparison of stream-wise velocity variation for all three cases at $Re=12800$

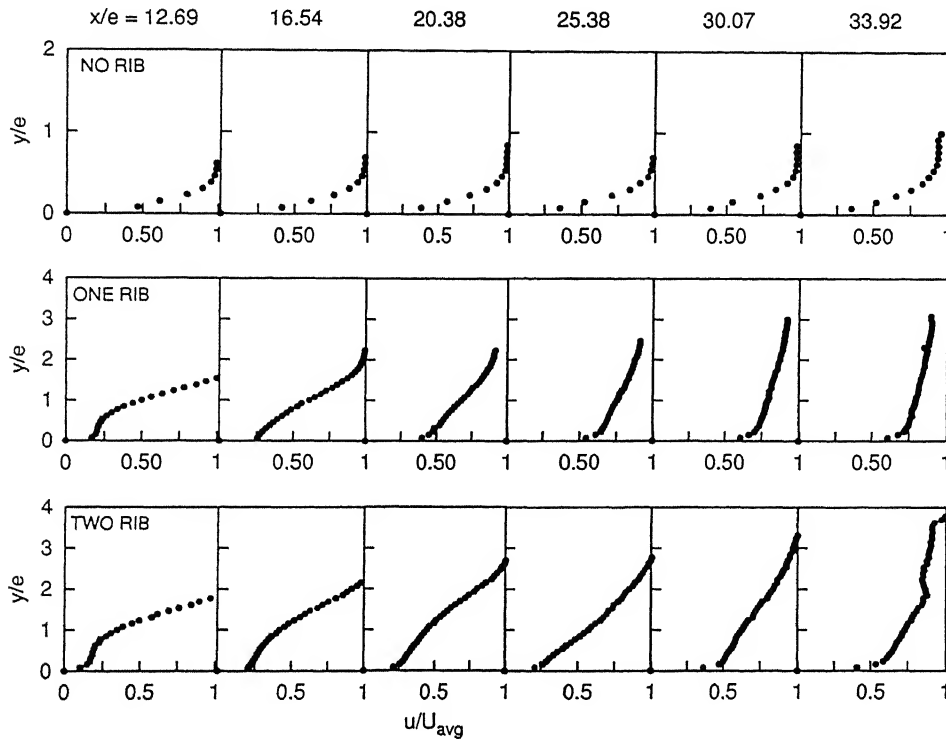


Figure 4.19: Comparison of stream-wise velocity variation for all three cases at $Re=29400$

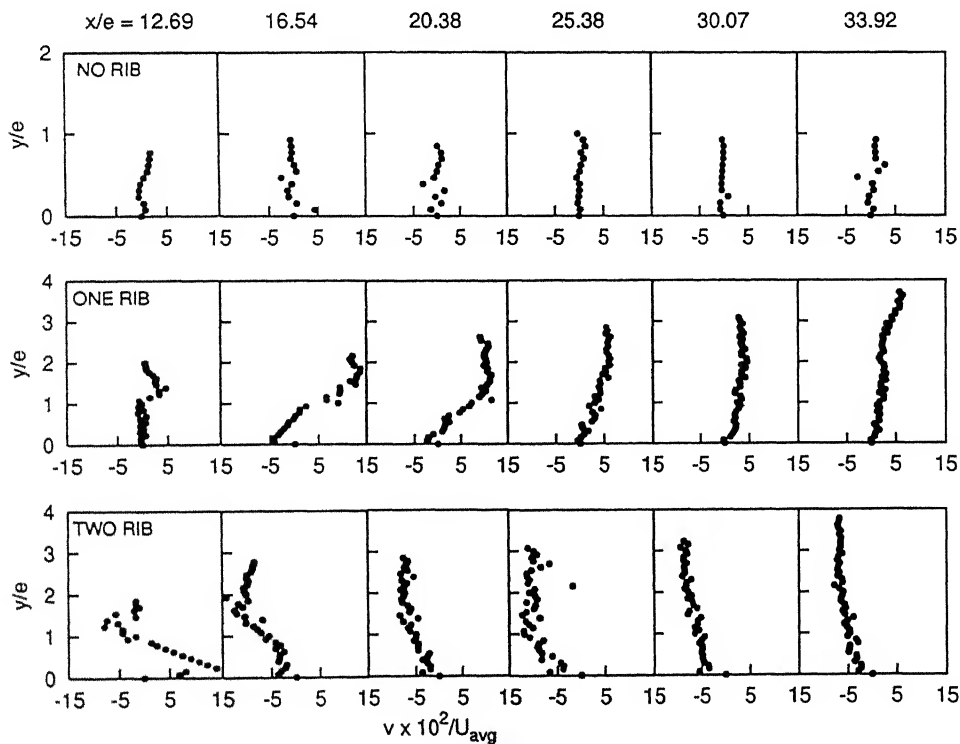


Figure 4.20: Comparison of cross-stream velocity variation for all three cases at $Re=29400$

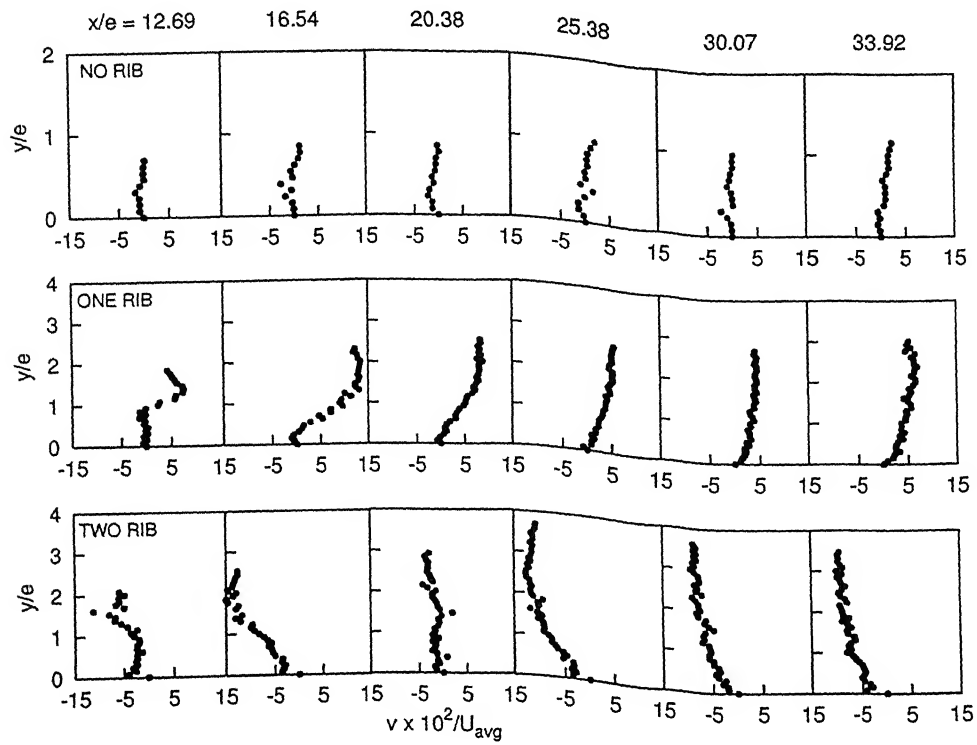


Figure 4.21: Comparison of cross-stream velocity variation for all three cases at $Re=20900$

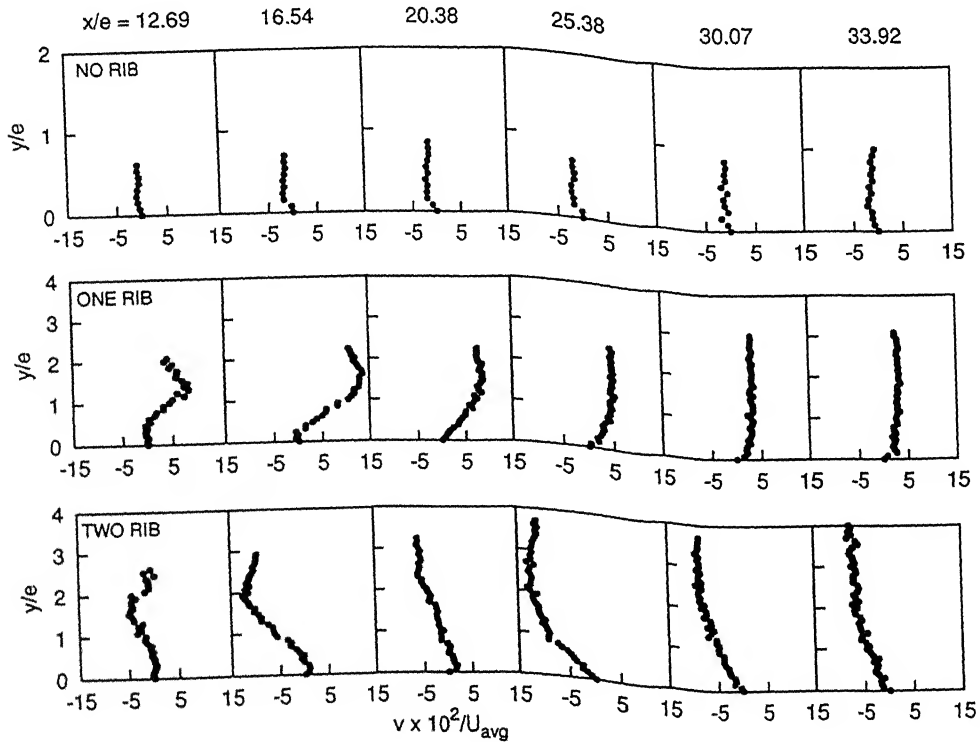


Figure 4.22: Comparison of cross-stream velocity variation for all three cases at $Re=29400$

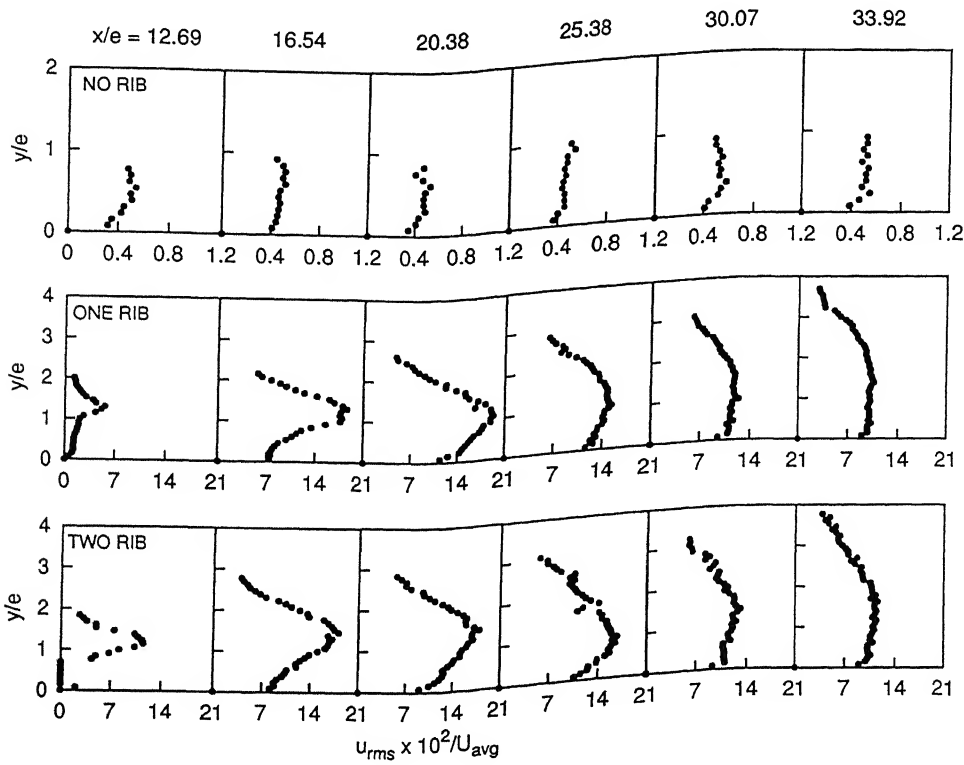


Figure 4.23: Comparison of u_{rms} variation with y for all three cases at $Re=12800$

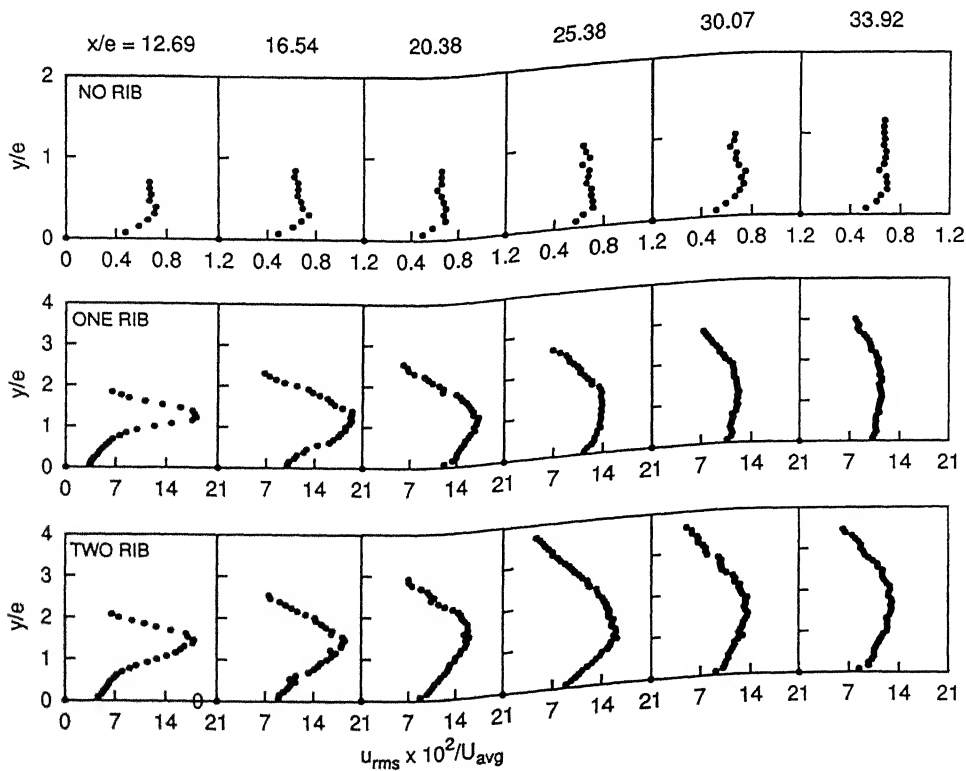
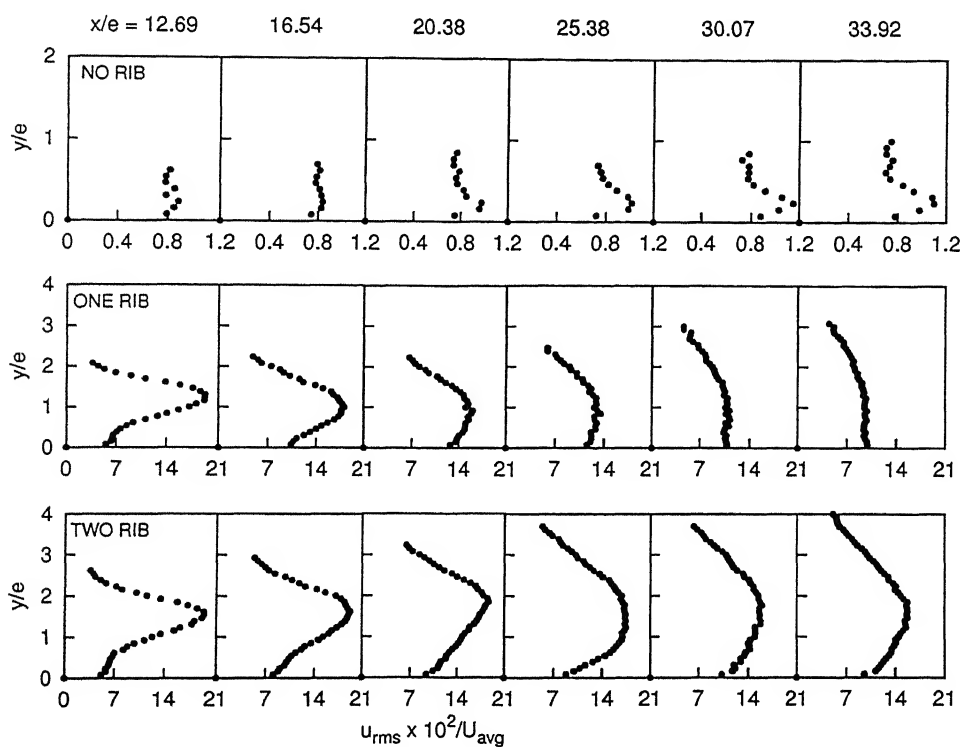
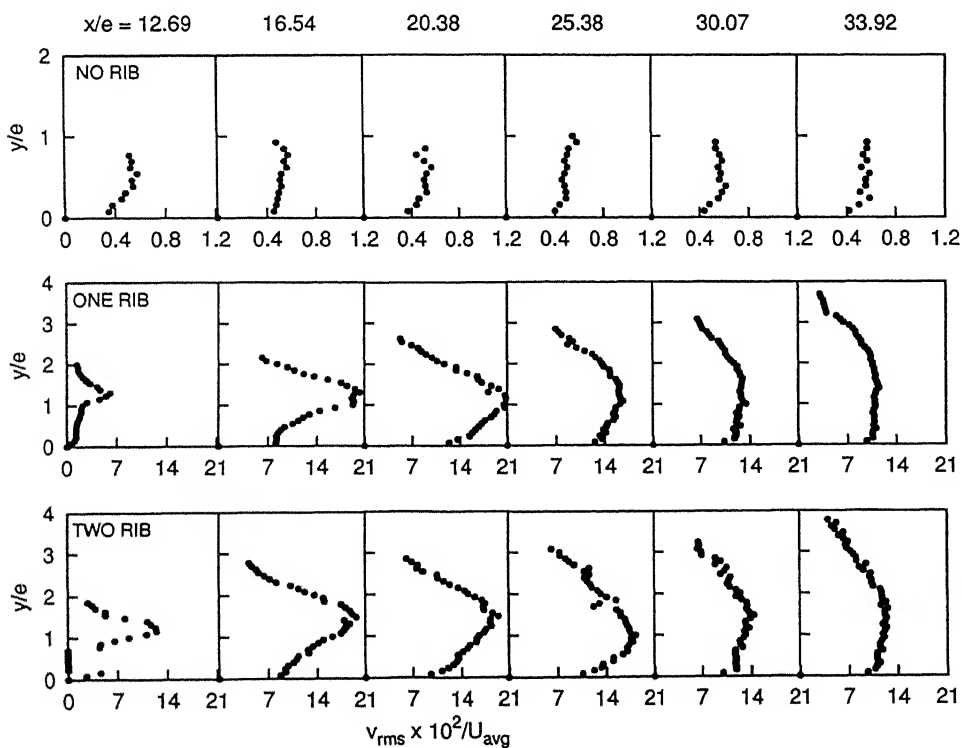
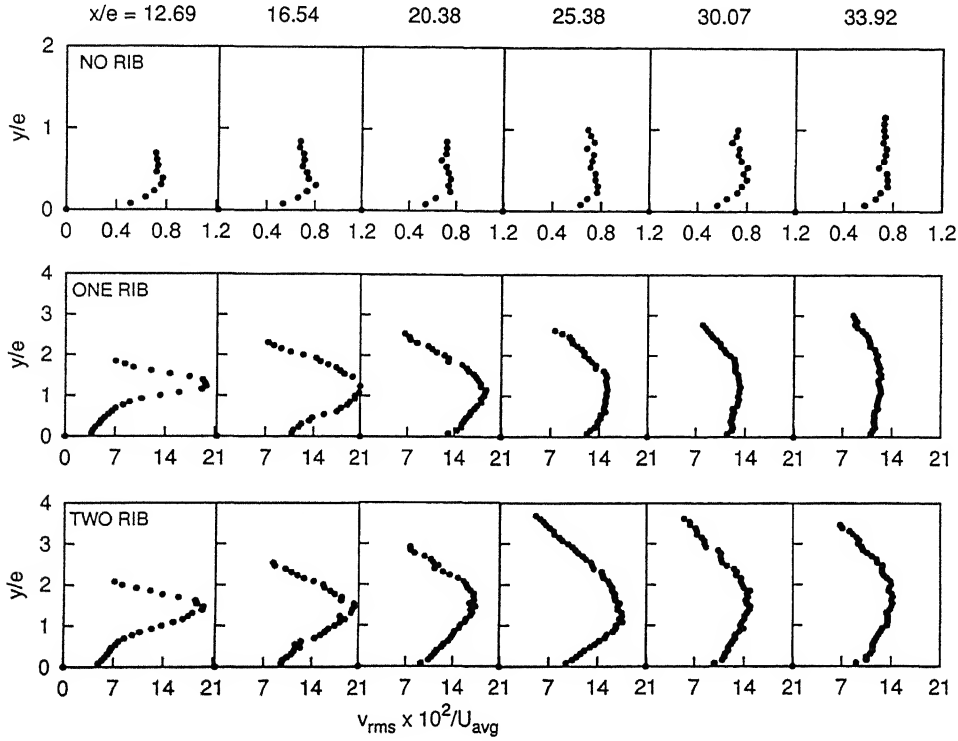
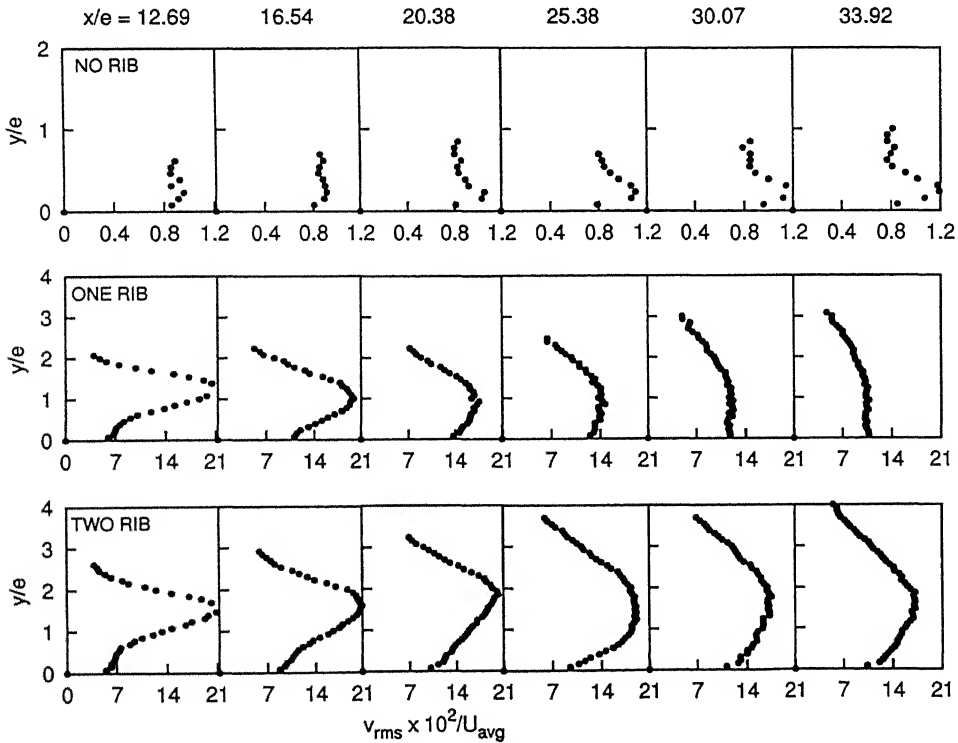


Figure 4.24: Comparison of u_{rms} variation with y for all three cases at $Re=20900$

Figure 4.25: Comparison of u_{rms} variation with y for all three cases at $Re=29400$ Figure 4.26: Comparison of v_{rms} variation with y for all three cases at $Re=12800$

Figure 4.27: Comparison of v_{rms} variation with y for all three cases at $Re=20900$ Figure 4.28: Comparison of v_{rms} variation with y for all three cases at $Re=29400$

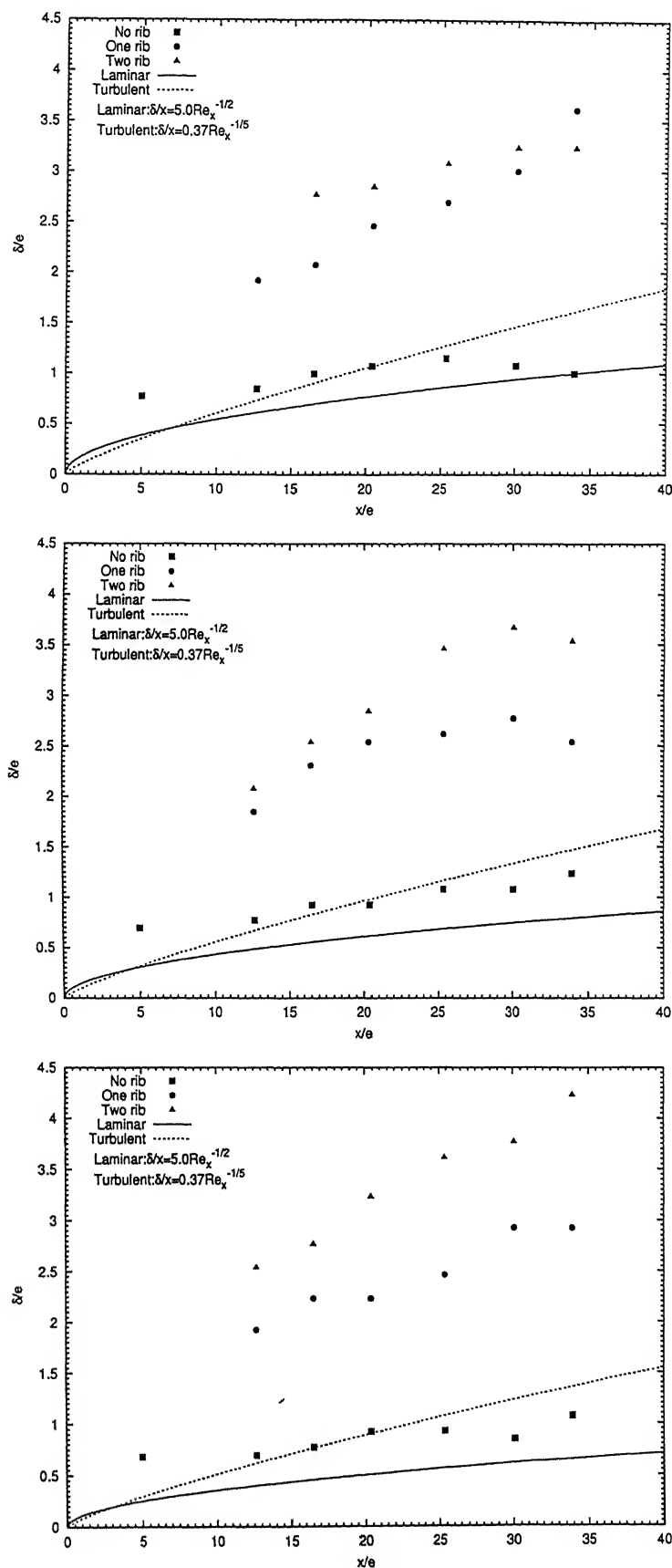


Figure 4.29: Variation of velocity boundary layer thickness with x/e for all three cases. The figure is a comparison of the experimental results with the theoretical curves for laminar and turbulent flow.

Table 4.2: Boundary layer parameters at different Reynolds number for the no-rib case at (a) Re=12800, (b) Re=20900 and (c) Re=29400

$\frac{x}{e}$	δ (mm)	δ^* (mm)	θ (mm)	δ_ω (mm)	$H = \frac{\delta^*}{\theta}$	$Y_{(\frac{\partial u}{\partial y})_{\max}}$ (mm)
05.00	10.00	2.26	0.97	3.20	2.33	0.00
12.69	11.00	2.73	1.26	3.13	2.17	0.00
16.54	13.00	3.19	1.34	3.67	2.00	0.00
20.38	14.00	2.46	1.12	2.91	2.19	0.00
25.38	15.00	3.45	1.64	3.54	2.10	0.00
30.07	14.00	2.42	1.14	2.74	2.13	0.00
33.92	13.00	2.59	1.21	2.97	2.13	0.00

(a)

$\frac{x}{e}$	δ	δ^*	θ	δ_ω	$H = \frac{\delta^*}{\theta}$	$Y_{(\frac{\partial u}{\partial y})_{\max}}$
05.00	9.00	1.82	0.81	2.31	2.25	0.00
12.69	10.00	2.21	1.00	2.65	2.21	0.00
16.54	12.00	2.25	1.05	2.58	2.15	0.00
20.38	12.00	2.39	1.15	2.55	2.09	0.00
25.38	14.00	2.56	1.25	2.64	2.06	0.00
30.07	14.00	2.74	1.30	3.08	2.11	0.00
33.92	16.00	2.96	1.44	2.93	2.06	0.00

(b)

$\frac{x}{e}$	δ	δ^*	θ	δ_ω	$H = \frac{\delta^*}{\theta}$	$Y_{(\frac{\partial u}{\partial y})_{\max}}$
05.00	9.00	1.58	0.70	2.06	2.27	0.00
12.69	9.00	1.76	0.79	2.12	2.24	0.00
16.54	10.00	1.87	0.83	2.39	2.26	0.00
20.38	12.00	1.87	0.84	2.39	2.26	0.00
25.38	12.00	2.24	0.99	2.80	2.27	0.00
30.07	11.00	2.04	0.89	2.50	2.28	0.00
33.92	14.00	2.59	1.28	2.75	2.02	0.00

(c)

Table 4.3: Boundary layer parameters at different Reynolds number for the one-rib case at (a) $Re=12800$, (b) $Re=20900$ and (c) $Re=29400$

$\frac{x}{e}$	δ (mm)	δ^* (mm)	θ (mm)	δ_ω (mm)	$H = \frac{\delta^*}{\theta}$	$Y_{(\frac{\partial u}{\partial y})_{\max}}$ (mm)
12.69	25.00	16.30	1.53	4.75	10.65	16.00
16.54	27.00	12.23	4.12	5.26	2.97	0.00
20.38	32.00	9.39	4.70	3.79	2.00	0.00
25.38	35.00	7.77	4.95	2.24	1.57	0.00
30.07	39.00	6.44	4.44	2.13	1.45	0.00
33.92	47.00	9.90	6.73	2.41	1.47	0.00

(a)

$\frac{x}{e}$	δ	δ^*	θ	δ_ω	$H = \frac{\delta^*}{\theta}$	$Y_{(\frac{\partial u}{\partial y})_{\max}}$
12.69	24.00	14.03	3.21	10.36	4.37	16.00
16.54	30.00	10.96	4.81	4.06	2.28	0.00
20.38	33.00	8.97	4.99	2.90	1.80	0.00
25.38	34.00	6.67	4.47	1.94	1.49	0.00
30.07	36.00	5.83	4.12	1.82	1.41	0.00
33.92	33.00	5.33	3.72	1.91	1.43	0.00

(b)

$\frac{x}{e}$	δ	δ^*	θ	δ_ω	$H = \frac{\delta^*}{\theta}$	$Y_{(\frac{\partial u}{\partial y})_{\max}}$
12.69	25.00	12.54	3.84	6.68	3.27	17.00
16.54	29.00	10.06	4.44	3.87	2.26	0.00
20.38	29.00	7.12	4.25	2.28	1.68	0.00
25.38	32.00	4.94	3.46	1.66	1.42	0.00
30.07	38.00	4.59	3.40	1.51	1.35	0.00
33.92	38.00	4.11	3.06	1.49	1.34	0.00

(c)

Table 4.4: Boundary layer parameters at different Reynolds number for the two-rib case at (a) Re=12800, (b) Re=20900 and (c) Re=29400

$\frac{x}{e}$	δ (mm)	δ^* (mm)	θ (mm)	δ_ω (mm)	$H = \frac{\delta^*}{\theta}$	$Y_{(\frac{\partial u}{\partial y})_{\max}}$ (mm)
12.69	25.00	15.76	1.80	4.64	8.75	18.00
16.54	36.00	14.79	4.76	7.39	3.11	0.00
20.38	37.00	14.91	5.66	8.76	2.64	0.00
25.38	40.00	12.68	5.94	7.68	2.13	28.00
30.07	42.00	11.10	6.43	4.39	1.72	0.00
33.92	42.00	9.44	6.12	3.60	1.54	0.00

(a)

$\frac{x}{e}$	δ	δ^*	θ	δ_ω	$H = \frac{\delta^*}{\theta}$	$Y_{(\frac{\partial u}{\partial y})_{\max}}$
12.69	27.00	15.10	3.66	11.30	4.13	17.00
16.54	33.00	12.67	5.05	4.48	2.51	0.00
20.38	37.00	14.56	6.07	6.41	2.40	0.00
25.38	45.00	14.71	6.65	6.85	2.21	0.00
30.07	48.00	13.16	7.25	3.50	1.81	0.00
33.92	46.00	10.81	6.79	2.94	1.60	0.00

(b)

$\frac{x}{e}$	δ	δ^*	θ	δ_ω	$H = \frac{\delta^*}{\theta}$	$Y_{(\frac{\partial u}{\partial y})_{\max}}$
12.69	33.00	16.23	4.56	11.54	3.56	16.00
16.54	36.00	15.15	5.76	5.16	2.63	0.00
20.38	42.00	15.56	6.73	4.92	2.30	0.00
25.38	47.00	14.38	6.98	5.14	2.06	0.00
30.07	49.00	11.36	6.91	2.78	1.65	0.00
33.92	55.00	12.44	8.46	2.61	1.47	0.00

(c)

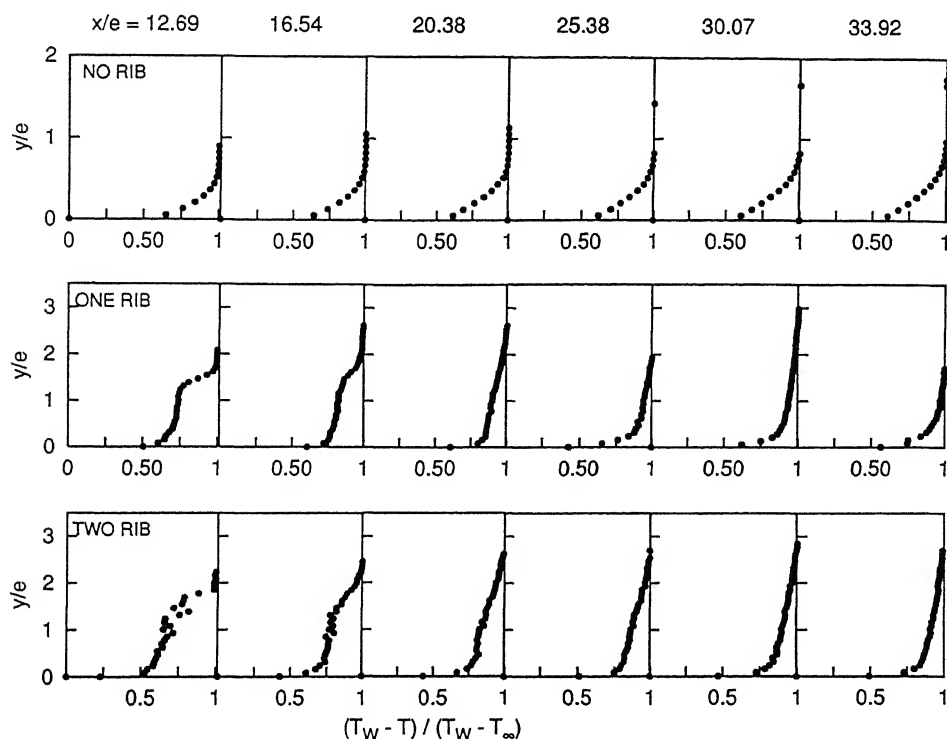


Figure 4.30: Comparison of mean temperature variation for all three cases at $Re=12800$

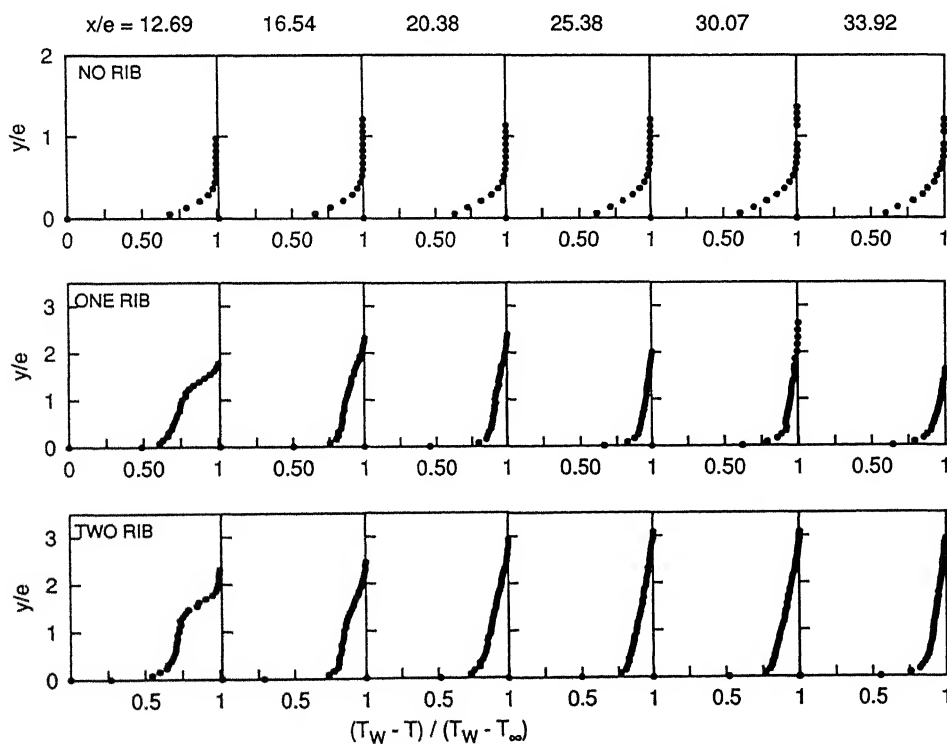


Figure 4.31: Comparison of mean temperature variation for all three cases at $Re=12800$

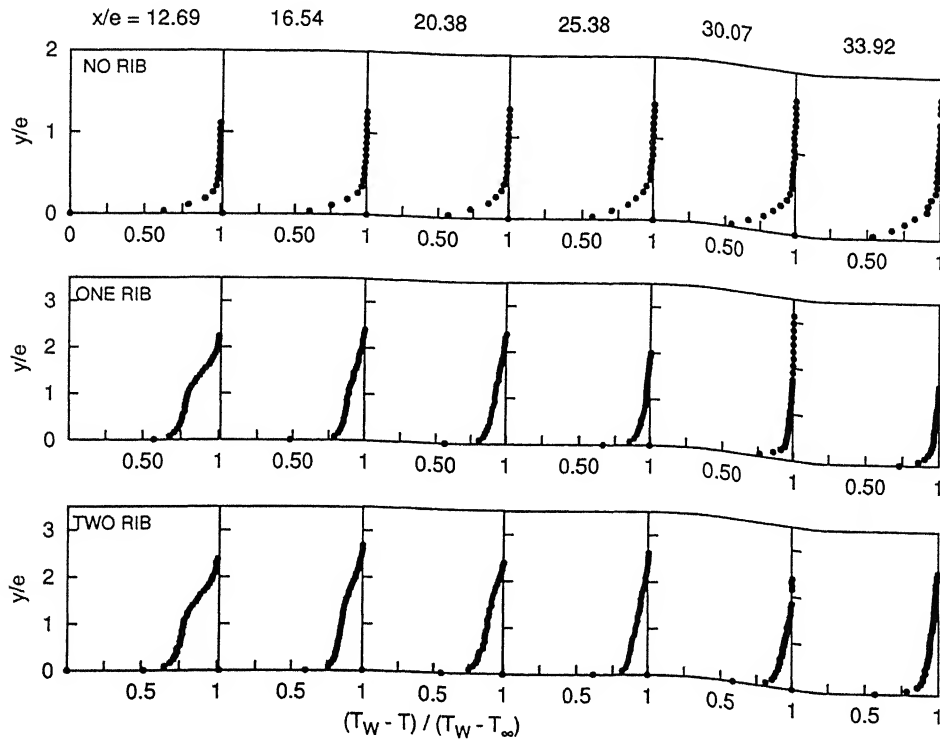


Figure 4.32: Comparison of mean temperature variation for all three cases at $Re=29400$

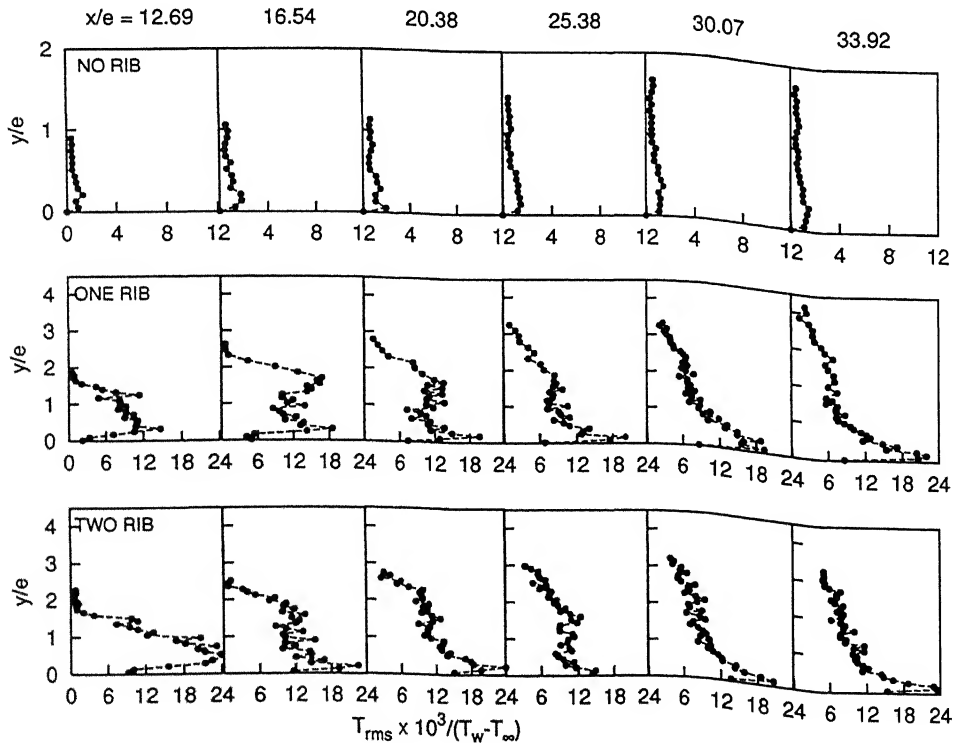


Figure 4.33: Comparison of RMS temperature variation for all three cases at $Re=12800$

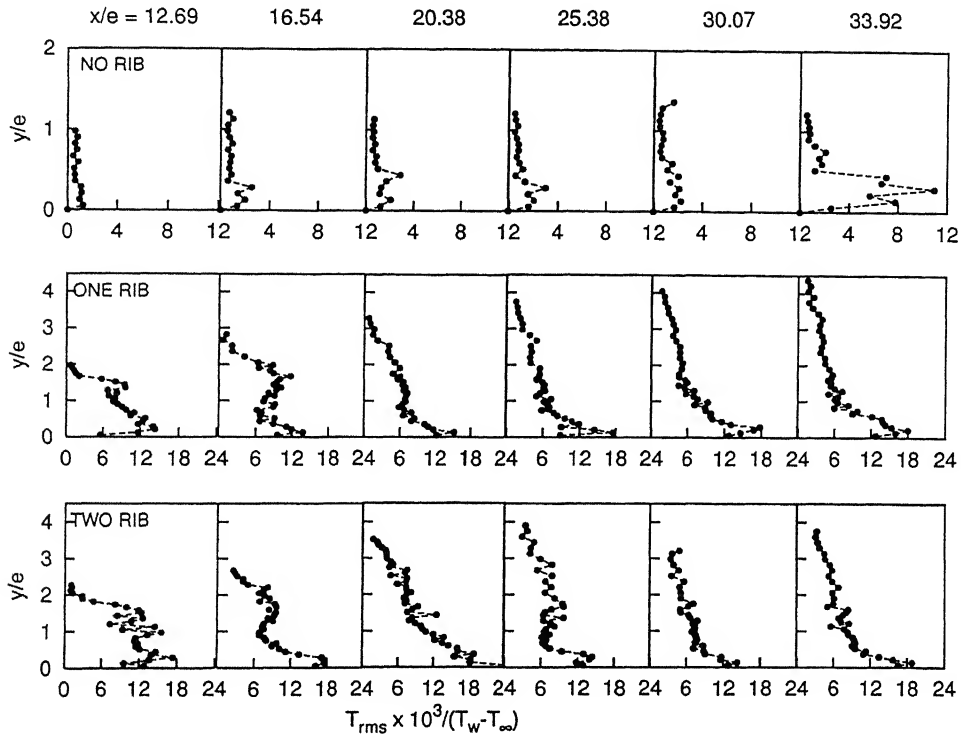


Figure 4.34: Comparison of RMS temperature variation for all three cases at $Re=20900$

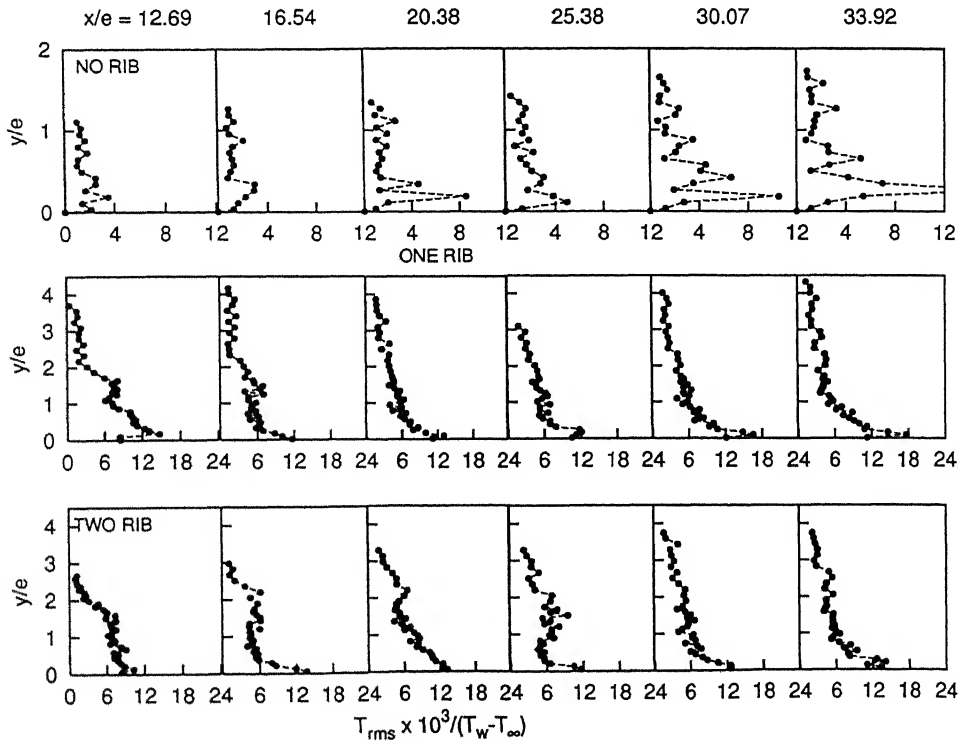


Figure 4.35: Comparison of RMS temperature variation for all three cases at $Re=29400$

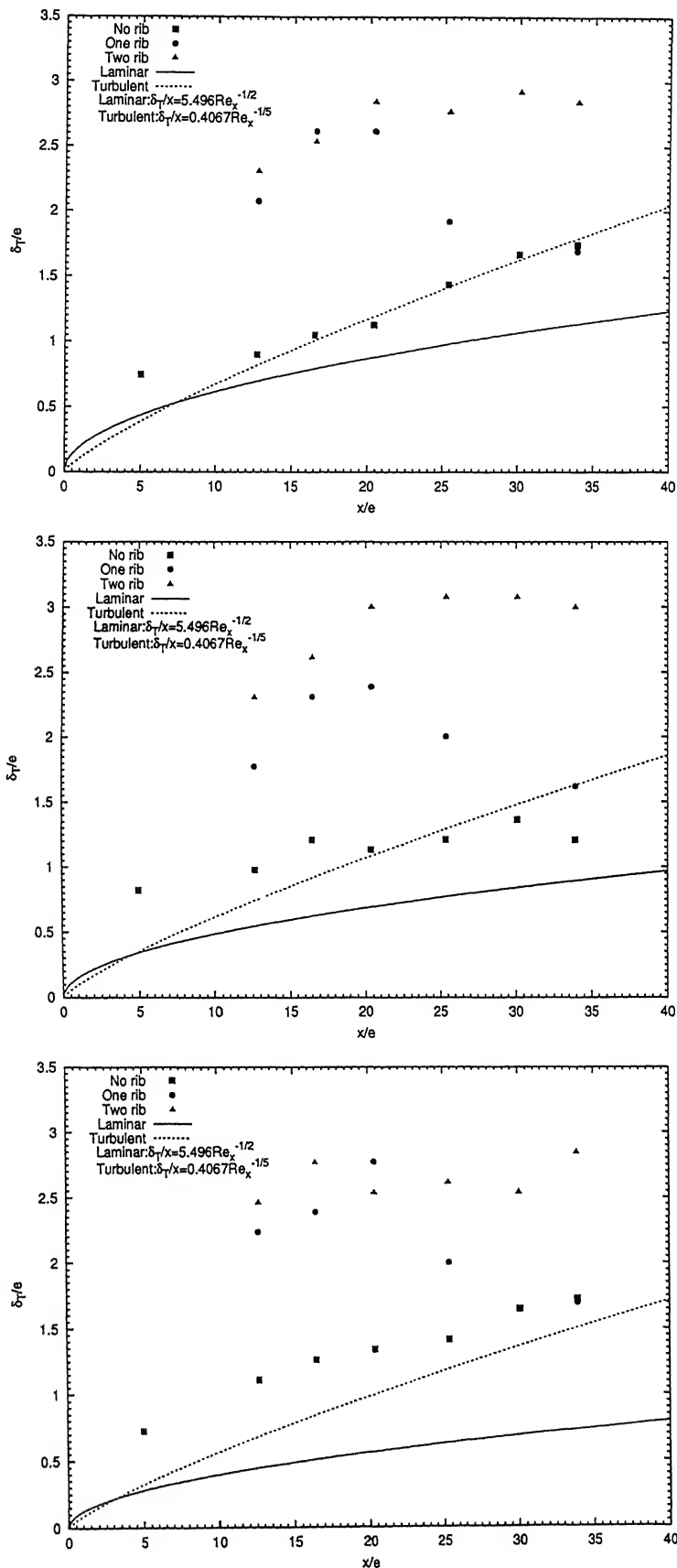


Figure 4.36: Variation of thermal boundary layer thickness with x/e for all three cases at (TOP) $Re=12800$, (MIDDLE) $Re=20900$, (BOTTOM) $Re=29400$

4.4.4 Surface Temperature Visualization

The sequential color images of the bottom surface were grabbed at three Reynolds numbers. The surface was heated to a constant temperature and capturing of sequential images was started at the time when heating current is turned off and the surface is suddenly cooled by flowing the ambient mainstream over it. The temperatures can be determined from the liquid crystal images using a hue calibration curve. The surface temperature at $Re=20900$ in the upstream and downstream of the ribs, compared for one-rib and two-rib cases are shown in Figures 4.37. The temperature of each region is related to the different colors of the picture. In the colored images black indicates the coldest regions i.e temperature below 35° , followed by the colors red, green, yellow and blue, indicating the higher temperatures up to 40° .

Initially the plate is heated up to 40°C and correspondingly the LC sheets appears to be pure blue, then on forced cooling the gradual changes in temperature with time occurs which is clearly depicted in the images. Initially Figure 4.37 shows the constant plate temperature at the start of the experiment by uniform color distribution. Further images show the color/temperature distribution at later time with regular time interval of 90 seconds. At each time step, the changes of temperature for both one-rib and two-rib cases show the difference of cooling. The region in between the two ribs are almost identical for both cases. But, the existence of low temperature at a distance from the downstream edge of the rib indicates that the heat transfer is maximum near the re-attachment region. Comparatively high temperature near the first rib points to the low heat transfer zone due to the stagnant flow in the re-circulation zone. This stagnant region is not seen after the second rib. Overall, the visualization image shows that the flow is not two-dimensional as was expected from the 2-D nature of the rib-channel geometry. The existence of definite three dimensionality in the downstream region of the flow behind rib is supported by the non uniform color distribution in the span wise direction. Further after 270 seconds of cooling, some parts the plate has cooled to a temperature which is below the 35°C since redness has appeared in certain regions of the images and the thermal field is well inside the range of liquid crystal.

The color images of the transient test experiment conducted at $Re=12800$

and 29400 in the upstream and downstream of the ribs for a time interval of 30 seconds are shown in Figure 4.38 on gray scale. Figure 4.38 shows the Reynolds number effect on the ribbed surface. As the velocity increases the heat transfer rate increases and fast cooling occurs. This can be easily visualized by the images of Figure 4.38. After 180 seconds the temperature of the ribbed plate at $Re = 12800$ is within the bandwidth of the LC sheets indicating the lower average heat transfer coefficient. In case of $Re = 29400$, part of the test surface appears to be completely black indicating fast cooling and higher average heat transfer coefficient.

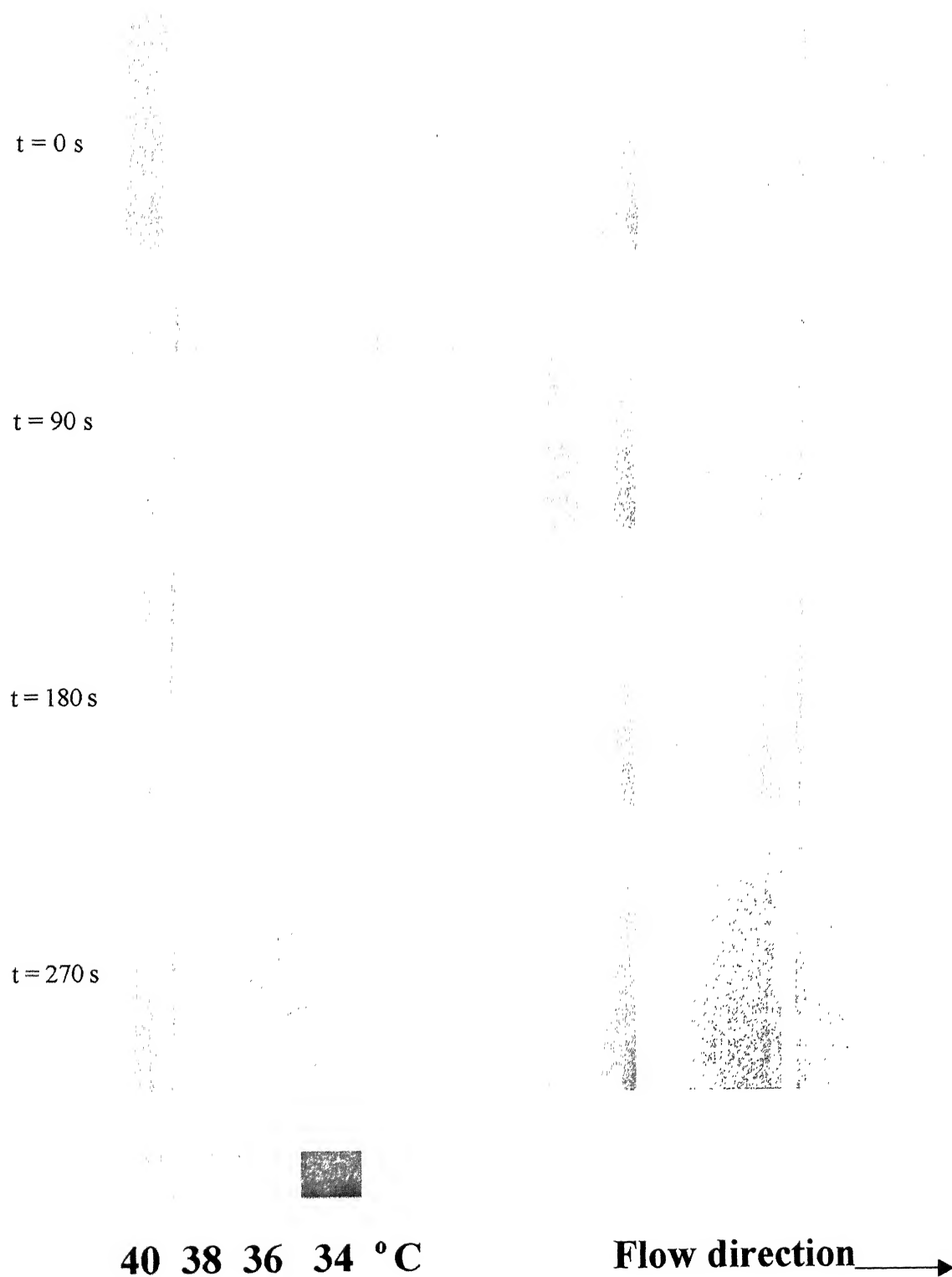


Figure 4.37: Transient liquid crystal images showing temperature changes during the cooling of the bottom surface with one-rib and two-rib cases at $Re = 20000$

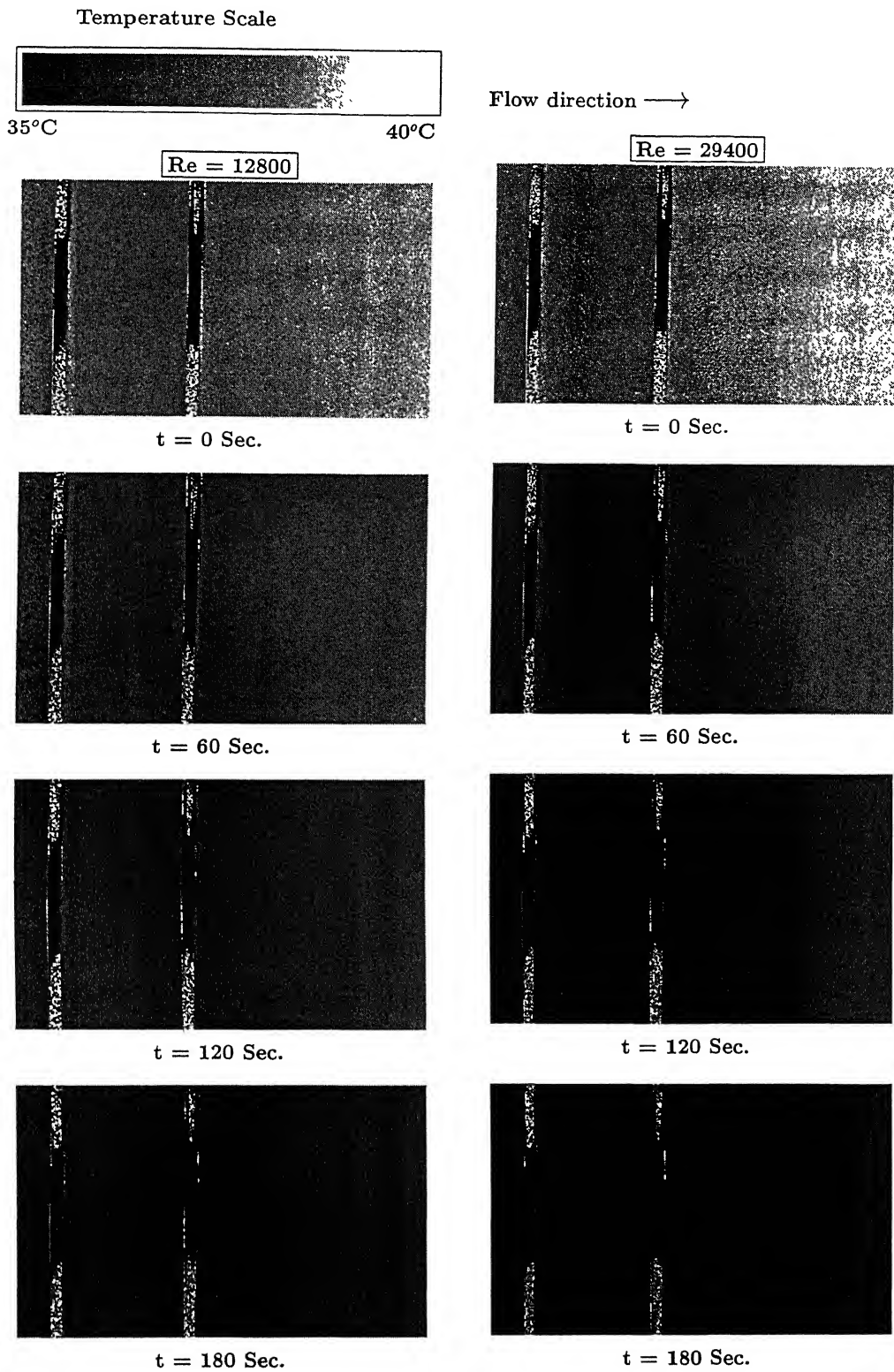


Figure 4.38: Transient liquid crystal images showing temperature changes during the cooling of the bottom surface with two ribs from 40°C at Re=12800 (Left) and Re=29400 (Right).

4.4.5 Nusselt Number

The transient temperature distribution is used for evaluation of the local heat transfer coefficient using LCT. The LCT analysis is verified by comparing it with the heat transfer coefficient obtained using law of the wall. These plots are shown in Figures 4.39, 4.40 and 4.41 at three different Reynolds number. The nature of variation is observed to be similar with the magnitude obtained from the law of the wall, but the difference between the two is increasing with increase in the Reynolds number. Overall, these plots enforces the validity of the law of the wall and LCT analysis for turbulent flow. In Figures 4.42, 4.43 and 4.44, the span-wise averaged Nusselt number variation in stream-wise direction obtained from LCT for the no-rib, one-rib, and two-rib cases are compared. The Nusselt number for the no-rib case is less than that of one-rib and two-rib case at all stream-wise locations except close to the first rib. At close to the rib, the Nusselt number is lower than the no-rib case due to the presence of the re-circulating stagnation region and hence negligible convection near the rib. The local Nusselt number obtained from LCT for the no-rib case well downstream of the ribs is less than that of two-rib case and one-rib case. From this observation, it may be concluded that the redeveloping turbulent boundary layer well past the rib turbulator is not similar in nature to that of the plane turbulent boundary layer. The turbulent fluctuation inside the boundary layer for the one-rib and two-rib case is more than that of the boundary layer for the smooth wall case, which is responsible for higher Nusselt number in the post reattachment region.

Table 4.5: The augmentation of Nusselt number for one-rib case and two-rib case from LCT analysis and energy balance.

$N_{\overline{Nu},a}$	Configuration	Energy balance	Transient LCT
Re=12800	One-rib	1.394	2.13
	Two-rib	1.519	2.24
Re=20900	One-rib	1.664	2.18
	Two-rib	1.869	2.40
Re=29400	One-rib	1.605	2.05
	Two-rib	1.868	2.14

The Nusselt number augmentation for one-rib and two-rib cases are shown in Table 4.5. The reason for this difference is the area for which the average Nusselt number is determined. In case of energy balance, the whole area of the plate is taken in to consideration while for LCT, the average Nusselt number is calculated for only the area covered by image which is smaller and contains only the higher heat transfer zones. Overall. the trend is similar except for the lowest Reynolds number.

4.4.6 Surface Nusselt Number Distribution

Before discussing the Nusselt number distribution, the validity of the values obtained from the transient LC analysis should be checked. Figures 4.39, 4.40 and 4.41, show the values of Nusselt number obtained from LCT analysis compared with the values obtained from the law of the wall. It can be observed that for all three Reynolds, the nature of variation of Nusselt number with x/e is similar from both LCT and the law of the wall. But the absolute values are quite close for lowest Reynolds number and with increase of Reynolds number, it is moving to lower side. This observation is in accordance with the earlier discussion made in chapter 3. So finally it can be concluded that for lower Reynolds number, the discussions would be correct, both quantitatively and qualitatively and for higher Reynolds number it would be at least correct qualitatively.

Figures 4.45, 4.47 and 4.47 show the surface Nusselt number distribution for no-rib, one-rib and two-rib cases for three different Reynolds number. For the no-rib case, variation of Nusselt number is very smooth, as it is high at starting locations and then decreasing when moving further downstream locations. After a certain distance, not much variation is seen in Nusselt number, indicating that flow is tending to reach the thermally fully developed condition.

Figures 4.45, 4.47 and 4.47 show the surface Nusselt number distribution for no-rib, one-rib and two-rib cases for three different Reynolds number. For the no-rib case, variation of Nusselt number is very smooth, as it is high at starting locations and then decreasing when moving o further downstream locations. After a certain distance, not much variation is seen in Nusselt number, indicating that flow is tending to reach the thermally fully developed condition.

Figures 4.45, 4.47 and 4.47 show the surface Nusselt number distribution for no-rib, one-rib and two-rib cases for three different Reynolds number. For the no-rib case, variation of Nusselt number is very smooth, as it is high at starting locations and then decreasing when moving o further downstream locations. After a certain distance, not much variation is seen in Nusselt number, indicating that flow is tending to reach the thermally fully developed condition.

Now, looking at the distribution of Nusselt number, there is a region of low heat transfer coefficient just after the rib, indicating the presence of re-circulating region. Value of Nusselt number in this region is comparable to that in the upstream of the rib. This observation is very important because there is no zone where the heat transfer is lower than that for the flat plate case, defying any speculation about the hot-spots even after the rib. After the re-circulating region, there exists a region of very high Nusselt number. This is showing that the separated shear layers are re-attaching to the surface, and vortices generated because of the rib, increasing the heat transfer. When comparing the one-rib case for different Reynolds number, it is seen that this reattachment region is moving nearer to the rib i.e. stagnant zone is becoming smaller. The reason for this could be the delay of separation as point of separation may not be the leading tip of the rib as Reynolds number is increasing. It can also be seen that the area covered by the reattachment region is extending well beyond the position of second rib and this area is increasing with increase in the Reynolds number. After this region, Nusselt number is again decreasing because the viscous sublayer is starting to develop after reattachment.

For the two-rib case, the region between the first and second rib is almost similar to that for the one-rib case. But after the second rib, Nusselt number is high even just after the rib showing that the effect of the first rib is prevailing there and no stagnant region is formed. The effect of second rib seen after that but the effect is not as prominent as that for the first rib in one- rib case. Also the effect of second rib is seen at a shorter distance from the rib as compared to the distance after the first rib. The presence of ribs is also inducing the three dimensionality to the flow field, as it is obvious from the Nusselt number distribution in the cross-wise direction. This is reaffirming the similar observation made in surface temperature visualization.

To show the effect of Reynolds number, the Nusselt number distribution at all three Reynolds numbers for one-rib case is shown in Figure 4.48. A significant increase in the Nusselt number can be seen for the $Re = 20900$ and 29400 in comparison to $Re = 12800$. The size of the reattachment region is observed to increase with a subsequent decrease in the in the stagnant region. The reduction in the size of the stagnant region may be because of the delay in the separation as the Reynolds number is increased. The three dimensionality also increases with the increase in the Reynolds number which is expected because of the increased turbulence in the flow field.

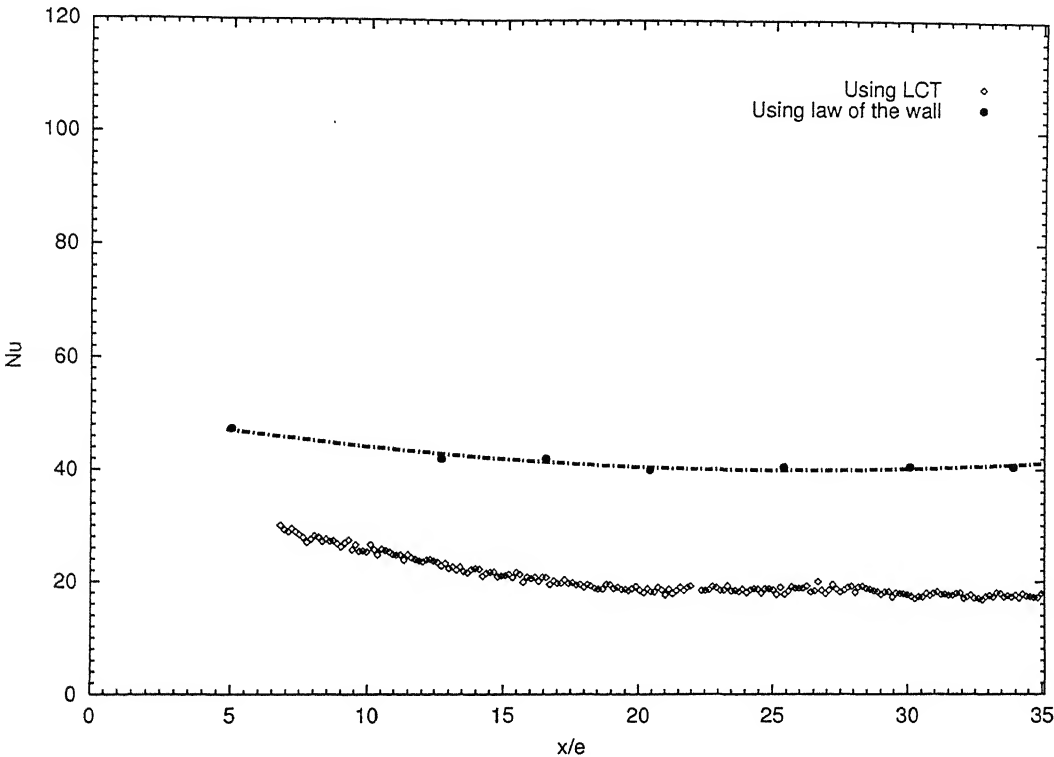


Figure 4.39: Span-wise averaged local Nusselt number comparison of the no-rib case using LCT with that from the law of the wall at $Re=12800$

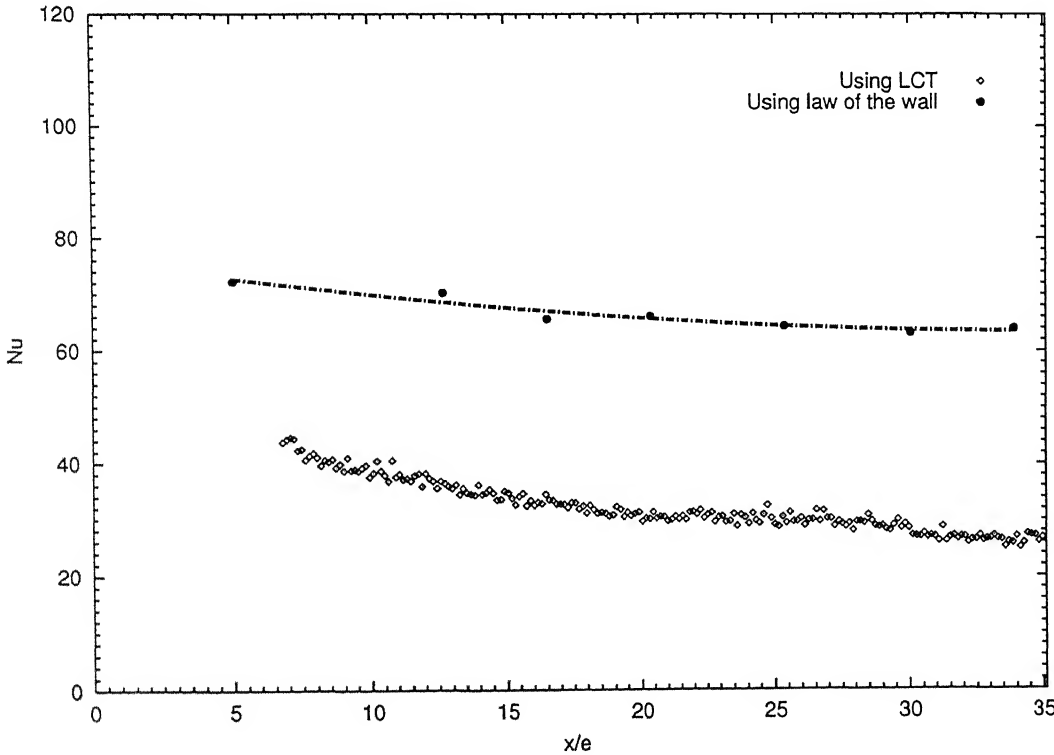


Figure 4.40: Span-wise averaged local Nusselt number comparison of the no-rib case using LCT with that from the law of the wall at $Re=20000$

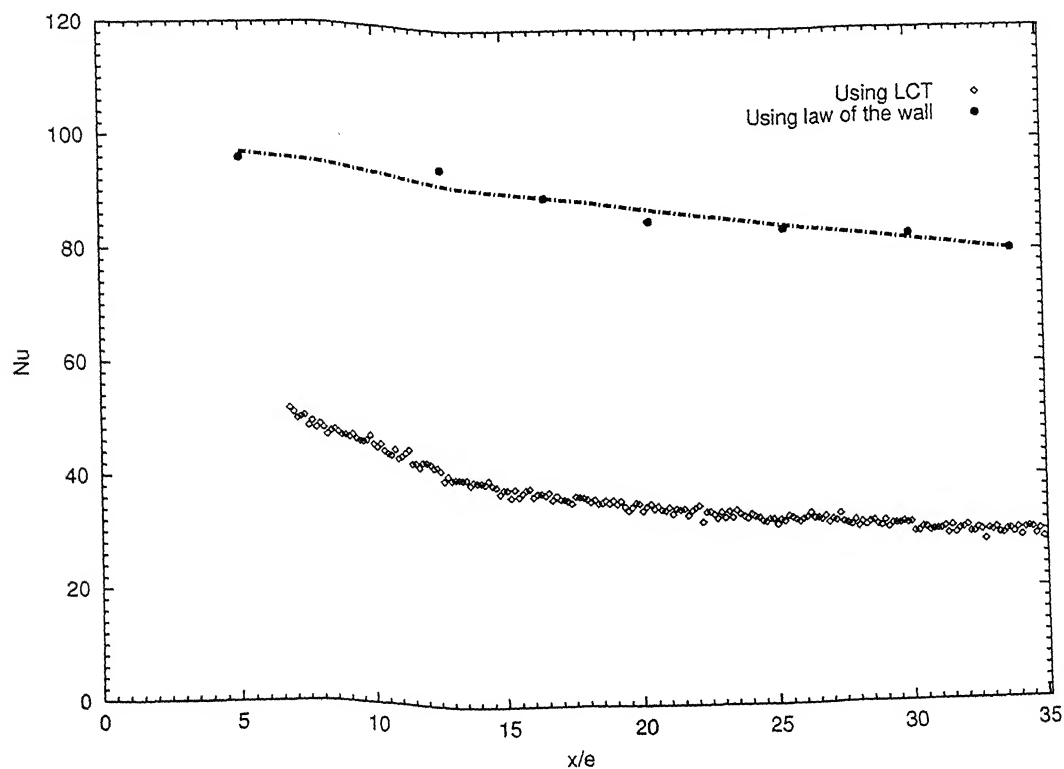


Figure 4.41: Span-wise averaged local Nusselt number comparison of the no-rib case using LCT with that from the law of the wall at $Re=29400$

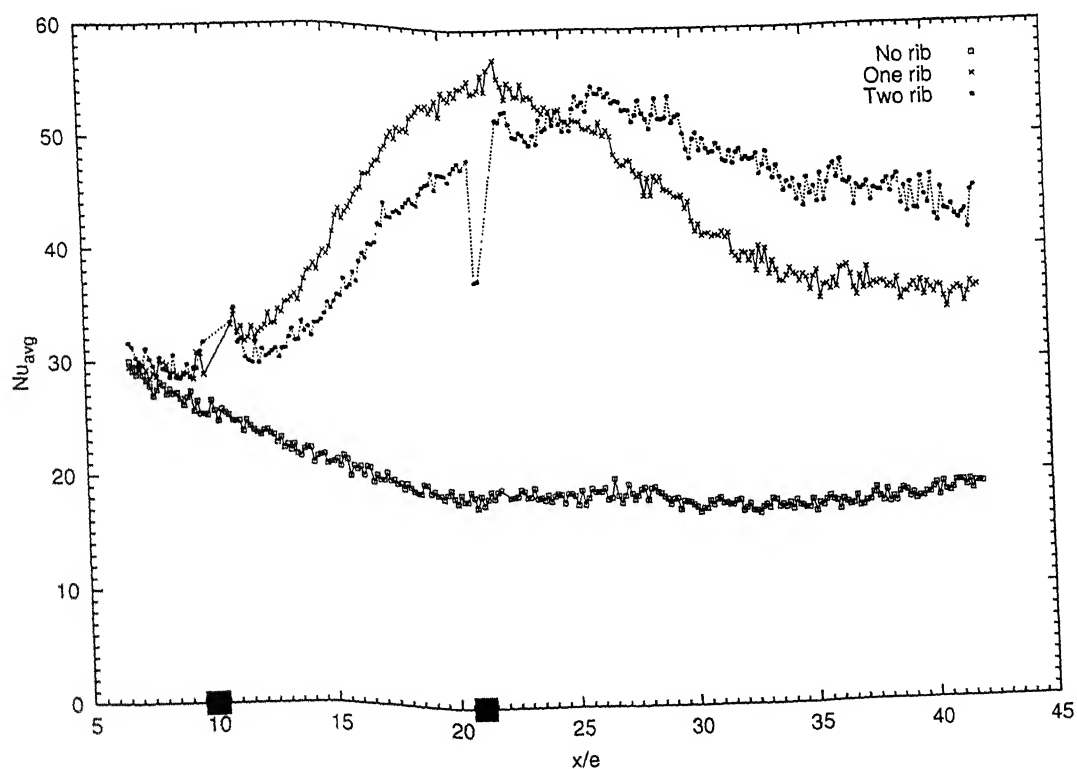


Figure 4.42: Comparison of span-wise averaged local Nusselt number variation for all three cases using LCT at $Re=12800$

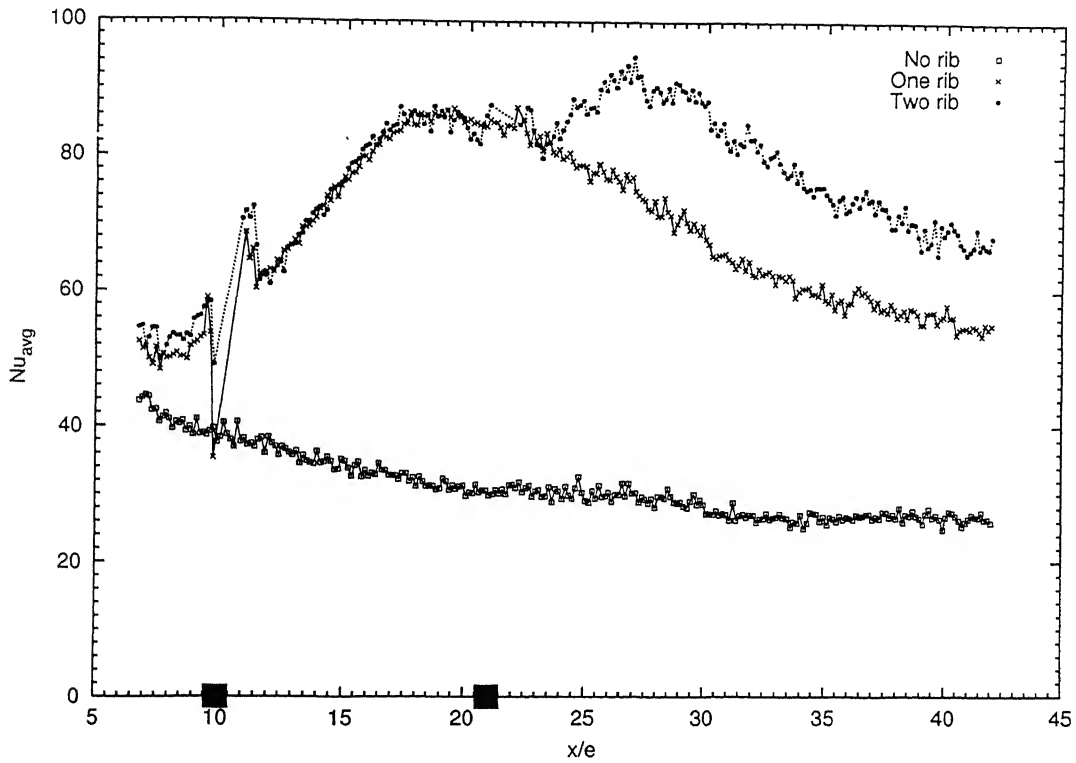


Figure 4.43: Comparison of span-wise averaged local Nusselt number variation for all three cases using LCT at $Re=20900$

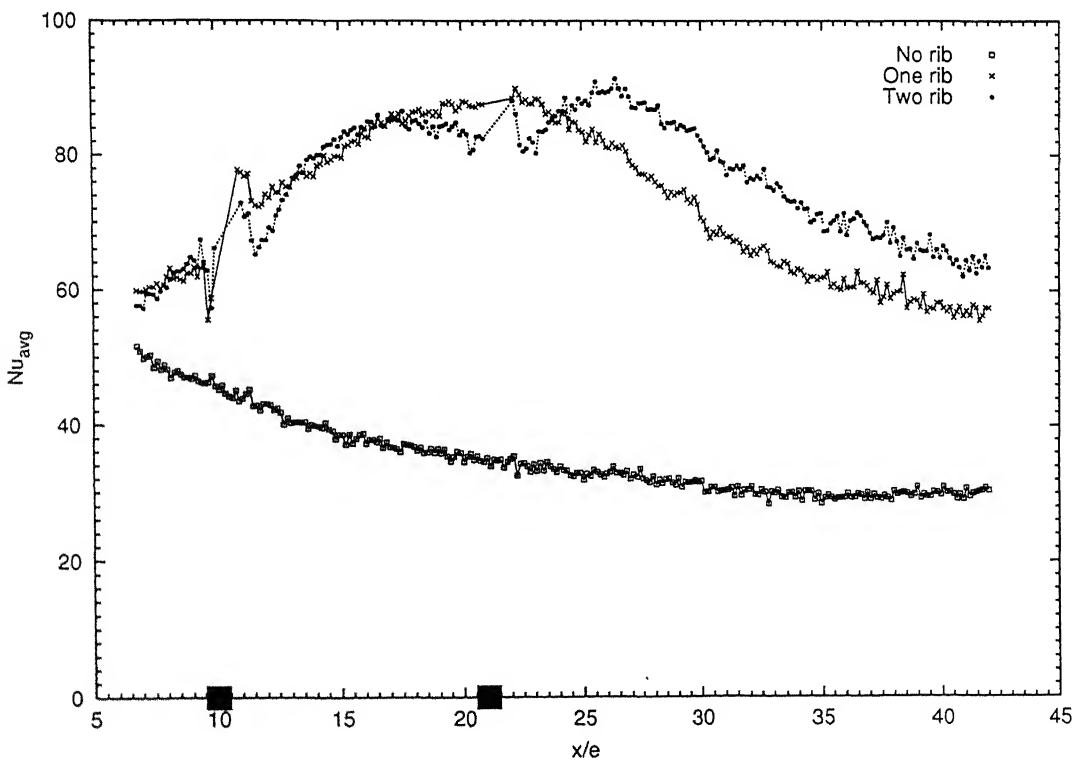


Figure 4.44: Comparison of span-wise averaged local Nusselt number variation for all three cases at $Re=29400$

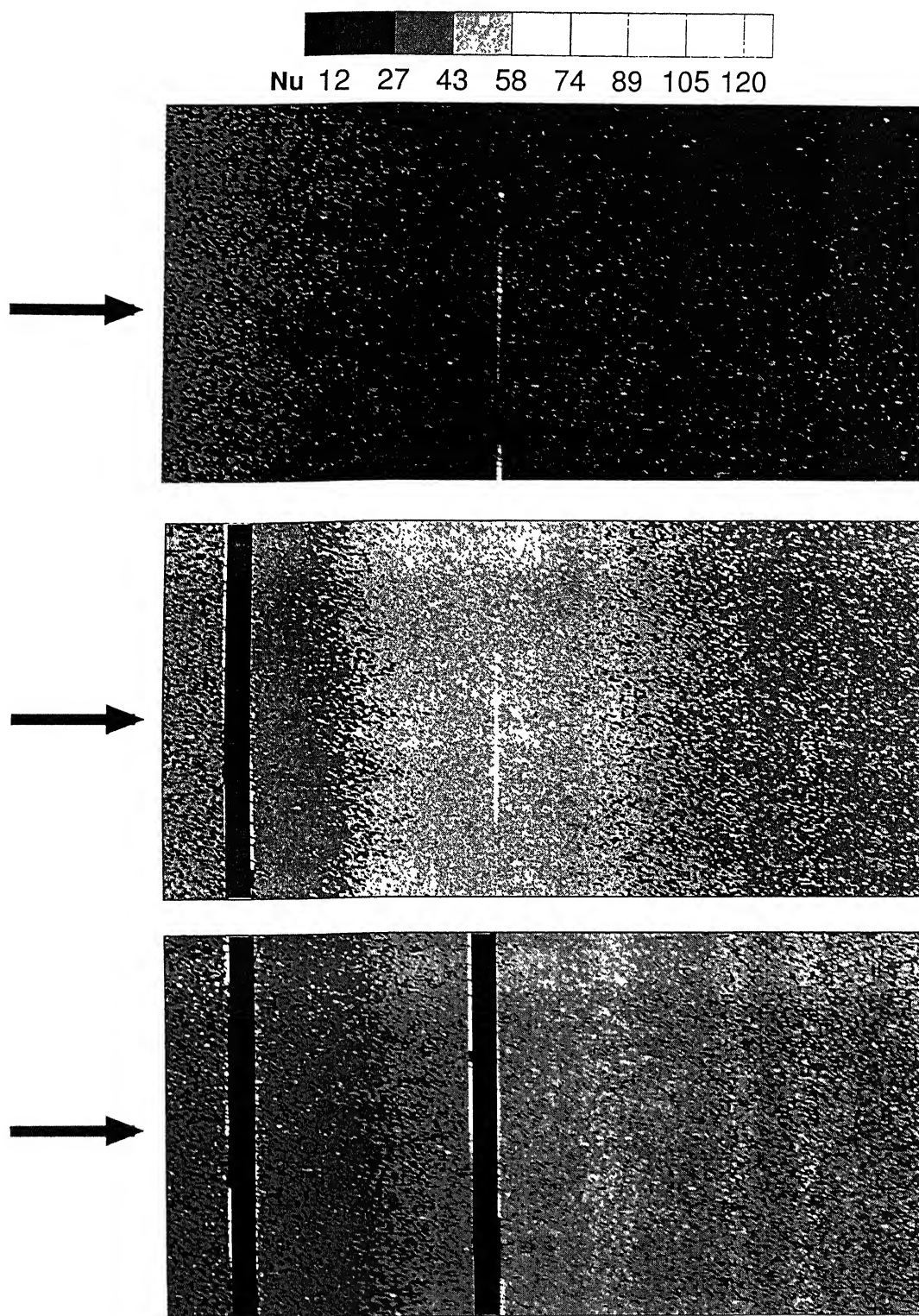


Figure 4.45: Detailed Nusselt number distribution for no-rib, one-rib and two-rib cases at $Re = 12800$

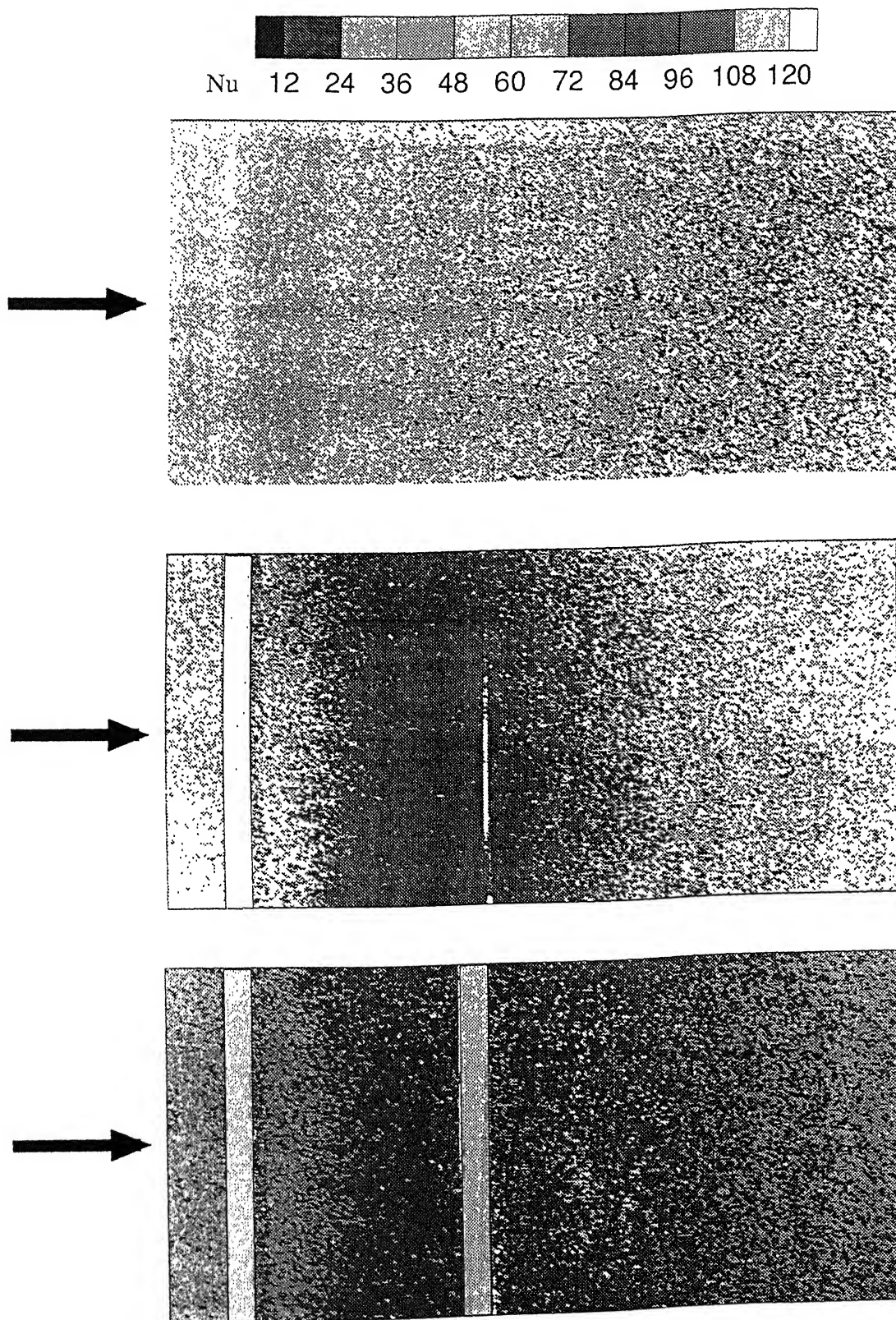


Figure 4.46: Detailed Nusselt number distribution for no-rib, one-rib and two-rib cases at $Re = 20900$

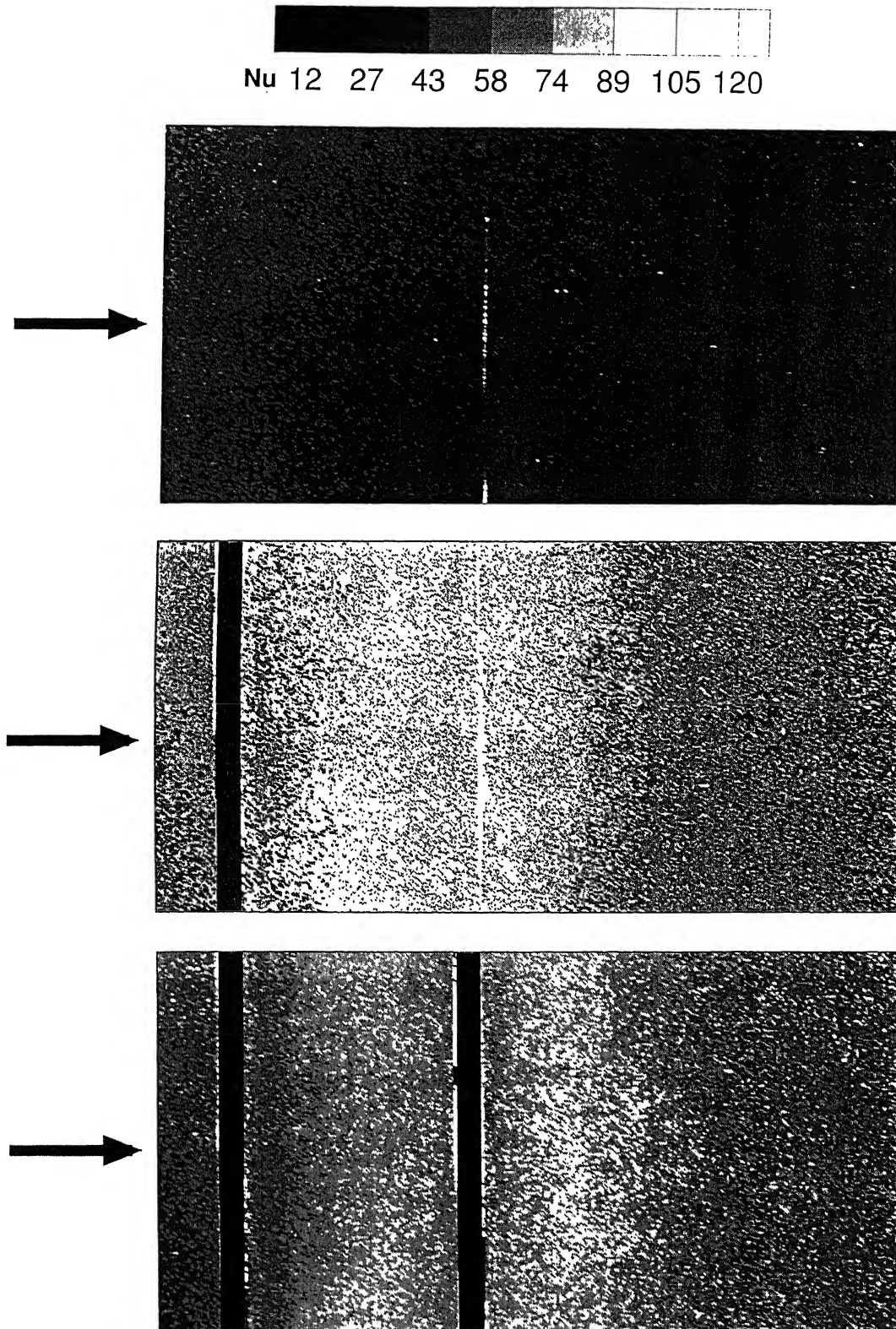


Figure 4.47: Detailed Nusselt number distribution for no-rib, one-rib and two-rib cases at $Re = 29400$

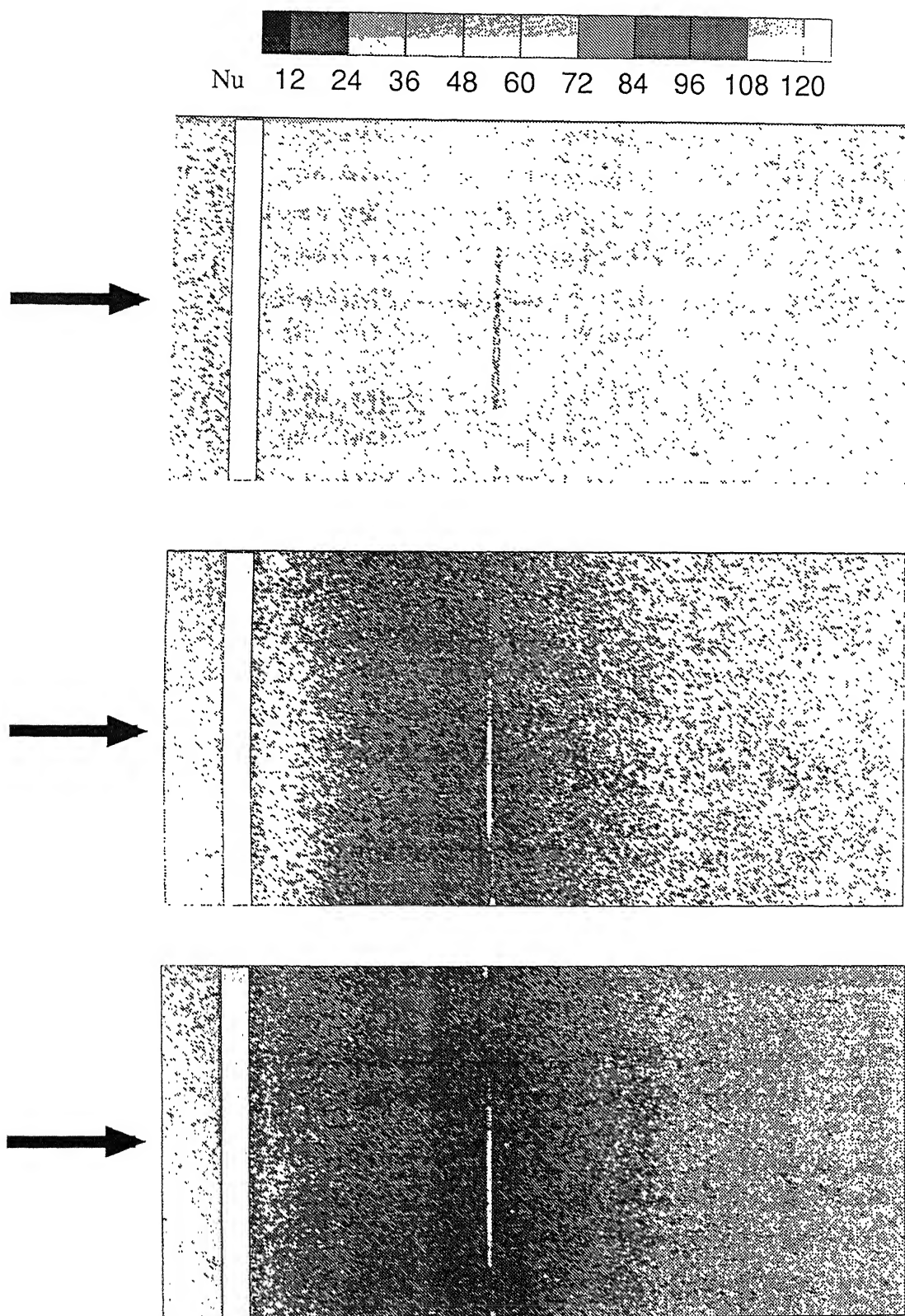


Figure 4.48: Detailed Nusselt number distribution for $Re = 12800$ (TOP), $Re = 20900$ (MIDDLE) and $Re = 29400$ (BOTTOM).

4.4.7 Transition of Boundary Layer

From the shape factor calculation discussed in the earlier section, continuous drop or change in shape factor was observed in the downstream direction. The shape factor magnitude in the far field region for the no-rib, one-rib and two-rib cases were different from each other. To varify if the boundary layer developing behind the rib is approaching the the turbulent flat plate profile according to the law of the wall, the velocity and temperature profile in u^+ vs y^+ and t^+ vs y^+ coordinate are shown in the Figure 4.49 to 4.54.

In the Figure 4.49, it may be observed that the velocity profile at all x/e location are very close to that of the law of the wall in the downstream direction. The rate of change in shape of u^+ vs y^+ profile decreases in the streamwise direction. No significant change is observed between $x/e = 25.38$ and 33.92 location. Same observation is made from the shape factor calculation where no significant change in shape factor value was observed between $x/e = 25.38$ and 33.92 . In contrast, for the two-rib case, change in nature of the u^+ vs y^+ profile is observed between $x/e = 30.07$ and 33.92 indicating that the development of the boundary layer is incomplete. The above observation is also corroborated by the shape factor result in Table 4.2 , 4.3 and 4.4.

In Figure 4.50, it maybe observed that the viscous-sublayer region and transition region is non existent in comparison to that seen in the u^+ vs y^+ plot of Figure 4.49. Similarly, for the one-rib case in 4.50, the transition of the boundary layer shape from one streamwise location to another is observed to be less than what is observed for the velocity boundary layer in Figure 4.49. Similar trend is also observed for the two-rib case in 4.50. The early transition in the thermal boundary layer in comparison to the velocity boundary layer may be attributed to the fact that the Prandtl number for the air is less than one.

Figures 4.51 to 4.54 shows the u^+ vs y^+ and t^+ vs y^+ plot at higher Reynolds number equal to $Re=20900$ and 29400 . comparing Figure 4.51 with Figure 4.49, at $x/e=12.69$ the profile is observed to develop more rapidly at higher Reynolds number for both one-rib and two-rib cases. Similarly, comparison of Figure 4.50 with Figure 4.52 shows that, for the two-rib case, transition of the thermal boundary layer to the law of the wall is more rapid at higher Reynolds number.

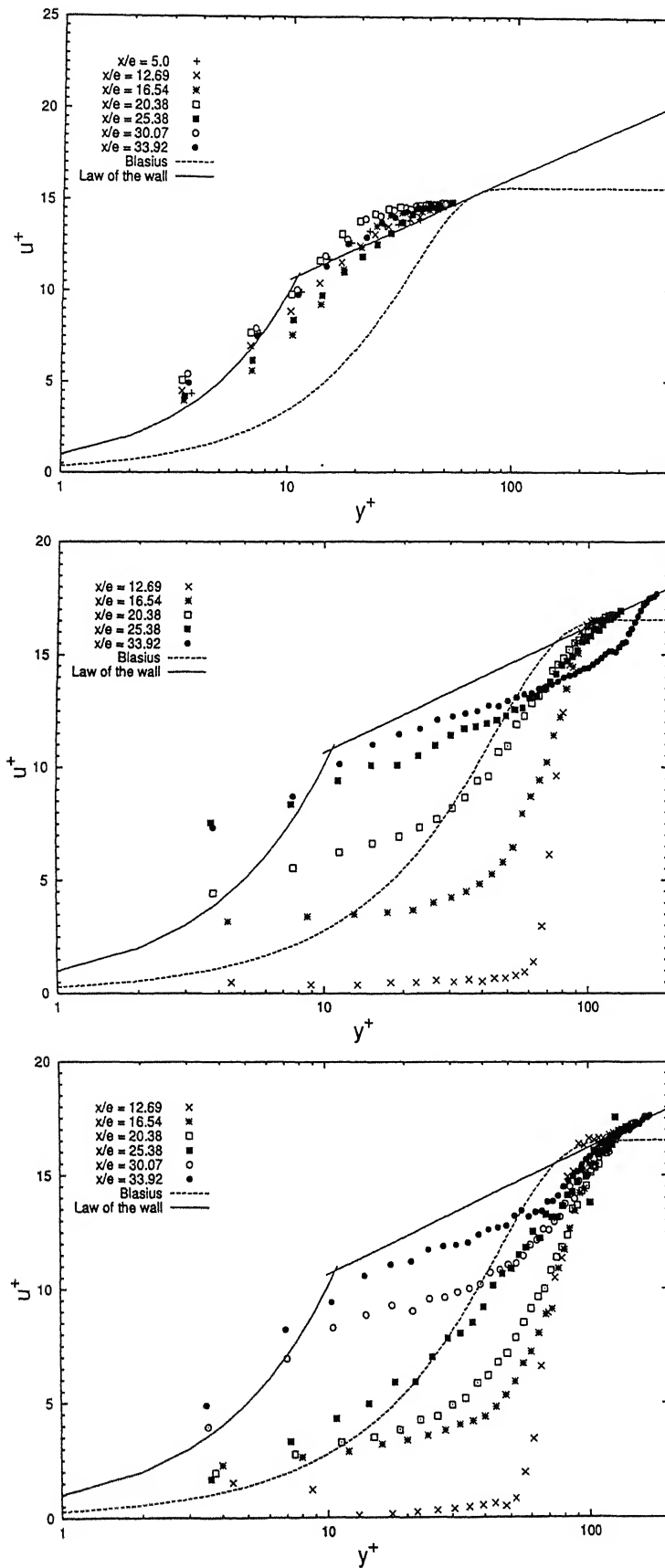


Figure 4.49: Variation of u^+ with y^+ for (TOP) no-rib case, (MIDDLE) one-rib case, (BOTTOM) two-rib case at $Re=12800$

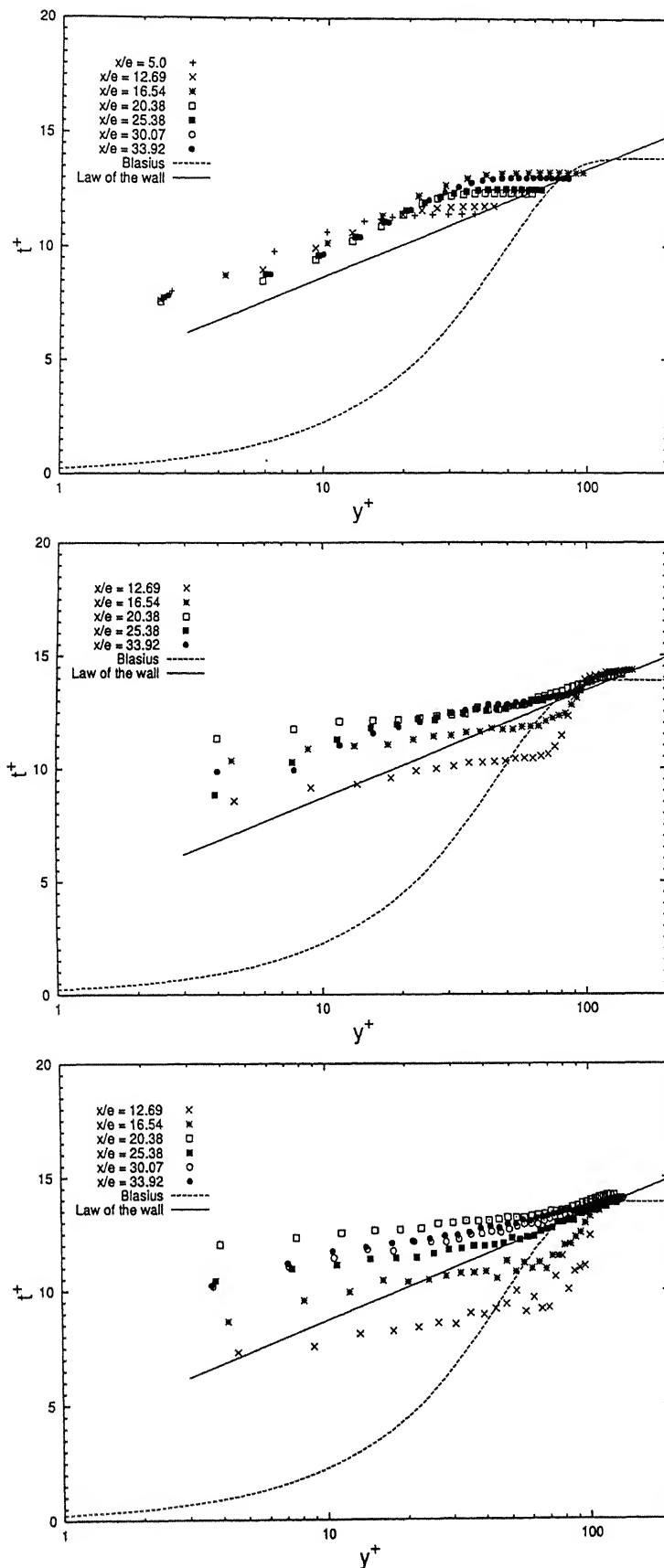


Figure 4.50: Variation of t^+ with y^+ for (TOP) no-rib case, (MIDDLE) one-rib case, (BOTTOM) two-rib case at $Re=12800$

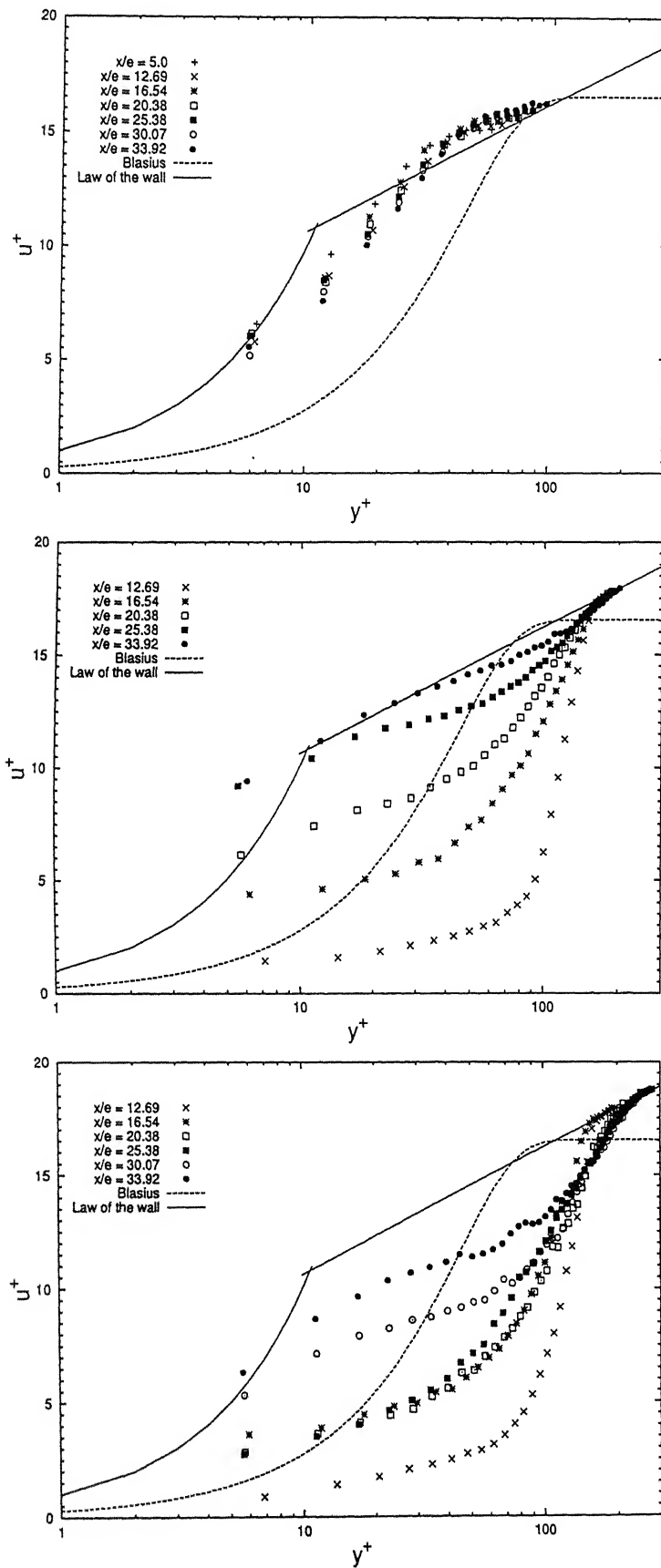


Figure 4.51: Variation of u^+ with y^+ for (TOP) no-rib case, (MIDDLE) one-rib case, (BOTTOM) two-rib case at $Re=20900$

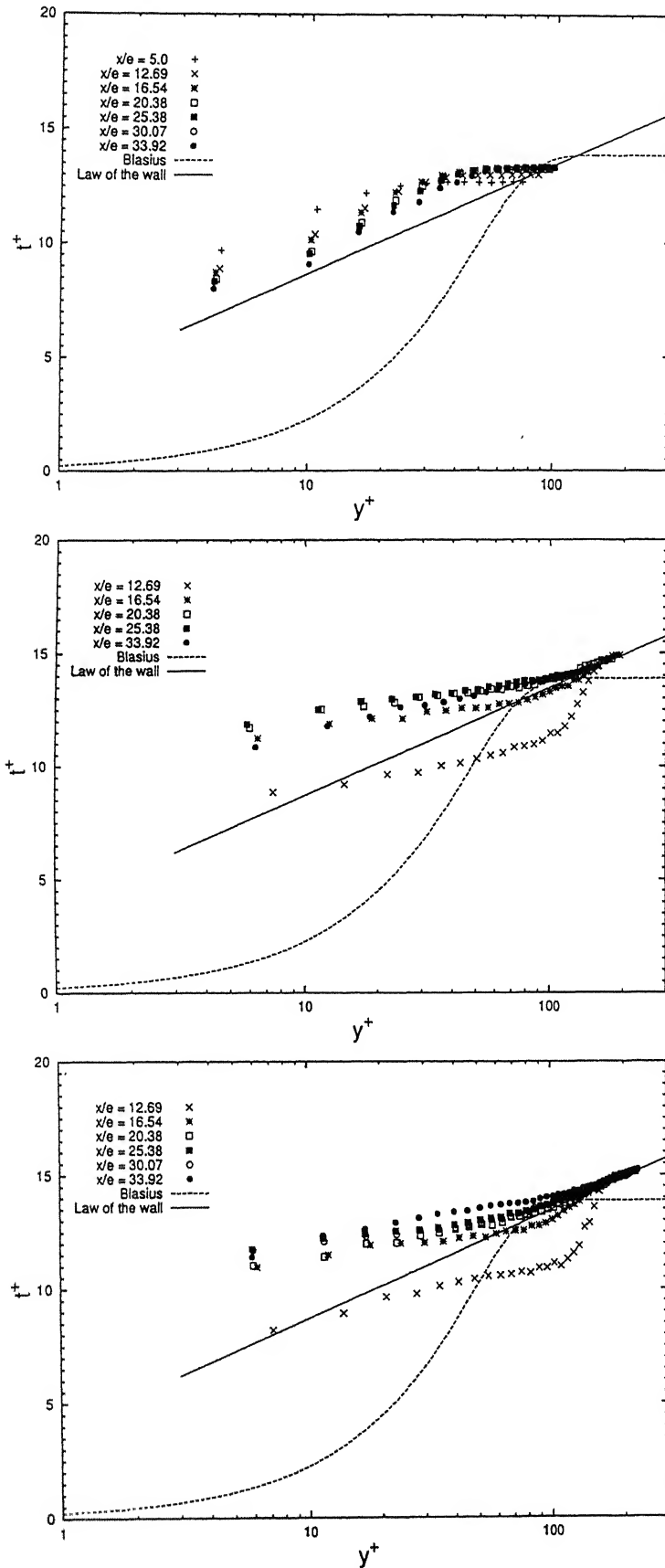


Figure 4.52: Variation of t^+ with y^+ for (TOP) no-rib case, (MIDDLE) one-rib case, (BOTTOM) two-rib case at $Re=20900$

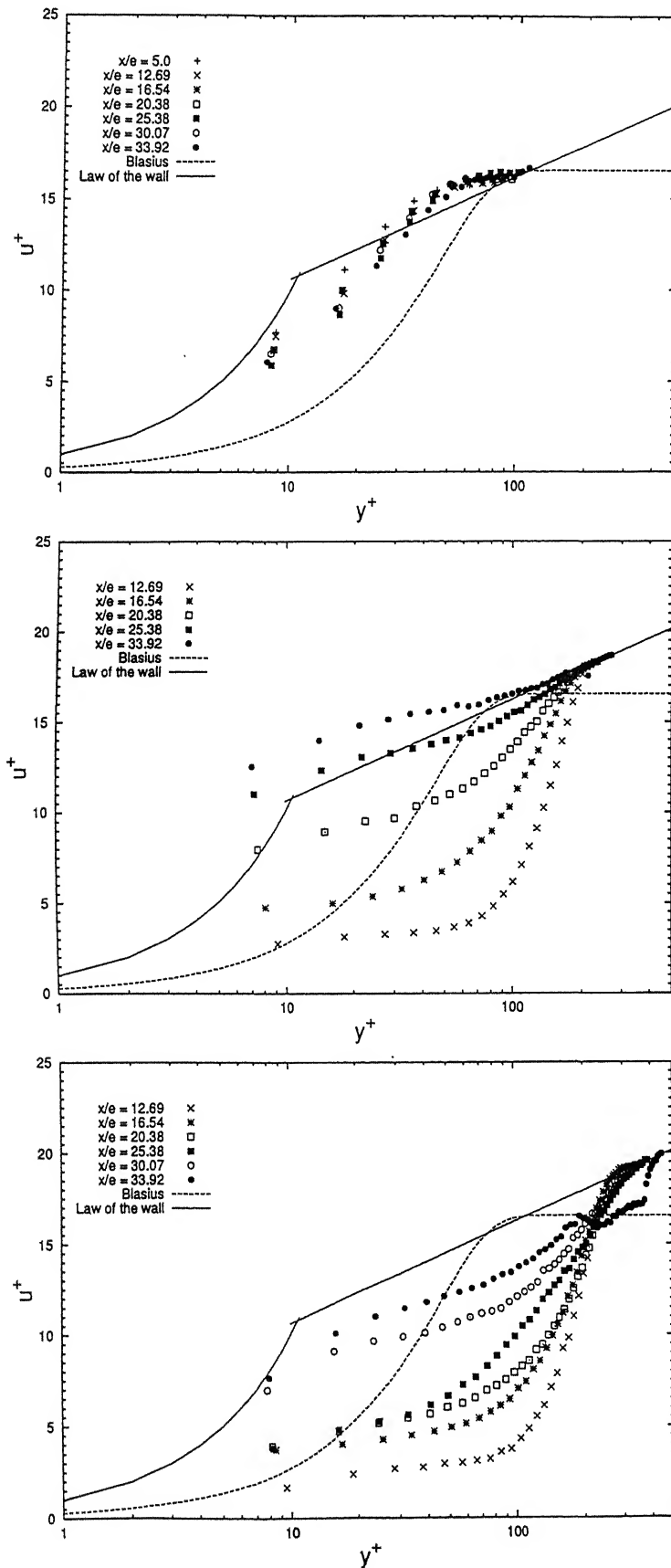


Figure 4.53: Variation of u^+ with y^+ for (TOP) no-rib case, (MIDDLE) one-rib case, (BOTTOM) two-rib case at $Re=29400$

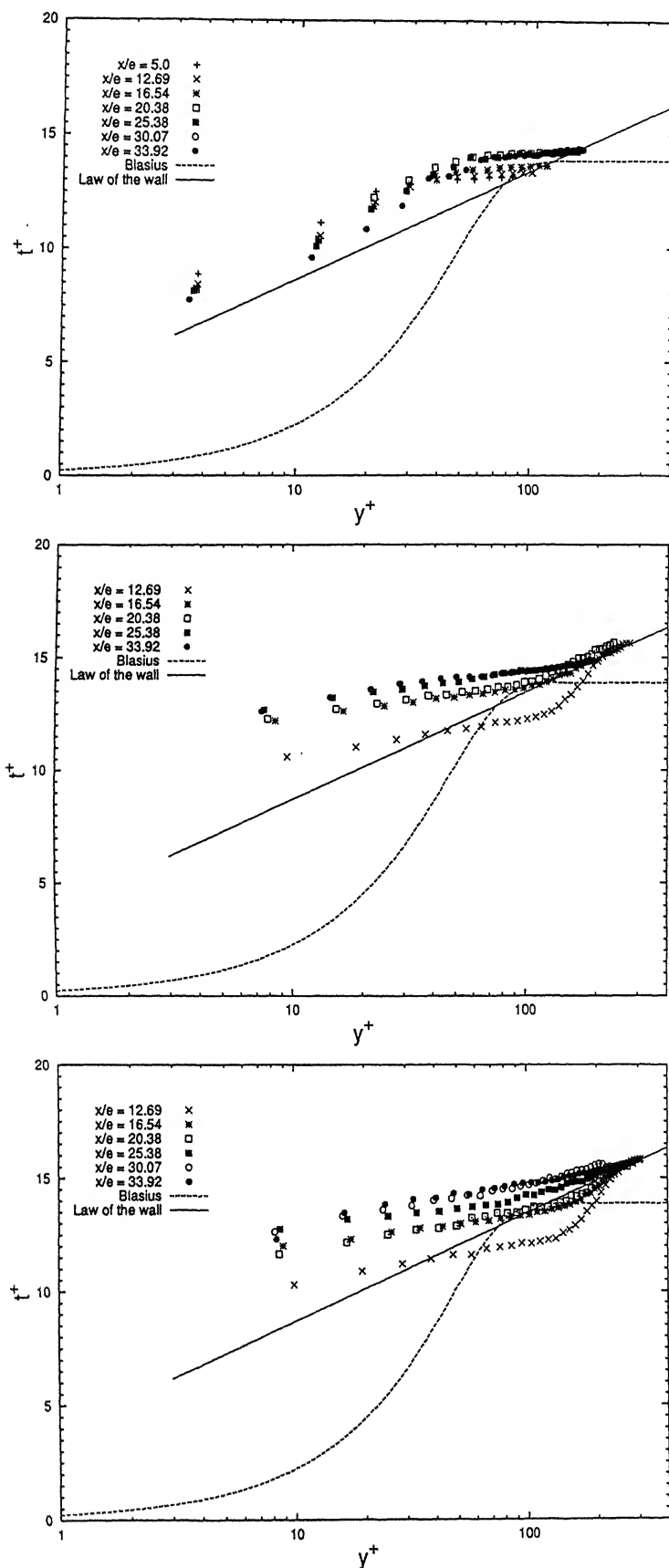


Figure 4.54: Variation of t^+ with y^+ for (TOP) no-rib case, (MIDDLE) one-rib case, (BOTTOM) two-rib case at $Re=29400$

4.5 Performance Evaluation

The irreversibility of convective heat transfer is seen to be due to two effects: heat transfer across a finite (nonzero) temperature difference and fluid friction. The competition between flow and heat transfer irreversibilities occurs in connection with the general problem of heat transfer augmentation.

The task of properly evaluating the merit of a proposed augmentation technique, is perhaps, as important as developing and applying the technique. The trade-off between heat transfer and fluid flow irreversibilities governs the application of any augmentation technique. The true effect of a proposed augmentation technique on thermodynamic performance may be evaluated by comparing the irreversibility of the heat exchange apparatus before and after the implementation of the augmentation technique. Bejan [2] has developed entropy generation minimization EGM method as a solid thermodynamic basis for evaluating the merit of augmentation techniques.

The average results for evaluating thermodynamic performance of one-rib and two-rib case are presented in Table 4.6. The last four columns at the right are respectively from left to right: the augmentation Nusselt friction factor number, $N_{\overline{Nu}\bar{f},a}$ ($= (\overline{Nu}/\bar{f})_a/(\overline{Nu}/\bar{f})_o$), the augmentation Nusselt number, $N_{\overline{Nu},a}$ ($= \overline{Nu}_a/\overline{Nu}_o$), the augmentation entropy generation number Bejan [2], $N_{S,a}$ ($= \dot{S}'_a/\dot{S}'_o$), and the irreversibility distribution ratio Bejan [2], ϕ ($= \dot{S}'_{\Delta P}/\dot{S}'_{\Delta T}$), where \dot{S}' is the entropy generation rate per unit heated length. In these notations the subscript 'a' refers to the augmented passage, the subscript 'o' refers to the original (unaugmented) passage, the subscript ' ΔP ' and ' ΔT ' represents the irreversibilities caused by fluid friction and due to heat transfer respectively.

Augmentation entropy-generation number Bejan [2], $N_{S,a}$ is found to be useful in quantizing the thermodynamic impact of the augmentation technique. Augmentation techniques that are characterized by $N_{S,a}$ values less than one are thermodynamically advantageous. Augmentation entropy-generation number is determined by computing \dot{S}' for both the augmented and unaugmented passage (baseline case) using entropy generation rate formula, Bejan [2].

$$\dot{S}' = \frac{\dot{m}}{\rho T} \left(-\frac{\Delta p}{L} \right) + \frac{q'_c \Delta T}{T^2} \quad (4.1)$$

where T , $\Delta p/L$, ΔT and q'_c are the absolute bulk temperature of the stream (\dot{m}), average frictional pressure gradient per unit heated length, wall-bulk-fluid temperature difference averaged over heated length, L ($= \frac{1}{L} \int_0^L [T_w(x) - T_b(x)] dx$) and the heat transfer rate per unit heated length respectively. Equation 4.1 can now be related to average heat transfer information ($\overline{Nu} = (q'_c D_h)/(w \Delta T k)$), where D_h and w is the hydraulic diameter and width of the duct respectively. Substituting the relations for ΔT into Equation 4.1 using \overline{Nu} and q'_c gives:

$$\dot{S}' = \frac{\dot{m}}{\rho T} \left(-\frac{\Delta p}{L} \right) + \frac{(q'_c)^2 D_h}{w k T^2 \overline{Nu}} \quad (4.2)$$

First term on the right side of Equation 4.2 represents the fluid-flow irreversibility and the second term is the heat transfer irreversibility. The relative importance of the two irreversibility mechanism is described by the irreversibility distribution ratio ϕ , which is defined by (Bejan [1982]):

$$\phi = \frac{\text{fluid flow irreversibility}}{\text{heat transfer irreversibility}} = \frac{\frac{\dot{m}}{\rho T} \left(-\frac{\Delta p}{L} \right)}{[(q'_c)^2 D_h]/[w k T^2 \overline{Nu}]} \quad (4.3)$$

In general, however, $N_{S,a}$ is a function of the ratio of heat transfer coefficients (St_a/St_o) and the friction factor ratio (f_a/f_o). The relative importance of the friction factor ratio is dictated by the numerical value of ϕ_o , which describes the thermodynamic mode in which the passage is meant to function. Bejan and Pfister [1980] observed that a critical value of ϕ_o exists which is typically less than unity which helps in deciding whether the use of augmentation technique will yield saving in available work. If in any device the irreversibility distribution ratio exceeds the critical ϕ_o , the augmentation scheme will not reduce the rate of entropy generation, even though the heat transfer is enhanced. Here, irreversibility distribution ratio, ϕ_o for the smooth duct for Reynolds number 12800, 20900 and 29400 are 0.001037, 0.004057 and 0.009122, respectively. Therefore the heat transfer irreversibility totally dominates. Table 4.6 shows that, the $N_{\overline{Nu}f,a}$ first increases and then decreases as the Reynolds number increases for both the configuration (one & two-rib case). However, the $N_{\overline{Nu}f,a}$ value for one-rib case indicate that it is the fluid flow irreversibility that poses the larger threat. It is also seen that for both the configuration, the presence of rib have less effect on the entropy generation due to heat transfer, $\dot{S}'_{\Delta T}$. It is the effect of $\dot{S}'_{\Delta P}$, which plays the significant role in the increase of irreversibility distribution ratio, ϕ_o for both the cases with respect to Re.

Table 4.6: Performance evaluation parameters

Configuration	Re	$N_{\overline{Nuf},a}$	$N_{\overline{Nu},a}$	$N_{S,a}$	ϕ
One-rib	12800	1.08	1.39	1.16	0.001309
	20900	1.28	1.66	0.97	0.006473
	29400	1.21	1.61	0.97	0.015126
Two-rib	12800	0.90	1.52	1.02	0.002231
	20900	0.95	1.87	0.90	0.011589
	29400	0.76	1.87	0.84	0.035359

To ensure that $N_{S,a}$ only reflected the changes due to the augmentation schemes, the experiments were all performed for the same laboratory conditions, the same mass flow rates (maximum deviation 4.0 %), and the same input power to keep q'_c fixed within 1.3%. Average results for the heated length were determined from integrating the different local results over the entire heated length for each case.

Further, Table 4.6 shows that, the value of $N_{\overline{Nu},a}$ is more for two-rib case than that of the one-rib case for all Reynolds number. Though, there exist a monotonic increase in heat transfer coefficient for both the configuration (one & two-rib case) in compare to the baseline case (un-augmented passage) with respect to the speeds, but the value of $N_{S,a}$ is found to be more than unity at low speed. This indicates that at low Reynolds number the augmentation schemes are not thermodynamically advantageous. The augmentation schemes (one & two-rib case) give the values of $N_{S,a}$ less than unity as the Reynolds number increases, which signifies the thermodynamic advantage i.e. in addition to heat transfer they reduces the irreversibility of the apparatus. Also, there exists a critical Reynolds number at which the value of $N_{S,a}$ may found to be unity, and below that critical Re the the augmentation scheme fails to give the thermodynamically efficient results even though the heat transfer is enhanced ($N_{\overline{Nu},a} > 1$).

Chapter 5

Conclusions and Scope for Future Work

5.1 Conclusions

This study has focussed on the degree of heat transfer enhancement obtained in gas turbine blade cooling passages and heat exchangers, by adopting the ribbed duct technology. The engineering aspect of heat transfer enhancement is corroborated with extensive fluid flow measurements. The investigation has been carried out experimentally in a rectangular channel with one-rib and two-ribs mounted on the bottom surface at three different Reynolds numbers and for different heating levels. Liquid crystal thermography (LCT) has been used for surface temperature visualization and Nusselt number calculation. Mean and fluctuating velocity and temperature results obtained respectively from hot wire anemometry (HWA) and resistance thermometry (RTD) are presented and correlated with heat transfer enhancement. The following observations are made from the present work:

1. The liquid crystal thermography (LCT) is a promising technique not only from visualization point of view but also as a quantitative evaluation tool. The transient liquid crystal thermography has been implemented successfully for accurate determination of surface Nusselt number as confirmed by the energy balance check.
2. The transient liquid crystal thermography visualization and surface Nusselt

number distribution show the flow behind the rib to be three dimensional in nature. The ineffectiveness of the re-circulation region and the effectiveness of the re-attachment region for heat transfer enhancement is clearly visible for one-rib and two-rib cases. The stagnant flow region near the second rib is observed to be almost absent or very less significant than that near the first rib for the two rib case.

3. The velocity and temperature profiles for the smooth channel follows the law of the wall indicating the flow to be turbulent in nature. The skin friction coefficient, boundary layer thickness and Nusselt number plots also supports the above observation.
4. The shape factor of the velocity boundary layer decreases continuously in the stream-wise direction and approaching to steady values and this steady value is observed to be different for the smooth surface, one-rib surface and two-rib surfaces. The u^+ vs y^+ plots support the shape factor results. It is observed that the transition of the rib roughened boundary layer to the equilibrium flat plate boundary layer takes place more rapidly for thermal boundary layer than the velocity boundary layer. This finding is supported by the fact that thermal boundary layer development is faster for the $Pr < 1$ case in comparison to the velocity boundary layer.
5. The maximum value of u_{rms} is observed to increase in the streamwise direction and then decreases subsequently for the one-rib case. For the two-rib case, the u_{rms} is observed to increase a second time after the second rib. But, the increase in magnitude after the second rib is less significant in comparison to that after the first rib. The rms value of temperature is observed to be correlated to the u_{rms} values.
6. Nusselt number and skin friction coefficient for the ribbed surface are higher than that of smooth surface.
7. Performance evaluation has been carried out using entropy generation principle. It is observed that at low Reynolds number, the augmentation is not thermodynamically advantageous even though Nusselt number increases due to the presence of ribs. There exists a critical Reynolds number above which the augmentation is thermodynamically efficient.

8. The Nusselt number calculation from the curve fitting of the temperature profile is observed not to be robust in nature. This observation questions the validity of this approach used by some earlier investigations. In general, it is observed that low-order polynomial works efficiently for the smooth channel case and higher order polynomials are efficient for ribbed surface cases.

Bibliography

- [1] Acharya, S., Dutta, S., Myrum, T.A. and Baker, R.S., Periodically developed flow and heat transfer in a ribbed duct, *Int.J.Heat Mass Transfer*, Vol. 36, pp 2069-2082 (1993).
- [2] Bejan, A.E., *Entropy Generation Through Heat and Fluid Flow*, Wiley, NY, (1982)
- [3] Burggraf, F., Experimental heat transfer and pressure drop with two dimensional turbulence promoters applied to two opposite wall of a square tube, Augmentation of convective heat and mass transfer, A.E Berbles and R.L webb, eds, ASME, pp 70-79 (1970).
- [4] Camci, C., Kim, K. and Hippensteele, S.A., A new hue capturing technique for the quatitative interpretation of liquid crystal images used in convective heat transfer studies, *ASME J Turbomachinery*, Vol. 114, pp 765-775 (1992).
- [5] Chan, T.L., Ashforth-Frost, S. and Jambunathan, K., Calibrating for viewing angle effect during heat transfer measurements on a curved surface, *Int. J. Heat Mass Transfer*, Vol. 44, pp 2209-2223 (2001)
- [6] Chandra, P.R., Han, J.C. and Lau, S.C., Effect of rib angle on local heat/mass transfer in a two-pass rib-roughened channel, *ASME J. Turbo-machinery*, Vol. 119, pp 233-241 (1988).
- [7] de Boer, J. B. and Fische, D., "Interior Lighting", Philips Technical Library, Kluwer Technical Books, Newyork, pp. 147 (1981).
- [8] Ekkad, S.V. and Han, J.C., Detailed heat transfer distribution in two-pass square channels with rib turbulators, *Int.J.Heat Mass Transfer*, Vol. 40, pp 2525-2537 (1997).

- [9] Farina, D. J., Ahcker, J.M., Moffat, J. and Eaton, J. K., Illuminant invariant calibration of thermochromic liquid crystals, *Exp. Therm. Fluid Sci.* 9, pp 1-12 (1994).
- [10] Han, J.C., Heat transfer and friction in channels with two opposite rib-roughened walls, *ASME J Heat Transfer*, Vol. 106, pp 774-781 (1984).
- [11] Han, J.C., Park, J.S. and Lei, C.K., Heat Transfer enhancement in channels with turbulence promoters, *ASME J Engineering for Turbines and Power*, Vol. 107, pp 628-635 (1985).
- [12] Han, J.C., Heat transfer and friction characteristics in rectangular channels with rib turbulators, *Int.J.Heat Mass Transfer*, Vol. 110, pp 321-328 (1988).
- [13] Han, J.C., Zhang, Y.M. and Lee, C.P., Augmented heat transfer in square channels with parallel, crossed, and V-shaped angled ribs, *Int.J.Heat Mass Transfer*, Vol. 113, pp 590-596 (1991).
- [14] Hirota, M., Fujita, H. and Yokosawa, H., Experimental study on convective heat transfer for turbulent flow in a square duct ribbed rough wall (Characteristics of mean temperature field)., *J. of Heat Transfer*, Vol. 116, pp 332-340 (1994).
- [15] Holman, J.P., *Heat Transfer*, McGraw-Hill, New York, 1997.
- [16] Hwang, J.J. and Liou, T.M., Augmentation heat transfer in a rectangular with permeable ribs mounted on the wall, *Int.J.Heat Transfer*, Vol. 116, pp 912-920 (1994).
- [17] Hwang, J.J. and Liou, T.M., Heat transfer augmentation in a rectangular with slit rib turbulators on two opposite walls. *ASME J. Turbomachinery*, Vol. 119, pp 617-623 (1997).
- [18] Hwang, J.J., Heat transfer and friction characteristics comparison in rectangular ducts with slit rib turbulators on one wall, *Int.J.Heat Transfer*, Vol. 120, pp 709-716 (1998).
- [19] Incropera, F.P. and Dewitt, D.P., *Fundamentals of heat and mass transfer*, John Willey and Sons, (1998).

- [20] Ireland, P.T. and Jones T.V., Response time of a surface thermometer employing encapsulated thermochromic liquid crystals, *J. Phys.*, Vol. 20, pp 1195-1199 (1987).
- [21] Ireland, P.T. and Jones T.V., Liquid crystal measurements of heat transfer and surface shear stress, *Meas. Sci. Technol.*, Vol. 11, pp 969-986 (2000).
- [22] Kays, W.M. and Crawford, M.E., *Convective Heat and Mass Transfer*, McGraw-Hill, New York, 1993.
- [23] Kukreja, R.T. and Lau, S.C., Distributions of local heat transfer coefficient on surfaces with solid and perforated ribs, *J. Enhanced Heat Transfer*, Vol. 5/1, pp 9-21 (1998).
- [24] Liou, T.M. and Hwang, J.J., Developing heat transfer and friction in a ribbed rectangular duct with flow separation at inlet, *ASME J. Heat Transfer*, Vol. 114, 565-573 (1992b).
- [25] Metzger, D.E., Chyu, M.K. and Bunker, R.S., The contribution of on-rib heat transfer coefficients to total heat transfer from rib-roughened surfaces, *Transport Phenomena in Rotating Machinery*, J.H. Kim, ed., Hemisphere Publishing Co, 1988.
- [26] Mochizuki, S., Murata, A., Shibata, R., and Yang, W.,J., Detailed measurement of local heat transfer coefficients in turbulent flow through smooth and rib-roughened serpentine passages with a 180° sharp end, *Int.J.Heat Mass Transfer*, Vol. 42, pp 1925-1934 (1999).
- [27] Schlichting, H., *Boundary Layer Theory*, 7th ed., McGraw-Hill Book company, New York, 1979.
- [28] Taslim, M.E., Li, T. and Kercher, D.M., Experimental heat transfer and friction in channels roughened with angled, V-shaped and discrete ribs on two opposite walls, *ASME J Turbomachinery*, Vol. 118, pp 20-28 (1996).
- [29] Taslim, M.E., Li, T. and Spring, S.D., Measurement of heat transfer coefficients and friction factors in passages rib-roughened on all walls, *ASME J Turbomachinery*, Vol. 120, 564-570(1999).

-
- [30] Tsia, J.P. and Hwang, J.J., Measurements of heat transfer and fluid flow in a rectangular duct with alternate attached-detached rib arrays, *Int. J. Heat Mass Transfer*, Vol. 42, 2072-2083 (1999).